Title
Femtosecond Molecular Dynamics Studied with Vacuum Ultraviolet Pulse Pairs

Author
Allison III, Thomas K.

Publication Date
2010

Peer reviewed|Thesis/dissertation

Femtosecond Molecular Dynamics Studied With Vacuum Ultraviolet Pulse Pairs

by

Thomas K. Allison III

A dissertation submitted in partial satisfaction of the

requirements for the degree of

Doctor of Philosophy

in

Physics

in the

Graduate Division

of the

University of California, Berkeley

Committee in charge:

Professor R. W. Falcone, Chair

Professor Y. R. Shen

Professor D. M. Neumark

Spring 2010

Femtosecond Molecular Dynamics Studied With Vacuum Ultraviolet Pulse Pairs

Abstract

Femtosecond Molecular Dynamics Studied With Vacuum Ultraviolet Pulse Pairs

by

Thomas K. Allison III

Doctor of Philosophy in Physics

University of California, Berkeley

Professor R. W. Falcone, Chair

Atoms and molecules have most of their oscillator strength in the vacuum ultraviolet (VUV) and extreme ultraviolet (XUV), between the wavelengths of 200 nm and 30 nm. However, most femtosecond spectroscopy has been restricted to the visible and infrared due to a lack of sufficiently intense VUV and XUV femtosecond light sources. This thesis discusses extensions of pump/probe spectroscopy to the VUV and XUV, and its application to the dynamics of ethylene and oxygen molecules excited at 161 nm.

I begin with a detailed discussion of the short wavelength light source used in this work. The source is based on the high order harmonics of a near infrared laser and can deliver $> 10^{10}$ photons per shot in femtosecond pulses, corresponding to nearly 10 MW peak power in the XUV. Measurements of the harmonic yields as a function of the generation conditions reveal the roles of phase matching and ionization gating in the high order harmonic generation process.

Pump/probe measurements are conducted using a unique VUV interferometer, capable of combining two different harmonics at a focus with variable delay. Measurements of VUV multiphoton ionization allows for characterization of the source and the interferometer. In molecules, time resolved measurements of fragment ion yields reveal the femtosecond dynamics of the system. The range of wavelengths available for pump and probe allows the dynamics to be followed from photo-excitation all the way to dissociation without detection window effects.

The dynamics in ethylene upon $\pi \rightarrow \pi^*$ excitation are protypical of larger molecules and have thus served as an important test case for advanced ab initio molecular dynamics theories. Femtosecond measurements to date, however, have been extremely lacking. In the present work, through a series of pump probe experiments using VUV and XUV pulses, time scales for the non-adiabatic relaxation of the electronic excitation, hydrogen migration across the double bond, and H_2 molecule elimination are measured and compared to theory.

In the simpler oxygen molecule, excitation in the Schuman-Runge continuum leads to direct dissociation along the B $^3\Sigma_u^-$ potential energy curve. The time resolved photoion spectra show that the total photoionization cross section of the molecule resembles two oxygen atoms within 50 fs after excitation.

To Cassandra

Contents

List of Figures

List of Tables

Acknowledgments

I have had the benefit of working with many scientists during my time in Berkeley. I need to thank Aaron Lindenberg, Donnacha Lowney, and Marcus Hertlein for teaching me most of what I know about lasers. In the beginning, Marc Hertlien, Magnus Bergh, Carl Calleman, and I started setting things up in two empty labs in the fourth floor of Building 2. Magnus and Calle went back to Sweden and Marc moved into his new job at the ALS. Jeroen van Tilborg joined the project, and for about a year it was just the two of us optimizing the harmonic yield and setting up the experimental endstation (Magnus Chamber). We were joined by Travis Wright in the summer of 2007 and started conducting the first experiments on multiphoton ionization, at least when the vacuum pumps were all working. Hamed Merdji came occasionally from France, always with some good ideas on how to get more XUV flux. Drew Kemp and Seno Rekawa helped with the design of the split mirror interferrometer. Yanwei Liu, Andy Aquila, and Sasa Bajt fabricated multilayer mirrors for us. Timur Osipov worked with Travis to develop the data acquisition software for the split mirror. Dan Haxton provided advice and encouragement on my Schrödinger equation solver. In the last year, Travis went to Davis and Jeroen went back to the world of petawatt lasers. Siin Che, Adam Stooke, and Champak Khurmi joined the project during the "surge" and they continue it now with Travis.

Through it all were my advisors Roger Falcone and Ali Belkacem. Early on, Roger patiently taught me the physics of lasers and x-rays, and Ali ultimately steered the project in a productive direction. This project would not have been a success without their unwavering support through good times and bad. I also wish to thank Ernie Glover, Phil Heimann, and Bob Schoenlein for technical advice, encouragement, and inspiration.

Chapter 1

Introduction

There are known knowns. These are things we know that we know. There are known unknowns. That is to say, there are things that we now know we don't know. But there are also unknown unknowns. These are things we do not know we don't know.

-Secretary of Defense Donald Rumsfeld

Much of the technology developed in the 20th century derives from our ever increasing ability to control electromagnetic fields. From the early days of telephone and radio communication to the current era of the internet and GHz microprocessors, physicists and engineers have worked to produce and utilize electromagnetic fields of higher frequency and larger coherent bandwidths. The field of ultrafast science, which began at the end of the 20th century, is thus appropriately positioned historically. Although there is still much work to do, in the beginning of the 21st century, it appears that mankind's mastery over the electromagnetic spectrum is on a path to completion. Using femtosecond lasers, it is now routine to produce controlled electromagnetic waveforms in the visible and infrared with coherent bandwidths spanning tens to hundreds of THz. High order harmonics of these lasers can be generated, providing coherent light in the vacuum ultraviolet and soft x-ray region [1]. Free electron lasers are now producing the first coherent hard x-ray light [2], and the next generation of seeded x-ray lasers will allow chains of coherent light sources from the THz to the hard x-ray [3, 4].

Biological systems, on the other hand, have developed their technology with a different fundamental architecture. The machinery of living organisms is chemical in nature. Neurons transmit signals through electrochemical reactions, and information in DNA is stored not as oriented magnetic domains on a hard-drive platter, but as complex arrangements of molecules. Relative to electromagnetic devices, our understanding of this technology is extremely primitive. Nonetheless, optimistic scientists have said that the 21st century will be the century of biology [5]: That as we learn how to engineer macro-molecular systems, amazing new man-made technologies will emerge from a bio-chemical architecture.

An important class of complex molecular systems that many researchers hope to

some day utilize for next generation technology [6] are those that absorb light and convert it into chemical energy. When light interacts with a molecule, the interaction is mediated through the electromagnetic force between the light field and the electrons. Quantum mechanically, the electrons are promoted to excited orbitals via the absorption of photons. The excited electrons now provide different forces for the nuclei, and the nuclei move in response. The excitation energy is thus transfered from the electrons to the nucleii. Many studies have now established [7, 8] that this transfer of energy from electrons to nucleii can proceed extremely rapidly, on the time scale of a few molecular vibrations or less. For example, in the first event in animal vision, upon absorbing a photon the rhodopsin molecule isomerizes [7] to a twisted configuration within 200 femtoseconds (fs = 10^{-15} s), initiating a string of chemical reactions which ultimately results in the firing of neurons. The speed of the initial step is critical to the ultimate success of the process, because of the large number of degrees of freedom of the molecule and its environment. If the nuclear motion is not funneled down a directed pathway on a time scale much shorter than thermalization, the absorption of the photon will not produce a signal in the brain, but be lost as random vibrations of rhodopsin and its environment, or heat.

Experimentally, dynamics taking place on these fast time scales are studied using laser pulses of femtosecond duration. A typical experimental technique uses pairs of pulses to carry out a "pump-probe" measurement. The first pulse, called the pump, excites a molecule and initiates the dynamics, and a second pulse comes a variable delay time τ later and probes the system as it evolves. This arrangement is illustrated in figure 1.1. There are many schemes by which the probe signal can be recorded. For molecules in solution, the absorption of the probe light by the sample can be monitored, giving information about the status of the absorbing electrons. The dynamics can also be probed by the nonlinear interaction of multiple probe pulses. For studies on isolated molecules in vacuum, ions or electrons created by the probe pulse(s) can be detected. The number of possible schemes is truly endless, but at the heart of all of them is the femtosecond laser pulse. The time resolution of any such experiment is ultimately limited by the pulse duration of the pulses employed, or alternatively, the bandwidth of coherent electromagnetic radiation that can be formed into a controlled pulse.

Fundamentally, atoms and molecules have the bulk of their oscillator strength in the vacuum ultraviolet (VUV) and extreme ultraviolet (XUV) [9, 10], between the wavelengths of 200 and 30 nm. XUV photons are also sufficiently energetic to ionize a molecule, and much information can be gleaned from the collection of the charged particles that result. Indeed, much of what we know about molecular physics is from studies using VUV and XUV light [11, 10]. In this thesis, I will describe an apparatus which I developed to perform VUV/XUV pump-probe spectroscopy. High order harmonics of an infrared laser provide femtosecond pulses of VUV and XUV light, which are applied to the study the dynamics of ethylene (C_2H_4) and oxygen (O_2) molecules excited in their first absorption band at 161 nm. This thesis, and others like it, describes techniques that extend our ability to control and utilize electromagnetic waves a little bit further, in the hope of understanding some of nature's ultrafast molecular tricks.

My goal has been to produce a manuscript readable by the general physicist, but useful to the specialist. The thesis is organized as follows. The rest of this chapter

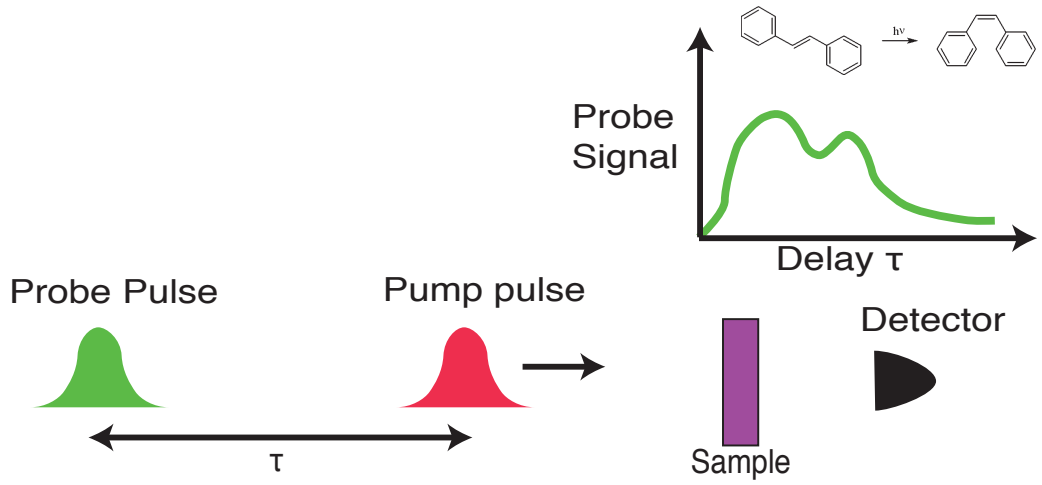

Figure 1.1: **A Generic Pump Probe Experiment.** The probe signal is recorded as a function of the delay between the two pulses, from which one hopes to reconstruct the dynamics of the sample initiated by the pump pulse.

is devoted to introducing basic concepts in molecular physics, photo-ionizaton, and high order harmonic generation (HHG) relevant to the later chapters. Experts in these fields are probably already very familiar with this material. Chapter 2 discusses the power scaling of high order harmonic generation, and the HHG source used in this work to get VUV/XUV intensities sufficient for pump/probe studies. Chapter 3 is devoted to details of the split mirror interferometer used to recombine high order harmonics at a focus with variable delay. Chapter 4 is devoted to VUV/XUV pump probe experiments performed on the ethylene molecule. Chapter 5 contains similar measurements performed on molecular oxygen. In chapter 6, I conclude with some perspectives on the work in this thesis and an outlook on the future role for VUV/XUV pump probe spectroscopy in atomic and molecular physics.

1.1 Molecular Physics

A molecule is a collection of nuclei with positions $\mathbf{R}_i$ and electrons with positions $\mathbf{r}_j$, with total wavefunction Ψ that obeys the Schrödinger equation:

$$H\Psi(\mathbf{r}_1, \mathbf{r}_2, \ldots, \mathbf{R}_1, \mathbf{R}_2, \ldots) = E\Psi(\mathbf{r}_1, \mathbf{r}_2, \ldots \mathbf{R}_1, \mathbf{R}_2, \ldots) \tag{1.1}$$

The full molecular Hamiltonian H contains terms for the kinetic energy of the electrons T_e, the Coulomb interactions between the electrons V_e, the kinetic energy of the nuclei T_N, the Coulomb interactions between the nuclei V_N, and the Coulomb interactions between the electrons and the nuclei V_{eN}.

$$H = \sum_i -\frac{\hbar^2\nabla^2_{e,i}}{2m} + \sum_{j>i}\frac{e^2}{|\mathbf{r}_i - \mathbf{r}_j|} + \sum_i -\frac{\hbar^2\nabla^2_{N,i}}{2M_i} + \sum_{j>i}\frac{Z_i Z_j e^2}{|\mathbf{R}_i - \mathbf{R}_j|} + \sum_{ij} -\frac{Z_j e^2}{|\mathbf{r}_i - \mathbf{R}_j|}$$

$$= \quad T_e + V_e + T_N + V_N + V_{eN} \tag{1.2}$$

The laplacians $\nabla^2_{e,i}$ and $\nabla^2_{N,i}$ refer to differentiation with respect to the coordinates of the ith electron or ion, respectively. Z_i is the charge of the ith nucleus and M_i is its mass. The symbols m and e stand for the charge and mass of the electron, and $\hbar$ is Planck's constant. No one knows how to solve the Schrödinger equation, not even for the simplest molecules. Brute force numerical solution runs into the so-called "exponential wall" [12]. The computer power needed to solve the Schrödinger equation for N particles scales as e^N, a severe limitation for all but the smallest molecules. To make any progress at all requires approximations. The first and most important approximation is the *Born-Oppenheimer* approximation, also called the *adiabatic* approximation. For simplicity, from now on I will denote all of the electronic coordinates by the symbol r and all of the nuclear coordinates by the symbol R. If the nuclei were all frozen in place at position R, the electronic eigenfunctions $\psi_n(r;R)$ on the fixed nuclear frame would be solutions of the equation:

$$(T_e + V_e + V_{eN})\psi_n(r;R) = E_n(R)\psi_n(r;R) \tag{1.3}$$

At each position of the nuclei R, the electronic wave functions ψ_n form an orthogonal complete set, and we can expand the wavefunction as a superposition of the ψ_n with coefficients $\chi_n(R)$.

$$\Psi(r,R) = \sum_n \chi_n(R)\psi_n(r;R) \tag{1.4}$$

Insertion of equation (1.4) into the Schrödinger equation (1.1) and projecting from the left with $\psi_m(r,R)$ leads to the following coupled set of equations for the coefficients $\chi_m(R)$:

$$\left(T_N + E_m(R) + V_N(R)\right)\chi_m(R) + \sum_n 2\left[\vec{T}^{(1)}_{mn}.\nabla + \vec{T}^{(2)}_{mn}.\nabla\right]\chi_n(R) = E\chi_m(R) \tag{1.5}$$

where

$$\vec{T}^{(1)}_{mn} = \langle\psi_m|\nabla\psi_m\rangle \tag{1.6}$$

$$\vec{T}^{(2)}_{mn} = \langle\psi_m|\nabla^2\psi_m\rangle \tag{1.7}$$

The notation has been compacted by having the operator ∇ represent a multi-dimensional derivative with respect to mass weighted nuclear coordinates [13]. The terms $\vec{T}^{(1)}_{mn}$ and $\vec{T}^{(2)}_{mn}$ are responsible for the off-diagonal terms in equation (1.4) and are called the non-adiabatic couplings. The Born-Oppenheimer approximation consists of neglecting these terms so that equation (1.5) reads:

$$\left[T_N + V_m(R)\right]\chi_m(R) = E\chi_m(R) \tag{1.8}$$

with $V_m(R) = E_m(R) + V_N(R)$. From equation (1.8), we can now see that in the Born-Oppenheimer $\chi_m(R)$ satisfies a time independent Schrödinger equation for the nuclei as if they were moving on a potential given by $V_m(R)$, a combination of the electronic energy $E_m(R)$ and the nuclear Coulomb repulsion $V_N(R)$. The function $\chi_m(R)$ is called the nuclear wave function and the time dependent version of (1.8) governs the nuclear dynamics. The electrons provide a potential energy surface (PES) $V_m(R)$ on which the nuclei move. If the molecule is in only one electronic state with wavefunction $\psi_m(r;R)$, so that all the χ_n of

equation (1.4) are zero except for $n = m$, within the Born-Oppenheimer approximation it will remain in only this electronic state, and the the nuclei will move on one PES. The wavefunction is then:

$$\Psi(r, R) = \chi(R)\psi(r; R) \tag{1.9}$$

The Born-Oppenheimer approximation has seperated the motions of the electrons and the nuclei. The electronic wavefunction and the nuclear wavefunction each have their own Schrödinger equation, and interact only through the parameters R and $E(R)$. The separation is justified on the basis that the electrons in general move much faster than the nuclei. This can be deduced from the following simple argument. The electrons and nuclei are subject to electrostatic forces of comparable magnitude, but have very different masses. If we consider simple harmonic motions about an equilibrium situation, both will have roughly the same force constant k. The electrons will move with charecteristic frequency $\omega_e \sim \sqrt{k/m}$ whereas the nuclei will have $\omega_N \sim \sqrt{k/M}$. The ratio is then $\omega_e/\omega_N \sim \sqrt{M/m}$, which is typically on the order of a 100 or larger. The changes to the electronic wavefunction as the nuclei move can thus be treated *adiabatically* [14], with the electronic wavefunction smoothly deforming as the geometry of the molecule changes.

The validity of the Born-Oppenheimer approximation is exemplified in the typical energy level structure of a molecule, shown in figure 1.2. The spacing in energy between different electronic states ΔE is usually several electron volts, whereas a quantum of nuclear vibration $\hbar\omega_0$ is 1/10 of an eV or less. A nuclear wavepacket, consisting of several vibrational states, will evolve on a time scale $\sim \hbar/(\hbar\omega_0)$. A superposition of electronic states will evolve on the much faster time scale $\hbar/\Delta E$.

Now, with the electronic and nuclear motions separated, one can begin to make progress, both computationally and conceptually. Computationally, the electronic problem given by (1.3) does not need to be solved exactly. What is needed is a reasonable approximation of the PES defined by $V_m(R)$, which can perhaps be obtained by Hartree-Fock methods and their expansions [15] or density functional theory [12]. Given the PES, one can then model the nuclear dynamics either by approximate solutions to the nuclear Schrödinger equation or with semi-classical methods. Conceptually, absorption of a photon promotes the electrons to an excited state. The nuclear wavefunction is projected on the manifold of vibrational states of the excited PES, and forms a wavepacket which moves on the excited PES. This is illustrated in figure 1.2 with our generic pump and probe scheme.

However, nothing in our preceding analysis ruled out the possibility of the electronic energy levels becoming degenerate so that $\Delta E = 0$ for some configuration of the molecule R_d. For a diatomic molecule with only one internal degree of freedom ($N = 1$), it turns out that two potential energy curves corresponding to electronic states of the same symmetry are in general not degenerate for any value of R [13]. This is the so-called "non-crossing rule" and places where two curves come close are called *avoided crossings*. For systems with $N = 2$ coordinates, there is generally a discreet set of isolate points where two PES's can touch. These points are called "conical intersections", because of the geometrical structure of the PES's near the point [17]. In $N > 2$ dimensions, the intersection is a manifold in $N - 2$ dimensions. Conical intersections and avoided crossings can have profound effects on the dynamics. At these points, and the vicinity around them, the electronic and nuclear wavefunctions evolve on comparable timescales, and the Born-Oppenheimer approx-

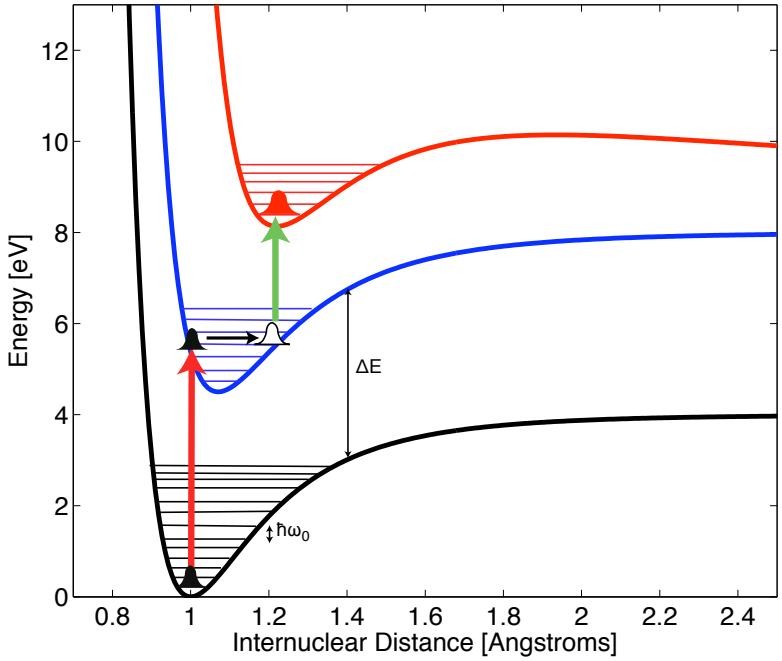

Figure 1.2: **Molecular Potential Energy Surfaces** A typical manifold of potential energy surfaces. Horizontal lines indicate energy levels of vibrational eigenstates of the nuclear wavefunction. Note that the spacing between vibrational energy levels $\hbar\omega_0$ is much smaller than the spacing between electronic energy levels ΔE. A pump photon (red) can excite the molecule and launch a wavepacket to an excited potential energy curve, from where it's evolution can be probed by a photon from the probe pulse (green).

imation breaks down. Mathematically, the non-adiabatic coupling vectors involve derivatives of the electronic wavefunctions with respect to the nuclear coordinates. Near points of degeneracy the nuclear motion can induce large changes in the electronic wavefunction and the non-adiabatic coupling vectors are no longer small. The Schrödinger equation (1.5) is then no longer diagonal, and *non-adiabatic* transitions between different electronic states can occur. A conical intersection between two electronic PES's of the ethylene molecule is shown in figure 1.3.

By allowing transitions between electronic PES's, conical intersections facilitate the internal conversion of electronic excitation into nuclear motion, and play a crucial role in photochemistry [17]. For example, excitation of a DNA base with ultraviolet light has the potential to cause damage to the DNA chain, because while the molecule resides in an excited electronic state, it is much more reactive. But most of the time we have one or our DNA bases excited with a photon, our DNA does not break. Instead the electronic excitation decays quickly through a conical intersection and the energy is safely dispersed to gentle vibrations before any damage is done [18].

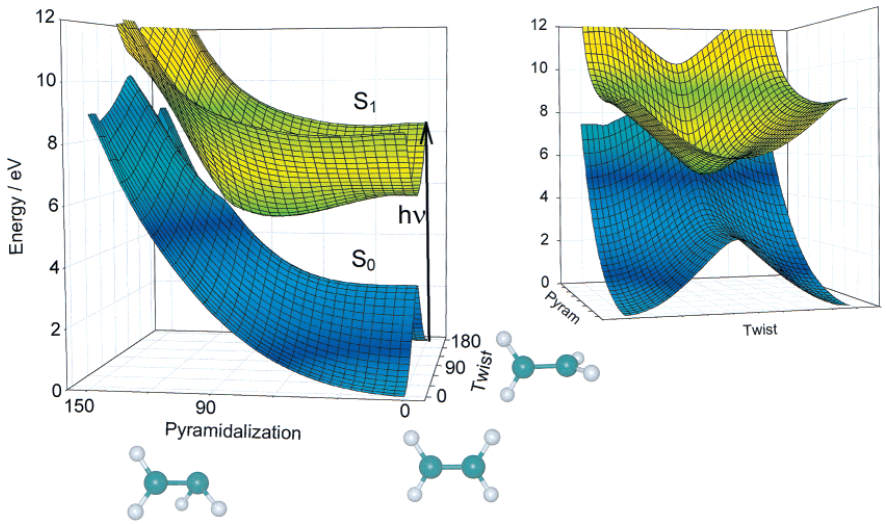

Figure 1.3: **A Conical Intersection.** Theoretical Potential Energy Surfaces of the ethylene molecule (C_2H_4) from [16]. Photon excitation starts a wavepacket on the S_1 surface from the planar equilibrium geometry of the ground state. The nuclear wavefunction quickly finds the conical intersection, transitioning to the S_0 surface.

1.2 Photoexcitation and Photoionization

When a molecule interacts with light, the amplitude of making a transition from an initial state i to a final state f is given by the dipole matrix element [10]

$$\langle \Psi_f | \sum_j \mathbf{r}_j | \Psi_i \rangle \tag{1.10}$$

where the sum runs over all the electrons of the molecule. If we consider two Born-Oppenheimer states in the form of equation (1.9), the matrix element takes the form

$$\langle \Psi_f | \sum_n \mathbf{r}_j | \Psi_i \rangle = \langle \chi_f(R) | \left(\langle \psi_f(r;R) | \sum_j \mathbf{r}_j | \psi_i(r;R) \rangle \right) | \chi_i(R) \rangle \tag{1.11}$$

The term inside the parentheses is the dipole matrix element between the two electronic states

$$d_{fi}(R) = \langle \psi_f(r;R) | \sum_j \mathbf{r}_j | \psi_i(r;R) \rangle \tag{1.12}$$

In the *Franck-Condon* approximation, the variation of $d_{fi}(R)$ with respect to R is neglected for the purposes of the R integral, and the transition amplitude becomes

$$\langle \Psi_f | \sum_j \mathbf{r}_j | \Psi_i \rangle = \langle \chi_f | \chi_i \rangle \, d_{fi}(\bar{R}) \tag{1.13}$$

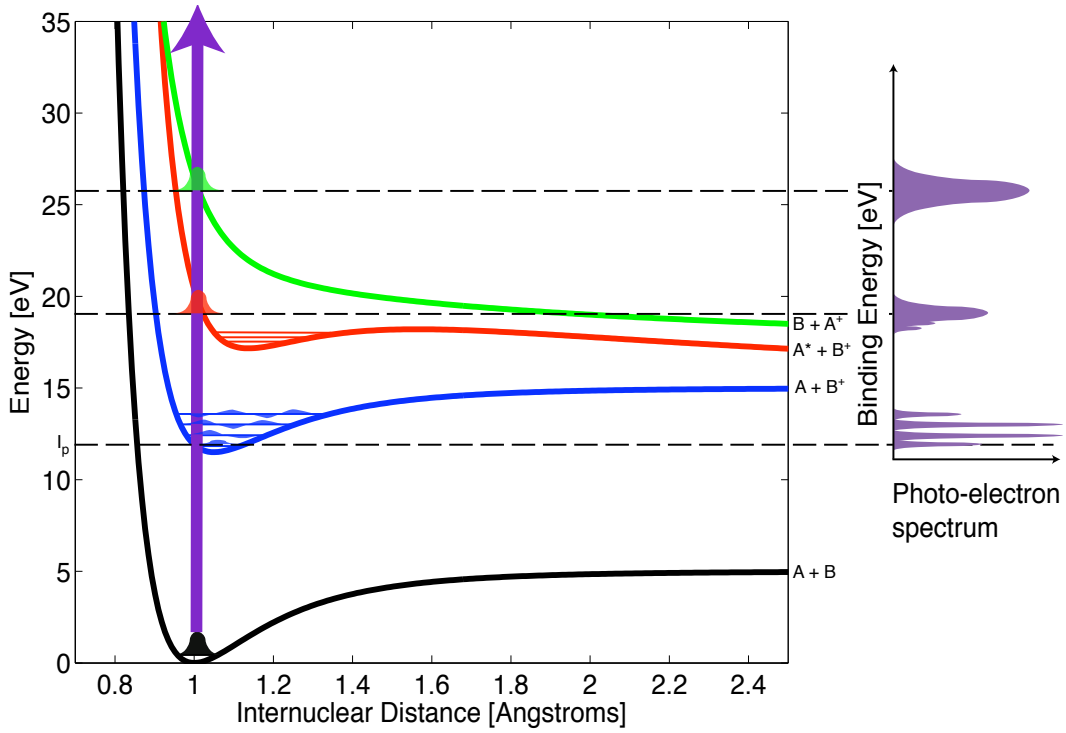

Figure 1.4: **Molecular Photoionization.** An XUV photon can leave the molecular cation in many states upon ionization, some of which will dissociate to fragment ions and neutrals. The photoelectron spectrum shows the branching ratio for leaving the photo-ion in a particular state. The binding energy is $h\nu - E_e$.

where $\bar{R}$ is the centroid of the initial nuclear wavefunction. The amplitude for populating a final nuclear wavefunction $\chi_f(R)$ is then given by the simple projection $\langle \chi_f | \chi_i \rangle$, called the Franck-Condon factor. Classically, the Franck-Condon principle amounts to treating photoexcitation as an instantaneous process with respect to nuclear motion, so that on an energy level diagram such as figure 1.2, transitions occur vertically. For example, a transition directly from the initial state at $R = 1.0$ Å to the final state at $R = 1.2$ Å in figure 1.2 is not allowed, as this would require nuclear motion during the photoexcitation.

The dynamics of large molecules in aqueous solution, such as the Rhodopsin or Adenine molecules metioned above, are extremely complicated to study, both experimentally and theoretically. Theoretically, the size of the molecule and the interaction with the solvent make calculating realistic PES's difficult. Experimentally, a change in probe absorption is often impossible to assign unambiguously, particularly in the visible and infrared regimes. To avoid these complexities and facilitate comparison to theory, one would like to study small molecules, isolated in vacuum. However, the absorption of a dilute beam of molecules is weak compared to a solid or liquid sample, and the fractional change in the transmitted probe pulse power is small. Instead, the absorption of the probe can be registered through photo-ionization by detecting the charged particles that result.

The ionization potential I_p is the energy required to remove an electron from a molecule. When a photon with $h\nu > I_p$ is absorbed by a molecule, a free electron (photo-electron) and a molecular ion (photo-ion) can be created. The math describing the photon absorption is the same, except that now the final electronic state ψ_f is that of a molecular ion and a free electron with energy E_e. Because E_e is a continuous variable, many possible final electronic states of the ion can be populated by photoionization. Figure 1.4 illustrates several photoionization processes. If the photo-ion is left in its ground state, the photo-electron has energy $E_e = h\nu - I_p$ (Binding energy $= I_p$). If the ion is left in an excited state, the photo-electron energy is correspondingly reduced (binding energy increase in figure 1.4). If the photo-ion is left in a bound electronic state (e.g. blue curve), the vibrational structure is reflected in the photoelectron spectrum, with each line corresponding to a different vibrational state of the ion. If the photo-ion is left in a dissociative electronic state with asymptote $A + B^+$ or $B + A^+$, a continuum is observed in the photoelectron spectrum. If a molecule is prepared in an excited state and subsequently ionized in a pump-probe experiment, the photoelectron spectrum and photoion fragmentation pattern will depend on the time dependent Franck-Condon factors and dipole matrix elements between the excited state(s) of the molecule and the excited states of the ion.

The ionization potential and excited state energies of a molecule scale as $\sim 1/R_m^2$, where R_m is the characteristic size of the molecule. For small molecules (e.g. O_2, H_2O, N_2, C_2H_4) this typically puts the first absorption band in the 7 to 11 eV range, and the ionization potential between 10 and 15 eV. Photo-electron and photo-ion spectra contain a great amount of information, and much of what we know about molecular physics comes from photoionization studies. Most of this work has been carried out with discharge lamps or synchrotron XUV light sources. These sources are temporally incoherent and do not produce the femtosecond pulses necessary for time-resolved studies.

1.3 High Order Harmonic Generation

1.3.1 Microscopic Physics: The Single Atom Response

Lasers can produce light with spatial and temporal coherence. In order to build a laser that produces femtosecond pulses, a gain medium with a high gain bandwidth is required. For an output pulse of full widh at half maximum (FWHM) Δt_{FWHM}, the spectral bandwidth $\Delta\omega_{\mathrm{FWHM}}$ must satisfy the relation

$$\Delta t_{\mathrm{FWHM}} \Delta\omega_{\mathrm{FWHM}} = 4\ln(2) \tag{1.14}$$

The power needed to produce a population inversion in a laser, in general, scales as $\sim 1/\lambda^4$ [19]. Thus, it is easy to build lasers in the infrared, somehwat more difficult but quite manageable in the visible, and extremely difficult in the VUV and XUV. At the time of this writing, the best femtosecond laser technology is in the near infrared, based on either Ti:Sapphire solid state lasers or Yb^+ doped fiber lasers. A few heroic demonstrations to get high bandwidth gain in the VUV and XUV [20, 21] have been reported, but the $1/\lambda^4$ pump power scaling presents a severe limitation.

An alternative route to getting laser-like radiation at short wavelengths is to start with an infrared laser and convert the light to shorter wavelengths through nonlinear optics.

In linear optics, the polarization density P of the optical medium obeys the principle of superposition: $P(E_1+E_2) = P(E_1)+P(E_2)$. The optical properties of the medium are thus unmodified by the electric fields E_i; E_1 produces the same response whether E_2 is present or not. The familiar optical phenomena of reflection and refraction are linear. Departures from linearity can be mathematically described by Taylor expanding the polarization beyond the linear term [22, 23]:

$$P = \chi^{(1)}E + \chi^{(2)}E^2 + \chi^{(3)}E^3 + ... \tag{1.15}$$

where the coefficients $\chi^{(k)}$ are called the kth order susceptibilities. The higher order terms can give rise to a polarization, and thus radiation, at new frequencies. For example, inserting an electric field of the form $E_0\cos(\omega t)$ into the second order term gives:

$$P^{(2)} = \chi^{(2)}E_0^2\cos^2(\omega t) = \chi^{(2)}E_0^2\left(\frac{1+\cos(2\omega t)}{2}\right) \tag{1.16}$$

and there is now polarization oscillating at twice the drive frequency, the second harmonic. "$\chi^{(3)}$ processes" include third harmonic generation, self phase modulation, and other phenomena described by the third order term. Starting from robust lasers in the near infrared, use of $\chi^{(2)}$ and $\chi^{(3)}$ processes to produce femtosecond pulses down to ~ 200 nm wavelengths is now routinely implemented in many laboratories.

To produce shorter wavelengths, we must look at what happens as the electric field strength is increased, and more and more terms must be considered in the expansion. The successive terms in the expansion (1.15) can be derived from quantum mechanical perturbation theory [22, 23]. If transitions to the continuum (ionization) are ignored, for an atomic system with resonance frequency ω_0 driven by light at frequency ω and amplitude E, the successive terms are approximately related through the simple expression [1]:

$$\frac{\chi^{(k+1)}E^{k+1}}{\chi^{(k)}E^k} \approx \frac{\mu E}{\hbar\Delta} \approx \frac{eEa_B}{\hbar\Delta} \tag{1.17}$$

where $\mu \approx ea_B$ is the dipole matrix element for a bound-bound transition with frequency detuning $\Delta = |\omega - \omega_0|$, $a_B = 0.529$ Å is the Bohr radius. For detunings of a few eV, as is the case for driving an atomic system in the optical or near infrared, the ratio (1.17) approaches unity for electric fields on the order of few V/Å, or light intensities in the 10^{14} W/cm^2 range. Thus, at these intensities the perturbation expansion is of a little use: The field is no longer a perturbation.

In fact, perturbation theory is frustrated at slightly lower laser intensities than indicated by (1.17) because ionization of the atom cannot be ignored. Figure 1.5 shows the potential experienced by the electron of a hydrogen atom ($V = -1/r$ in atomic units), in a strong electric field ($V = -Ex$), for several values of the field. As the field strength increases, the potential barrier is lowered and made shorter, leading to quantum mechanical tunneling of the electron wave function to the continuum. To estimate the importance of tunneling in an oscillating field, one uses the Keldysh scale parameter [24]:

$$\frac{1}{\gamma} = \frac{eE}{\omega\sqrt{2mI_p}} = \frac{eEa}{\hbar\omega_0} \tag{1.18}$$

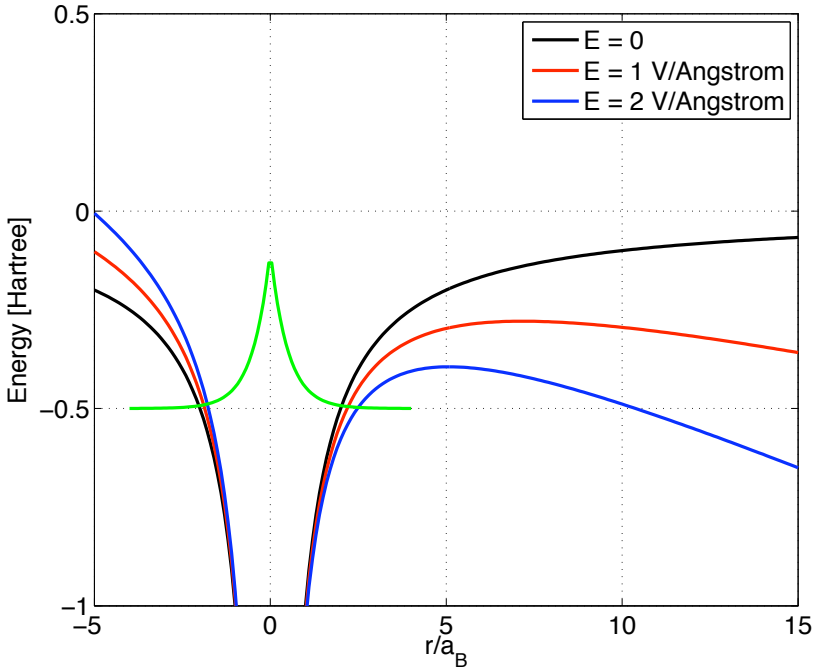

Figure 1.5: **Atom in a Strong Electric Field** The superposition of the Coulomb potential of a hydrogen atom ($V = -1/r$) and a strong electric field ($V = -Ex$) is plotted for three values of the elctric field in atomic units. Also shown is the 1s orbital of hydrogen at E = -1/2 Hartree (green curve). As the field strength increases, the electron can tunnel through the potential barrier to the continuum.

where $a \equiv \hbar/\sqrt{2mI_p}$ is now a "generalized Bohr radius" [1] for an atom with ionization potential I_p. The Keldysh parameter γ^{-1} represents the ratio of the tunneling rate for the electron through the potential barrier of figure 1.5 to the laser period. For $\gamma^{-1} \ll 1$, ionization can be described perturbatively as the absorption of multiple photons. For γ^{-1} of order unity or greater, the so-called "strong-field regime", it is much more appropriate to describe the ionization process as tunneling occurring at the maxima of the electric field.

When an atom is subjected to a laser field in the strong-field regime, a dipole moment $d(\omega)$ with very high order harmonic content can be produced. The basic phenomena is well described by the semi-classical three-step model pioneered by Corkum [25] and Lewenstein [26], and illustrated in figure 1.6. The emission of high energy photons can be understood by considering the dynamics of tunnel-ionized electrons over one half cycle of the laser field. Near the maximum in the electric field, atoms are tunnel-ionized. A free electron is born with zero initial velocity and starts to move in the strong electric field. Many of the possible classical electron trajectories do not return to the vicinity of the atom. However, the ones that do return have a chance for radiative recombination producing a short burst of light and a dipole $d(\omega)$ with high frequency spectral content. The burst occurs

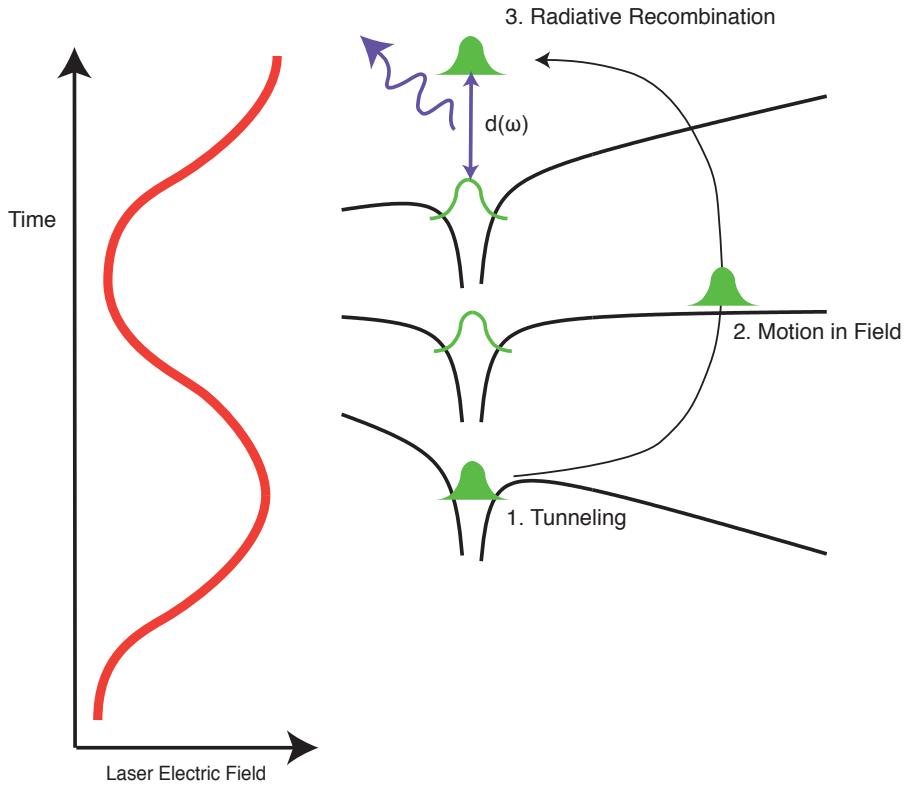

Figure 1.6: **Three Step Model of High Order Harmonic Generation.** A schematic evolution of the atomic potential and electron wave-packet in a strong electric field. Atoms are tunnel-ionized near a peak in the electric field. The electron can then gain kinetic energy from motion in the field and recombine, emitting a high energy photon.

near the zero crossings of the laser electric field [1, 27]. The dipole for a single attosecond burst is sketched on the left side of figure 1.7 in the time and frequency domains. The spectrum exhibits a plateau up to an abrupt cutoff. The cutoff energy can be calculated from consideration of the classical trajectories and is given by:

$$\hbar\omega_c = 3.17U_p + I_p \tag{1.19}$$

where the pondermotive energy U_P is defined:

$$U_p = \frac{e^2E^2}{4m\omega_0^2} \tag{1.20}$$

The parameters E and ω_0 refer to the driving electric field amplitude and frequency, respectively. The Pondermotive energy represents the time average of the kinetic energy of the free electron in the laser field.

An analogy can be made between our driven atom and a child on a swingset. When pushed lightly, the swing executes a damped simple harmonic motion at frequency

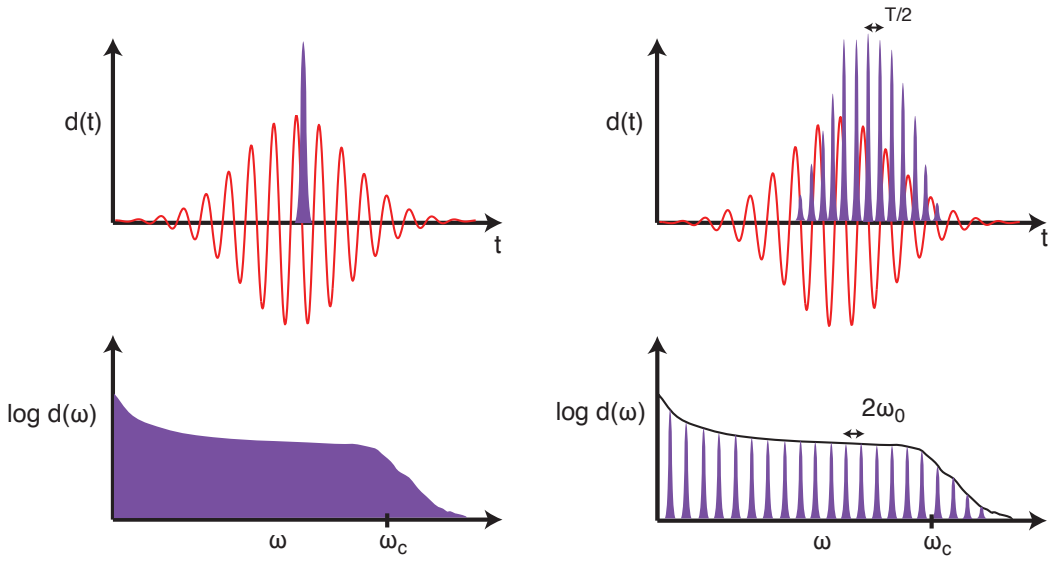

Figure 1.7: **High Order Harmonic Spectra.** Left: The time dependent dipole $d(t)$ and its spectral content $d(\omega)$ from one tunnel-ionization/recombination event. The very short burst has a broad spectrum extending out to the cutoff determined by equation (1.19). Right: The spectral interference of multiple attosecond bursts modulates the broad spectrum into harmonics of the fundamental driving laser. The red line shows the electric field of an infrared drive laser, with attosecond XUV bursts occuring every half cycle (T/2) on the zero crossings of the electric field. The spacing of the harmonics in frequency is then $2\omega_0$.

ω (linear optics). As the pushing force increases, the amplitude of the oscillations increases and the true response of the swing is revealed to not be a perfect sinusoid, with a spectrum containing some harmonics of ω (nonlinear optics). The strong field regimes corresponds to ripping the swing off its hinges and slamming it into the ground at full speed. The short burst of screaming as the child hits the ground extends to high frequency.

Under normal experimental conditions with multi-cycle drive laser pulses, the tunnel-ionization probability per half cycle is small, and the process repeats, producing an attosecond burst every half cycle ($T/2$). The spectral interference of successive bursts then modulates the spectrum $d(\omega)$ with modulation period $2\pi(2/T) = 2\omega_0$. Since $d(\omega)$ will also have a (linear) component at drive laser frequency ω_0, and peaks in the spectrum are spaced by $2\omega_0$, $d(\omega)$ consists of odd harmonics of the laser frequency. If this spectral modulation seems strange to you, recall the interference patterns produced on a screen after the illumination of slits with coherent light [28]. If one slit of finite width a is illuminated, a broad maximum is observed on the screen with width proportional to $1/a$. If N such slits with spacing b are illuminated, the broad maximum is modulated into narrow peaks with spacing $\propto 1/b$ and width $\propto 1/N$. Mathematically, in the Fraunhofer limit, the diffraction pattern is determined from the Fourier transform of the aperture function (the slits). In our case, $d(\omega)$ and $d(t)$ are a Fourier transform pair, and N attosecond pulses interfere to

produce a spectrum with harmonic peaks spaced by $2\omega_0$ and width $\sim 1/N$.

In contrast with the $1/\lambda^4$ pump power scaling required to achieve lasing at wavelength λ, the cutoff photon energy of (1.19) scales linearly with intensity, so that in principle the drive laser power required to reach a given wavelength scales much more favorably as $1/\lambda$. Indeed, with modest focused femtosecond laser pulse energies (~ 100 μJ), the cutoff in $d(\omega)$ can easily be made to extend into the soft-xray. To determine the actual radiation that is produced in HHG, we must consider an ensemble of such driven atoms.

1.3.2 Macroscopic Physics: Ionization and Phase Matching

The high order harmonic dipole moment of a single atom driven with the strong field process described above is extremely weak. In atomic units, the single atom dipole $d(\omega)$ is on the order of 10^{-3} to 10^{-5} [25]. For comparison, the dipole moment of an atom participating in a helium-neon laser is order unity or larger [19]. Bright high order harmonic generation (HHG) can only be obtained from the coherent superposition of emission from many atoms. In principle, HHG can be observed from any target capable of the tunnel-ionization/recombination process discussed above. HHG has been observed from noble gas atoms, solid surfaces [29], clusters of atoms [30], and molecules [31]. However, for several reasons, the medium of choice for HHG is usually a noble gas.

The first reason is survival. Noble gas atoms have the highest ionization potentials in the periodic table, allowing them to survive the rising edge of a laser pulse without being ionized early in the pulse while the intensity is still in the multiphoton ionization regime ($1/\gamma \ll 1$). An ensemble of atoms with lower I_p might be completely ionized before they even see the portion of the pulse corresponding to the strong field regime. This also explains why HHG is generally not observed with longer laser pulses of comparable peak intensity in the picosecond or nanosecond regime. The rise time of these pulses is too slow, and all the atoms are ionized early in the pulse before the intensities needed for HHG are reached.

The second reason for noble gas atoms, as opposed to molecules which might also have a high I_p, is that they are spherically symmetric. For molecules, the phase of the high harmonic dipole depends on the orientation of the molecule with respect to the drive laser electric field vector [31]. For an un-aligned molecular ensemble at room temperature, the molecules are randomly oriented, and their dipoles combine incoherently with random phases. Adjacent atoms have no such problem, and radiate with a phase determined only by the drive field.

To call any HHG apparatus "standard" is dangerous, as both laser technology and HHG tricks are still evolving, but a common arrangement is depicted in figure 1.8. Femtosecond driver laser pulses, amplified to the 0.1-1 mJ range, are focused in vacuum with a ~ 1 m lens to $\sim 10^{14}$ W/cm^2. A noble gas target is introduced near the focus either with a small nozzle backed by high pressure or a short tube with pinholes for the laser to enter and exit. The harmonics and the driving laser diverge after the focus. Sufficiently far away from the focus to avoid damage, a thin metallic foil is inserted in the beam to block the fundamental and transmit the XUV light. I will return to more of the technical details of such a system in chapter 2. Now, lets look at some of the equations describing how we get from a single atom response to a usable electric field. In the gas medium, the polarization density P induced is the single atom dipole moment d times the number density of atoms

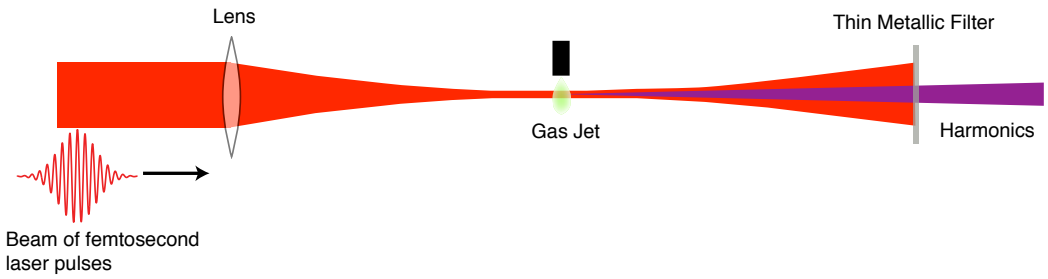

Figure 1.8: **An HHG Apparatus.** Infrared femtosecond laser pulses are focused into a gas to achieve intensities in the strong field regime. A metallic filter blocks the fundamental and low harmonic orders.

ρ.

$$P = \rho d \tag{1.21}$$

The evolution of the electric field $\vec{E}$ in the gas medium is governed by Maxwell's wave equation [22, 23]:

$$-\nabla^2 \vec{E} + \frac{1}{c^2}\frac{\partial^2 \vec{E}}{\partial t^2} = -\frac{4\pi}{c^2}\frac{\partial^2 \vec{P}}{\partial t^2} \tag{1.22}$$

where c is the speed of light in vacuum. If $\vec{P} = 0$, the solution of the wave equation will be the free space propagation of the driver laser field. In the gas medium, $\vec{P} \neq 0$, and equation (1.22) is a driven wave equation. For now, I will neglect the pulse structure of the field and write the electric field and polarization as a superposition of waves at the fundamental frequency of the drive laser and its odd harmonics.

$$\vec{E}(\mathbf{r}, t) = \sum_q \vec{E}_q(\mathbf{r}) e^{-i\omega_q t} \tag{1.23}$$

$$\vec{P}(\mathbf{r}, t) = \sum_q \vec{P}_q(\mathbf{r}) e^{-i\omega_q t} \tag{1.24}$$

Insertion of this into the wave equation yields a coupled set of driven wave equations for the frequency components.

$$\nabla^2 \vec{E}_q(\mathbf{r}) + \omega_q^2/c^2 E_q(\mathbf{r}) = -\frac{4\pi\omega_q^2}{c^2}\vec{P}_q(\mathbf{r}) \tag{1.25}$$

If $\vec{P}_q(\mathbf{r})$ were that of single atom represented by a polarization density of infinitesimal spatial extent, the solution to (1.25) would be the familiar dipole radiation pattern [32]. The propagation of the drive laser through the gas medium sets up a phased array of these atomic dipoles, described by $\vec{P}_q(\mathbf{r})$, which add coherently to produce a radiation pattern $\vec{E}_q(\mathbf{r})$ that solves the wave equation. In order to have bright harmonic emission from the gas, the atomic dipoles generated by the laser must be arranged to add in phase. Controlling the parameters of the laser and medium so that the dipoles add in phase is termed *phase matching*.

To allow us to get a feel for the problem, lets make the simplification that the electric field is made up of linearly polarized plane waves with amplitudes that vary along the propagation direction of the laser (taken to be the z-axis):

$$\vec{E}(\mathbf{r},t) = \hat{\mathrm{x}} \sum_q A_q(z) e^{i(k_q z - \omega_q t)} e^{-\alpha_q z} \tag{1.26}$$

where k_q and α_q represent the wavenumber and field attenuation coefficient in the medium such that $(k_q + i\alpha_q)^2 = \epsilon^{(1)}\omega_q^2/c^2$, and $\epsilon^{(1)}(\omega_q)$ is the linear dielectric constant of the medium. The field attenuation coefficient is related to the photo-absorption cross section, σ, of the atoms via $2\alpha_q = \rho\sigma$. Separating the polarization into linear and nonlinear components,

$$\vec{P}(z,t) = \vec{P}^{(1)} + \vec{P}^{NL} = \hat{x} \sum_q \left(P_q^{(1)}(z) + P_q^{(NL)}(z) \right) e^{-i\omega_q t} \tag{1.27}$$

yields the coupled wave equations [22, 23]:

$$\left(\frac{d^2 A_q}{dz^2} + 2ik_q \frac{dA_q}{dz} \right) e^{(ik_q - \alpha_q)z} = -\frac{4\pi\omega_q^2}{c^2} P_q^{NL}(z) \tag{1.28}$$

Now, in general, the first term in equation (1.28) is much smaller than the second because the amplitude of the harmonic field will change on a length scale much larger than its wavelength. This is called the *slowly varying envelope approximation* [22]. Neglecting the first term, the wave equations simplify to:

$$\frac{dA_q}{dz} = \frac{2i\pi\omega_q^2}{k_q c^2} P_q^{NL}(z) e^{(-ik_q + \alpha_q)z} \tag{1.29}$$

The nonlinear polarization is produced by the drive laser and the phase of the nonlinear polarization is directly related to the phase of the drive laser. In the semiclassical Lewenstein model [26], the phase of the nonlinear polarization with respect to the driving laser is

$$\Phi_q = q\omega_0 t_f - \frac{1}{\hbar} S \tag{1.30}$$

where S is the quasi-classical action integral for the motion of the electron in the laser field [33] and t_f is the return time of the electron's classical trajectory with respect to a fixed phase of the laser. In the strong field approximation ($1/\gamma \gg 1$), the action can be approximated as $\mathrm{S} \approx -U_p\tau$, where τ is the time the laser spends in the field between ionization and recombination. As the laser propagates the phase then evolves with z as:

$$\Phi(z) \approx \Phi_0 + \frac{d\Phi}{dz} z = \Phi_0 + \left[q\frac{d}{dz}(\omega_0 t_f) + \frac{d}{dz} U_p \tau \right] \tag{1.31}$$

$$= \Phi_0 + \left[qk_0 + \alpha_q^j \frac{dI}{dz} \right] z \tag{1.32}$$

where I is the laser intensity and α_q^j is a coefficient that depends on the harmonic order and the classical trajectory, or "quantum path" [34, 35]. Since $\omega_0 t_f$ is simply a phase with

respect to the laser phase, it evolves the same as the laser phase, and $d(\omega_0 t_f)/dz = k_0$. The RHS of equation (1.29) can then be written

$$P_q^{NL}(z)e^{-ik_q z} = \rho\,|d(\omega_q)|\,e^{i\Delta k z} \tag{1.33}$$

where

$$\Delta k = (qk_0 - k_q) + \alpha_q^j \frac{dI}{dz} \tag{1.34}$$

The term in parentheses is the standard expression for the wave-vector mismatch encountered in perturbative non-linear optics. The last term accounts for the fact that the phase of the high order harmonic dipole also depends on the intensity of the light. The phase factor $\Delta k z$ represents the phase slip between harmonics generated at two points in the medium separated by a distance z. The separation at which the harmonics generated at two points destructively interfere is called the *coherence length*.

$$L_c = \frac{\pi}{\Delta k} \tag{1.35}$$

Likewise, the absorption length is defined as the propagation length at which the harmonic intensity $|E_q(L)|^2$ will be reduced by $1/e$ in the absence of a nonlinear polarization:

$$L_{\text{abs}} = \frac{1}{\rho\sigma} = \frac{1}{2\alpha_q} \tag{1.36}$$

Equation (1.29) can be integrated for the electric field amplitude at the exit of the medium. From our definition of $\vec{E}$ in equation (1.26), the magnitude of E_q at the exit of the medium is [36]:

$$\begin{aligned} E_q(L) &= A_q(L)e^{-\alpha_q L} \\ &= e^{-\alpha_q L} 2\pi i k_q \rho\,|d_q| \int_0^L dz e^{(i\Delta k + \alpha_q)z} \\ &= 2\pi i k_q \rho\,|d_q|\,\frac{1}{i\Delta k + \alpha_q}\left(e^{i\Delta k L} - e^{-\alpha_q L}\right) \end{aligned} \tag{1.37}$$

The intensity of the harmonic light exiting the medium is plotted as a function of medium length for several values of Δk in figure 1.9. For perfect phase matching with $\Delta k = 0$, the harmonic emission from all the atoms in the medium add coherently. The yield that can be achieved rapidly drops off as Δk becomes non-zero and harmonics generated in different regions of the medium add out of phase.

As we will see in more detail in chapter 2, the main source of phase mismatch is the difference in phase velocity between the harmonic and fundamental fields in the medium. The phase velocity for a light field is given by $c/n(\omega)$, where $n(\omega)$ is the index of refraction for waves at frequency ω. The wave vector k_q is

$$k_q = n(\omega_q)\frac{\omega_q}{c} \tag{1.38}$$

The first term in (1.34) then becomes

$$qk_0 - k_q = qn(\omega_0)\frac{\omega_0}{c} - n(\omega_q)\frac{q\omega_0}{c} = q\frac{\omega_0}{c}\left[n(\omega_0) - n(\omega_q)\right] \tag{1.39}$$

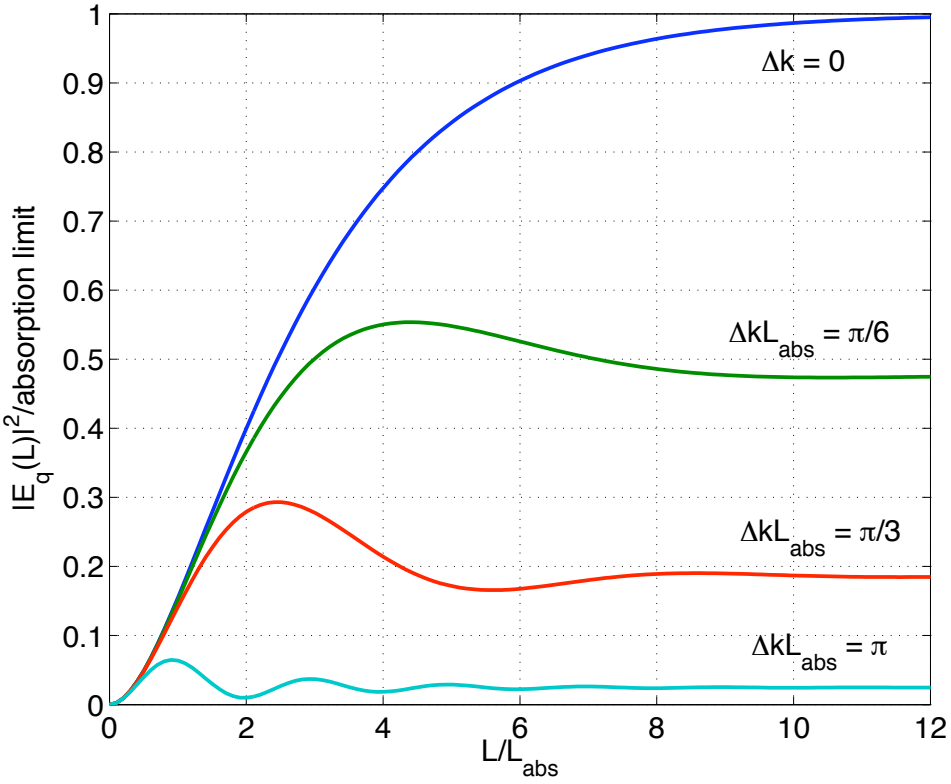

Figure 1.9: **Effects of Phase Mismatch.** The high order harmonic intensity $|E_q(L)|^2$ as a function of normalized medium length L/L_{abs}. For $\Delta k = 0$, the harmonic yield reaches a limit where the rates of harmonic emisison and absorption are equal. The attainable yield rapdily drops as Δk becomes non-zero.

As ω_q increases into the soft x-ray, $n(\omega_q)$ tends towards one, while the index of refraction at the optical drive wavelength, $n(\omega_0)$, remains fixed. For a finite index of refraction difference, the phase slip then increases linearly with q. This explains why phase matching becomes increasingly more difficult as the harmonic order increases. Driving a single atom dipole $d(\omega)$ that extends out into the soft x-ray is not difficult, simultaneously achieving phase matching is.

1.3.3 Absorption Limited HHG

Even for perfect phase matching, the harmonic yield in figure 1.9 is observed to plateau. This is due to absorption. The absorption rate of photons from the harmonic field by gas atoms scales as the number of photons in the field, whereas the harmonic emission rate does not. As the driving pulse propagates and the harmonic field grows, the harmonic absorption rate approaches the harmonic emission rate and the harmonic intensity approaches a maximum.

The saturation of the harmonic yield with increasing medium length indicates that there is not much to be gained by making the noble gas medium much longer than a few absorption lengths. Constant [36] proposed the criterium for absorption limited HHG:

$$L > 3L_{\text{abs}} \tag{1.40}$$

This indicates a density-length product of

$$\rho L > \frac{3}{\sigma} \tag{1.41}$$

For a typical XUV absorption cross section of $\sigma \sim 10$ Mb, this indicates a density length product of $\sim 3 \times 10^{17}$ atoms/cm^2 or a pressure-length product of ~ 10 Torr-cm at room temperature. The case of phase matched, absorption limited HHG corresponds to medium lengths that are simultaneously short compared to the coherence length $1/\Delta k$, and optically thick,

$$\frac{1}{\alpha_q} \ll L \ll \frac{1}{\Delta k} \tag{1.42}$$

We can use equation (1.37) to estimate an upper limit for the flux of HHG that can be emitted from the medium per unit area per unit time. The field attenuation coefficient, α_q is related to the photon absorption cross section σ through $\alpha_q = \rho\sigma/2$. Inserting this into equation (1.37), and taking the approiate limit, we get

$$E_q(L) = 4\pi i k_q \left|d_q\right| / \sigma \tag{1.43}$$

The maximum number of photons per unit area per unit time that can be emitted from the medium is thus

$$J_{\max} = \frac{1}{\hbar\omega}\left(\frac{c}{8\pi}\left|E_q\right|^2\right) = \frac{2\pi k_q}{\hbar}\frac{\left|d_q\right|^2}{\sigma^2} \tag{1.44}$$

Plugging in some rough numbers, $|d_q|^2 \sim 10^{-8}$ a. u. [25], $\sigma \sim 5 \times 10^{-18}$ cm^2, $\lambda_q = 30$ nm, gives $\sim 2 \times 10^3$ photons per square micron per femtosecond of phased matched harmonic emission. Consider a 1 mJ, 50 fs laser pulse focused to a diamter of ~ 100 μm for an intensity of $2{\times}10^{14}$ W/cm^2. If phase matched harmonic generation can be achieved for 10 fs over the focal area of $\sim (100\ \mu\text{m})^2$, $\sim 2 \times 10^8$ photons per harmonic per pulse are produced, or about 1 nJ/harmonic/pulse for a conversion efficiency of 10^{-6}. The optimization of high order harmonic generation has been an active area of research for over 15 years now and still is. In the literature, values an order of magnitude higher [36, 37] than this estimate have been claimed, but a conversion efficiency of $\sim 10^{-6}$ is a good working estimate for practical applications [38] for photon energies in the 20 to 40 eV range.

It should be noted that the absorption limit is not a constant across the harmonic spectrum. The absorption cross section of an atom decreases away from the ionization threshold, so that higher harmonic orders may actually have a larger absorption limited flux. I will return to this in section 2.4.

Chapter 2

High Order Harmonics Beamline

As you know, you go to war with the army you have. They're not the army you might want or wish to have at a later time.

- Secretary of Defense Donald Rumsfeld

The absorption cross sections of atoms and molecules are the highest in the VUV and XUV. In a material of solid density, a typical absorption length is $\sim$ 100 nm. This makes XUV optics dismally inefficient. With no contamination, a good multilayer mirror might have a reflectivity of $\sim$ 30% and a filter, as shown in figure 1.8, a transmission of 50 % [39]. In a real world vacuum environment, the the transmission can be as low as 10 %.

In the last chapter, I made an estimate for the XUV yield from a typical high order harmonic generation source using 1 mJ driver pulses of 2×10^8 photons/harmonic/shot. In practice with the losses, of filters, gratings, and optics, one might get to utilize 10^7 photons/shot (or less) in a an experiment [40, 38]. Typical absorption cross sections in the XUV are of order 10 Mb = 10^{-17} cm^2. If the harmonics can be focused to an area of $\sim (10\ \mu\text{m})^2$ (see chapter 3), the fraction of molecules η at the focus that absorb a photon is roughly

$$\eta = F\sigma = \frac{10^7 \text{ photons}}{(10\ \mu\text{m})^2} \times 10 \text{ Mb} = 10^{-4} \tag{2.1}$$

The probability of a molecule absorbing two photons in a pump/probe experiment then scales as $\eta^2 \sim 10^{-8}$ and is extremeley low. Lets look at the approximate expression we derived for the absorption limit in HHG (1.44), and see how we can get more photons to work with.

$$N_\gamma \approx J_{max} A \Delta t = \frac{2\pi k_q}{\hbar} \frac{|d_q|^2 \Delta t}{\sigma^2} A \tag{2.2}$$

In this expression k_q and d_q are the harmonic wavevector and atomic dipole phase, A is the focal area over which harmonics are emitted efficiently, and Δt is the duration that efficient harmonic generation can be achieved.

Since the HHG atomic dipole $d(t)$ is initiated by tunnel ionization, the strength of the atomic dipole moment roughly scales with the instantaneous tunnel ionization amplitude. The instantaneous dipole strength $d(t)$ can thus be increased by increasing the

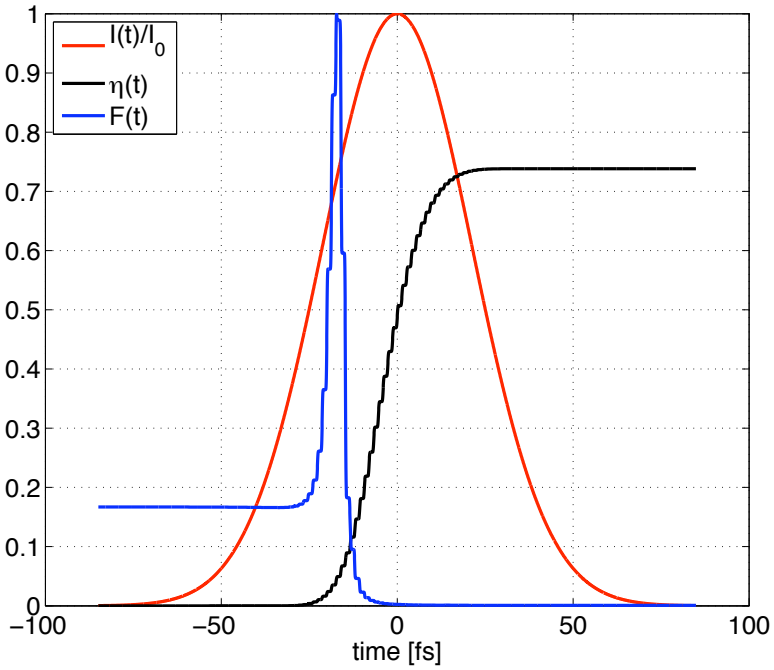

Figure 2.1: **Time Dependent Ionization and Phase Matching.** The ionized fraction of Kr atoms ($\eta(t)$, black curve) is plotted as a function of time for a 50 fs, 800 nm laser pulse ($I(t)$, red curve) with peak intensity 2×10^{14} W/cm^2. Over 70% of the atoms are ionized by the end of the pulse. The time dependent phase matching factor for the 19th harmonic ($F(t)$, blue curve) peaks when the dispersion of the plasma balances that of the neutral atoms, and goes to zero as the ionization increases. The simulation parameters are made to emulate a tightly focused beam in a short gas jet: $L = 1$ mm, $z_c = 0.5$, $z_R = 1.2$ cm, $\rho = 3.2 \times 10^{18}$ atoms/cm^3 (100 Torr), and $|\alpha_q^j| = 1 \times 10^{-14}$ cm^2/W. More details on the calculation of Δk and F appear in section 2.1.

laser intensity. However, this will cause the medium to ionize more rapidly. In addition to depleting the number of atoms available for HHG, ionization of the gas produces a free electron plasma. The plasma has a non-unity index of refraction and contributes to the phase mismatch factor Δk. This is illustrated in the simulation of Kr atoms in a 50 fs laser pulse with a peak intensity of 2×10^{14} W/cm^2 shown in figure 2.1. The ionization rate is calculated at each time step using the expression of Ammonosov, Delone, and Krainov [41, 25] for tunnel ionization (the so-called "ADK" rate). The ionization fraction, $\eta(t)$, is plotted in black. Also shown is the time dependent phase matching factor [36, 42] derived from equation (1.37):

$$F_q(t) = \left| \frac{\alpha_q L e^{\alpha_q L}}{(i\Delta k(t) + \alpha_q)L} \left(e^{i\Delta k(t) L} - e^{-\alpha_q L} \right) \right|^2 \tag{2.3}$$

The factor $F(t)$ is the ratio of the harmonic yield to what could be attained with $\Delta k = 0$. $F(t)$ exhibits a transient peak at a degree of ionization where dispersion due to the neutral gas atoms and the plasma electrons balance. As the ionization increases, the plasma dispersion rapidly forces F to zero. This creates a so-called "ionization gate" [43] on the harmonic emission. If the peak intensity of the pulse is increased or the ionization potential of the target gas is reduced, ionization occurs faster. The peak in $F(t)$ is shifted earlier in the pulse to lower intensity and becomes narrower. The balance between the strength of the dipole and ionization sets a practical limit on the product $|d_q|^2\Delta t$ that can be obtained, and the harmonic yield in an optically thick medium where phase matching is important is relatively insensitive to intensity [36]. Gains can be made, however, by using shorter driver pulses so that the atoms can be exposed to a higher intensity with less plasma density [1].

The approach taken in this work to increase the HHG yield for pump/probe studies is to scale the focal area A by loosely focusing ($f = 6$ m) high energy (30 mJ) laser pulses [37, 44, 45]. In the next section I will discuss the different factors contributing to the phase slip Δk and their scaling with focal area and target density. We will determine the appropriate scaling to apply to the noble gas medium to optimize phase matching and limit the divergence of the beam.

2.1 Phase Matching Factors

From equation (1.32), the phase of the nonlinear polarization generated by the laser is

$$\Phi(z) \approx \Phi_0 + \frac{d\Phi}{dz}z = \Phi_0 + \left[q\frac{d}{dz}\Phi_{\text{Laser}} + \alpha_q^j\frac{dI}{dz}\right] \tag{2.4}$$

In chapter 1, I considered a plane wave for the drive laser, and used $d\Phi_{\text{Laser}}/dz = k_0$. A better assumption is that the drive laser is actually a focused Gaussian beam. In cylindrical coordinates, the electric field $E(r, z, t)$ takes the form [22]:

$$E(r, z, t) = E_0\frac{w_0}{w(z)}e^{-r^2/w^2(z)}e^{ik_0r^2/2R(z)}e^{i(k_0z+\Phi_G(z)}e^{-i\omega_0t} \tag{2.5}$$

where

$$w(z) = w_0\left[1 + \left(\frac{z}{z_R}\right)^2\right]^{1/2} \tag{2.6}$$

is the z-dependent $1/e^2$ radius of the intensity distribution. The radius of curvature of the phase fronts is

$$R(z) = z\left[1 + \left(\frac{z}{z_R}\right)^2\right] \tag{2.7}$$

and the Gouy phase is

$$\Phi_G(z) = -\tan^{-1}(z/z_R) \tag{2.8}$$

The Rayleigh range $z_R = \pi w_0^2/\lambda_0$ describes the depth of focus of the Gaussian beam. The phase of a focused Gaussian laser beam on axis ($r = 0$) is

$$\Phi_{\text{Laser}}(z) = k_0z - \tan^{-1}\left(\frac{z}{z_R}\right) \tag{2.9}$$

Setting the cell position at $z = z_c$, the phase evolution of the laser at the gas cell is

$$\left.\frac{d\Phi_{\text{Laser}}}{dz}\right|_{z=z_c} = k_0 - \frac{1}{z_R}\frac{1}{1+(z_c/z)^2} \tag{2.10}$$

The on-axis intensity of the laser varies with z as

$$I(z) = I_{\text{peak}}\frac{w_0^2}{w^2(z)} = I_{\text{peak}}\frac{1}{1+(z/z_R)^2} \tag{2.11}$$

so

$$\left.\frac{dI}{dz}\right|_{z=z_c} = -\frac{2I_{\text{peak}}}{z_R}\frac{z_c/z_R}{1+(z_c/z_R)^2} \tag{2.12}$$

The expression for Δk then becomes

$$\Delta k = q\frac{\omega_0}{c}\left[n(\omega_0) - n(\omega_q)\right] - \frac{q}{z_R}\frac{1}{1+(z_c/z)^2} + \frac{2|\alpha_q^j|I_{\text{peak}}}{z_R}\frac{z_c/z_R}{1+(z_c/z_R)^2} \tag{2.13}$$

where I have written the intensity dependent phase coefficient α_q^j as $-|\alpha_q^j|$ [33]. The intensity dependent phase coefficient α_q^j depends on whether the harmonic is in the plateau or cutoff region of the spectrum and the "quantum path" dominating the single atom dipole [34, 35]. For harmonics in the plateau, $|\alpha_q^j|$ is 1×10^{-14} cm^2/W for the short quantum path and 25×10^{-14} cm^2/W for the long quantum path [34]. It is convenient to separate the difference in index of refraction into two components, one due to the dispersion of the noble gas atoms and one due to the free electron plasma that is created upon ionization.

$$\begin{aligned} q\frac{\omega_0}{c}\left[n(\omega_0) - n(\omega_q)\right] &= q\frac{\omega_0}{c}\left[n(\omega_0) - n(\omega_q)\right]_{\text{atomic}} + q\frac{\omega_0}{c}\left[n(\omega_0) - n(\omega_q)\right]_{\text{plasma}} & (2.14)\\ &= \Delta k_{\text{atomic}} + \Delta k_{\text{plasma}} & (2.15)\end{aligned}$$

The index of refraction for a gas can be expressed in terms of the atomic scattering factors f_1^0 and f_2^0 [39]:

$$n(\omega) - 1 = -\rho\frac{r_0\lambda^2}{2\pi}\left(f_1^0(\omega) - if_2^0(\omega)\right) \tag{2.16}$$

To determine the wavevector mismatch, we are only interested in the real part of n. Using the relation $\lambda_q = \lambda_0/q^2$ for the wavelengths in vacuum, gives

$$\begin{aligned}\Delta k_{\text{atomic}} &= q\frac{\omega_0}{c}\left[n(\omega_0) - n(\omega_q)\right]\\ &= -q\rho r_0\lambda_0\left(f_1^0(\omega_0) - \frac{1}{q^2}f_1^0(\omega_q)\right) & (2.17)\end{aligned}$$

Table 2.1 table lists the atomic scattering factors for the fundamental and high harmonics of 800 nm divided by q^2. From table 2.1, it is clear that refraction at the drive laser and harmonic wavelengths both contribute to Δk_{atomic}.

The gas medium is rapidly ionized by the drive laser pulse in the HHG process. This forms a free electron plasma with time dependent plasma frequency

$$\omega_p^2(t) = \eta(t)\frac{4\pi\rho e^2}{m} \tag{2.18}$$

	$10^2 \times f_1^0(\omega_q)/q^2$ for $q =$										
q	1	3	5	...	19	21	23	25	27	29	31
Ar	-3.8	-4.1	-4.9		2.0	2.3	2.2	2.1	1.5	1.1	0.9
Kr	-5.8	-6.4	-8.3		3.0	2.6	2.2	1.8	1.5	1.2	1
Xe	-9.4	-9.4	-9.4		2.6	1.9	1.5	1.1	0.8	0.6	0.4

Table 2.1: **Atomic Scattering Factors**. Atomic scattering factors divided by q^2 for the fundamental and harmonics of 800 nm for Ar, Kr, and Xe gasses. For harmonics 19-31, the data is from [46]. For the fundamental, 3rd, and 5th harmonic, f_1^0 is calculated from the Sellmeier coefficients of [47].

The free electron plasma has an index of refraction given by [48]

$$n(\omega) = \sqrt{1 - \frac{\omega_p^2}{\omega^2}} \tag{2.19}$$

For the optical and XUV frequencies of the drive laser and the harmonics and gas densities used for HHG, $\omega_p \ll \omega$ and

$$n(\omega) - 1 \approx -\frac{1}{2}\frac{4\pi\rho e^2}{m\omega^2} \tag{2.20}$$

The time dependent phase mismatch due to the free electron plasma is then

$$\begin{aligned} \Delta k_{\text{plasma}}(t) &= q\frac{\omega_0}{c}\left[n(\omega_0) - n(\omega_q)\right] \\ &\approx q\frac{\omega_0}{c}\left(-\eta(t)\frac{2\pi\rho e^2}{m\omega_0^2}\right) \\ &= -q\eta(t)\rho r_0\lambda_0 \end{aligned} \tag{2.21}$$

Defining the length $z_\rho \equiv 1/\rho r_0\lambda_0$, we can summarize the four components contributing to Δk:

$$\Delta k_{\text{atomic}} = \frac{q}{z_\rho}\left(\frac{1}{q^2}f_1^0(\omega_q) - f_1^0(\omega_0)\right) \tag{2.22}$$

$$\Delta k_{\text{plasma}} = -\frac{q}{z_\rho}\eta(t) \tag{2.23}$$

$$\Delta k_{\text{Gouy}} = -\frac{q}{z_R}\frac{1}{1 + (z_c/z)^2} \tag{2.24}$$

$$\Delta k_{\text{dipole}} = \frac{2|\alpha_q^j|I_{\text{peak}}}{z_R}\frac{z_c/z_R}{1 + (z_c/z_R)^2} \tag{2.25}$$

Phase matching is achieved by balancing the sum of these terms so that for a gas medium of length L and number density ρ, $\Delta kL \ll 1$. The atomic dispersion and plasma contributions to Δk both scale as $1/z_\rho$ and are proportional to the gas density. The terms due to the Gouy phase (Δk_{Gouy}) and the intensity dependent dipole phase (Δk_{dipole}) are

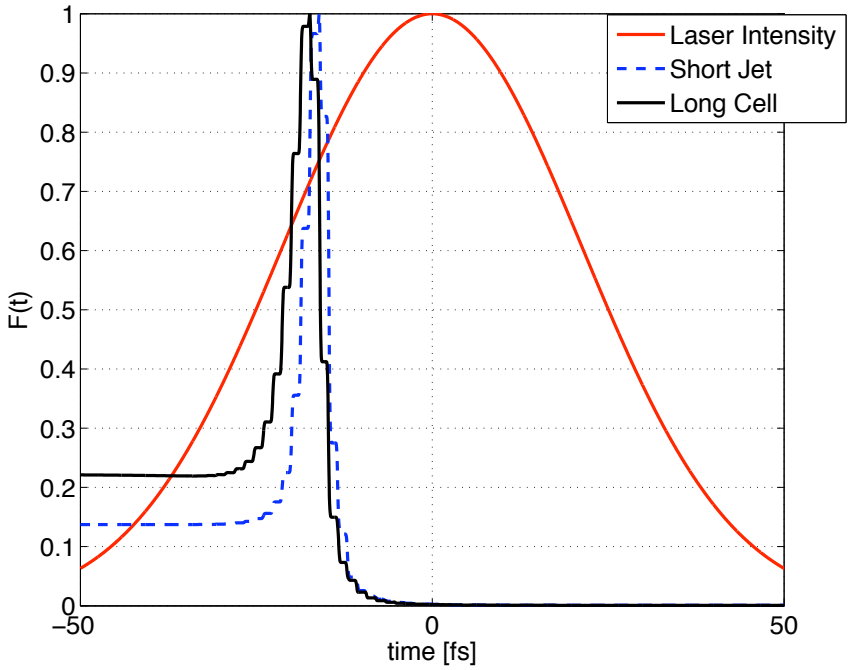

Figure 2.2: **Short Jet vs. Long Cell.** Time dependent phase matching factor F_q for the 19th harmonic of Kr in a 50 fs, 800 nm laser pulse with peak intensity 2×10^{14} W/cm^2. The laser is loosely focused so $z_R = 76$ cm. The dashed blue curve is a for a short gas jet with $L = 0.1$ cm and $\rho = 3.2 \times 10^{18}$ atoms/cm^3 (100 Torr). The solid black curve is for a long gas cell with $L = 10$ cm and $\rho = 3.2 \times 10^{16}$ atoms/cm^3 (1 Torr). The long gas cell has a wider phase matching peak and a higher baseline. Other simulation parameters are $z_c = 20$ cm and $|\alpha_q^j| = 1 \times 10^{-14}$ cm^2/W.

geometric in nature, and scale as $1/z_R$. The sign of Δk_{dipole} depends on the position of the gas cell at $z = z_c$ with respect to the laser focus at $z = 0$. Balcou et. al. [33] have extended this analysis to three dimensions and shown that the balance between the dipole and Gouy terms for on-axis or off-axis phase matching can be adjusted by positioning the focus after ($z_c > 0$) or before the medium ($z_c < 0$), respectively. Good conversion efficiency is attainable in both cases [37, 44].

If the geometric terms due to the Gouy phase (Δk_{Gouy}) and the intensity dependent dipole phase (Δk_{dipole}) are neglected, then satsifying the phase matching condition $\Delta k L \ll 1$ is simply a constraint on the density-length product; a short and dense medium such as that produced by a gas jet can work just as well as a long, dilute medium produced by a gas cell with the same ρL product. The geometric terms, however, can help to balance the medium dispersion, at least early in the pulse when the plasma density is not too high [49].

As the laser focal area is increased, the Rayleigh range increases. For example, a 30 mJ, 50 fs, laser pulse with a Gaussian spatial profile focused to a peak intensity of 2×10^{14}

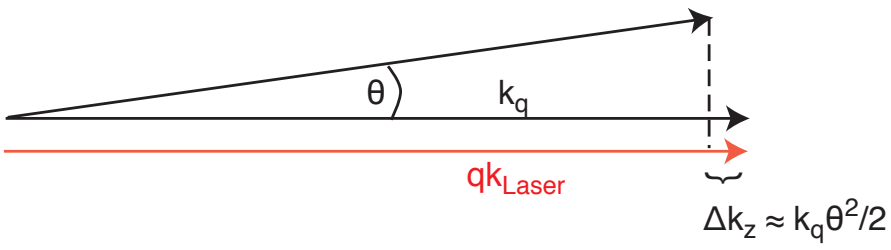

Figure 2.3: **Off Axis Phase Matching.** If phase matching is achieved on axis, off axis rays will have an angle dependent phase mismatch.

W/cm^2 has a Rayleigh range of 76 cm. If a short dense, gas jet is used, the geometric terms are totally irrelevant because $z_\rho \ll z_R$. However, if a long gas cell is used, the Gouy phase and dipole phase can help balance the atomic dispersion. Figure 2.2 compares the time dependent phase matching factor for the 19th harmonic in Kr for a long gas cell and a short gas jet with the same density-length product. The long cell shows a wider phase matched time window and a larger value of F before ionization sets in.

A long cell also produces a lower divergence beam because off-axis phase matching is suppressed. This is illustrated in figure 2.3. If phase matching is achieved on-axis, off axis rays will have a phase mismatch $\Delta k(\theta)_z = k_q(1 - \cos(\theta)) \approx k_q\theta^2/2$. This is the so-called "Cerenkov" Phase Matching Factor [50, 42]. For the condition $\Delta kL \ll \pi$, this implies that the divergence angle θ scales as $1/\sqrt{L}$ [50].

2.2 System Scaling

Far away from the focus ($z \gg z_R$), the laser beam radius goes as

$$w(z) \approx w_0 \frac{z}{z_R} \tag{2.26}$$

For a fixed peak intensity, I_{peak}, the area of the focus must scale linearly with laser pulse energy E. This means that the Rayleigh range also linearly scales with laser pulse energy.

$$z_R \propto w_0^2 \propto E \tag{2.27}$$

The peak fluence F_{peak} a distance l upstream *or* downstream from the focus is

$$F_{\text{peak}}(l) = \frac{2E}{\pi w^2(l)} = \frac{2E}{\pi w_0^2 (l/z_R)^2} \propto \frac{E^2}{l^2} \tag{2.28}$$

All optics have a damage threshold F_{damage}: a laser fluence beyond which they will damage. To avoid damage to optics on either side of the focus, the fluence at the optic must be kept below the damage fluence. This puts a condition on the minimum distance from the focus that optics must be placed, and thus the straight-line length that is needed

in the HHG system. The minimum length $l_{\min}$ of the system then scales as

$$F_{\text{peak}}(l) < \frac{F_{\text{damage}}}{S} \Rightarrow l_{\min} \propto E\sqrt{S} \tag{2.29}$$

where $S = F_{\max}/F_{\text{damage}}$ is a safety factor. We can numerically estimate the minimum distance required on either side of the focus. If a femtosecond pulse damage threshold of ~ 500 mJ/cm^2 is assumed [51] for a dielectric mirror and a safety factor of 2 is employed, equation (2.29) implies a minimum distance of only 16 cm for 1 mJ pulses. For 30 mJ pulses, however, this becomes 4.7 m. In practice, one is not working with perfect Gaussian beams. To account for this one can include an M^2 factor to account for reduced mode quality by substituting $\lambda \rightarrow M^2\lambda$ in equation (2.6) [52]. The divergence angle of the laser after the focus is increased by M^2. Making this substitution and rearranging (2.29)

$$l_{\min} > \frac{2E}{M^2\lambda}\sqrt{\frac{S}{F_{\text{damage}} I_{\text{peak}} \tau_{\text{pulse}}}} \tag{2.30}$$

where τ_{pulse} is the pulse length.

2.3 HHG Beamline

A general overview of the laser system and HHG beamline is shown in figure 2.4. High order harmonics of 807 nm are generated with a repetition rate of 10 Hz by loosely focusing (f = 6 m) 30 mJ, 50 fs laser pulses into a 5 cm gas cell with laser drilled pinholes. The cell can be scanned through the focus and filled with Ar, Kr, or Xe to optimize the desired wavelengths. The harmonic and fundamental beams are allowed to diverge for three meters where they are incident on a superpolished silicon mirror set at the 800 nm Brewster angle (75°). The silicon mirror removes the fundamental and reflects the harmonics towards the "Magnus chamber" where pump/probe experiments are conducted. The Magnus chamber is so named for two reasons: (1) it is large, (2) it was extracted from a junk heap and originally set up by Magnus Bergh. The spectrum of the harmonics can be measured by removing the Si mirror, allowing the beam to enter a Rowland circle monochromator. Absolute photon yields are calculated from the monochromator signal and the signal on a calibrated photodiode placed after the Si mirror. The harmonic yield can also be recorded by measuring the ionization of residual gas with a set of two copper plates (ion plates) between the gas cell and the Si mirror. The ion plate signal can be monitored while running pump/probe experiments to record the shot to shot fluctuations of the HHG yield.

In the Magnus chamber, pump/probe delay is achieved with a split mirror interferometer (SMI). The harmonics are focused into a pulsed molecular beam by two "D-shaped" spherical concave mirrors at normal incidence. One mirror is mounted on a piezoelectric translation stage to produce a delay and the other mirror is mounted on a tip/tilt flexure stage to align the spatial overlap of the two foci. Wavelength selection in each arm of the SMI is achieved by a combination of filters inserted after the silicon mirror and coatings on the two D-shaped mirrors. Photo-ions from the focal region are measured with a time of flight ion mass spectrometer (TOF). The gas cell provides a gas load of ~ 1 Torr-L/s

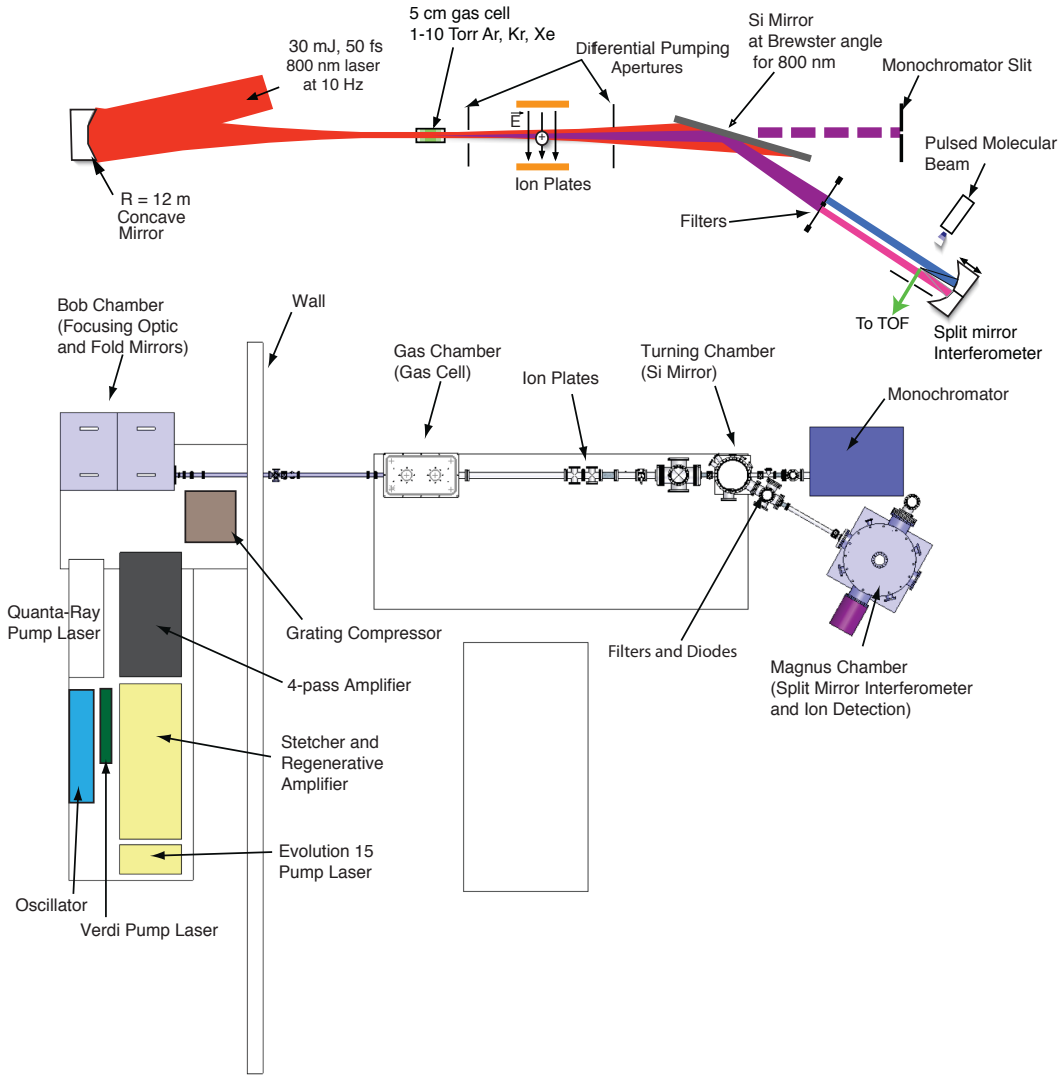

Figure 2.4: **Laser System and HHG Beamline.** A general overview of the apparatus used in this work.

that the vacuum pumping system must handle. The chamber containing the focusing optic and folding mirrors ("Bob Chamber") and the chamber containing the gas cell (Gas Chamber) operate at $\sim 10^{-3}$ Torr. The pressure is reduced downstream by differential pumping through a series of small diameter apertures and short tubes [53]. The pressure at the Si mirror (Turning Chamber) is typically $\sim 5 \times 10^{-7}$ Torr and the Magnus chamber can reach 2×10^{-8} Torr with the pulsed molecular beam off.

More technical details of the HHG beamline are contained in the following sections. The ion TOF and SMI are described in chapter 3.

2.3.1 Laser System

The laser system, based on chirped pulse amplification in titanium doped sapphire [54, 55], produces $\sim$ 30 mJ, 50 fs pulses with a carrier wavelength of 800 nm. The repetition rate of the system is 10 Hz. The system consists of a Kerr-lens modelocked oscillator, an Offner stretcher, a regenerative amplifier operating at 1 kHz, a pulse picker, a four pass amplifier, and a grating compressor.

The oscillator was built from a kit supplied by KMlabs inc. and is similar to that described by Asaki et. al. [56]. Intracavity dispersion is achived through a brewster angle prism pair. The oscillator is pumped with 4.4 W of 532 nm laser light from a frequency doubled CW Nd:YVO_4 laser (Coherent Verdi V6). The oscillator delivers 7 nJ pulses with a repetition rate of $\sim$ 80 MHz to an Offner stretcher [57, 58] containing a 1200 line/mm diffraction grating. The stretcher and regenerative amplifier (Positive Light Legend USP) were supplied by Positive Light incorporated. The group velocity dispersion of the stretcher chirps the oscillator pulses to $\sim$ 200 ps. The regenerative amplifier selects oscillator pules at 1 kHz and amplifies them to 1.2 mJ. The amplifier is pumped with 9 mJ, 532 nm laser pulses at 1 kHz from an intracavity frequency doubled Q-switched Nd:YVO4 laser (Positive Light Evolution 15). Pulses are selected at 10 Hz for further amplification by a pulse picker consisting of a half-wave Pockell's cell (Lasermetrics inc.) and a high bandwidth thin film polarizer. The remaining 990 pules per second are used in an adjacent laboratory for x-ray streak camera characterization [59].

The 10 Hz pulse train is amplified by a home-built 4 pass amplifier shown in figure 2.5. The Ti:Sapphire rod is pumped with $\sim$ 300 mJ, 532 nm laser pulses from a flashlamp pumped frequency doubled Nd:YAG laser (Spectra Physics Quanta-Ray GCR-170). Thermal lensing in the crystal is compensated for with a dichroic spherical convex mirror with 6 m radius of curvature immediately after the Ti:Sapphire crystal. The output power of the amplifier is controlled by varying the pump power and can be increased up to 90 mJ. Normal operation was between 40 and 60 mJ measured at position PM. The beam diameter is expanded to $\sim$ 30 mm by a Gallilean telescope. The negative lens of the telescope is rotated 5° to compensate for the astigmatism of the amplifier. The output pulses of the 4 pass amplifier are compressed with a home-built grating pulse compressor consisting of two 1500 line/mm 120 mm $\times$ 140 mm diffraction gratings and a 4" roof reflector. The efficiency of the compressor was $\sim$ 60%. The pulse length was characterized with a home-built single shot autocorrelator and found to be less than 50 fs FWHM. Many high energy laser systems have the pulse compressor under vacuum to avoid self phase modulation [55] in air and vacuum windows. In this work the compressor was not under vacuum, but the optical path length in air was minimized to $\sim$ 1 m. Only two transmission optics were used in the beam after the compressor: A 0.4 mm crystal quartz 5th order half waveplate used for polarization control and a 2 mm thick fused silica window at the entrance to the Bob chamber. The focusing mirror and most of the optical path length was in the Bob chamber. With the additional losses after the compressor, I estimate that 20-25 mJ was focused for generating harmonics.

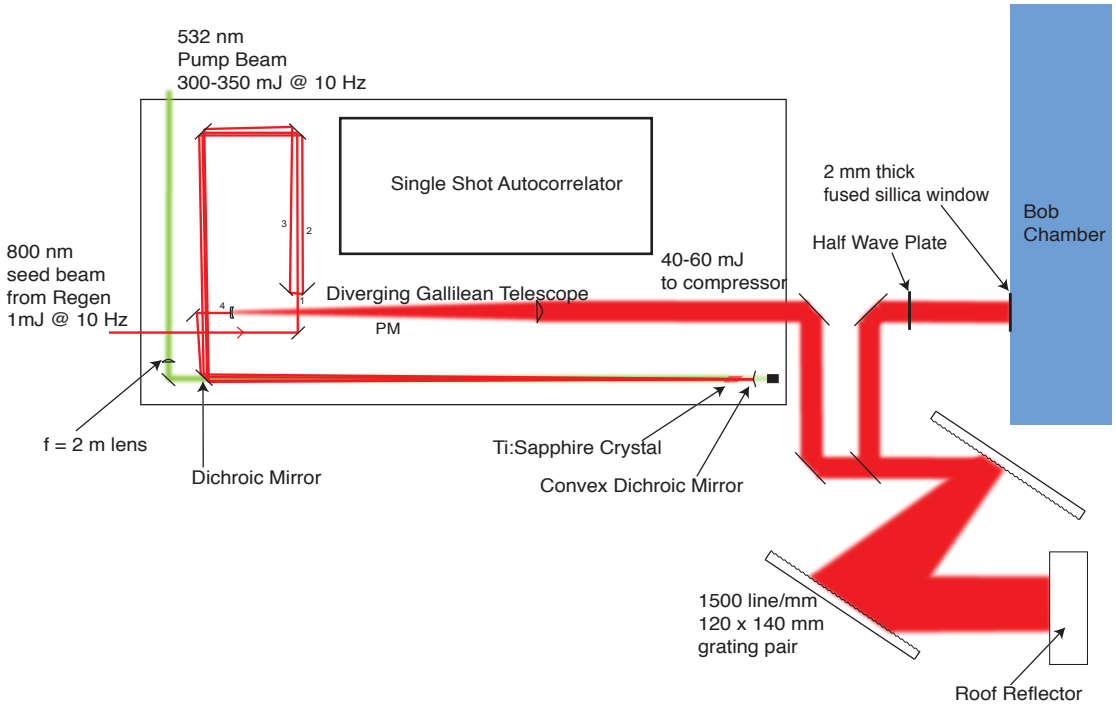

Figure 2.5: **4-pass Amplifier and Compressor.** The optical setup of the four pass amplifier and grating compressor.

2.3.2 Bob Chamber

The Bob chamber was named for Bob Schoenlein who donated it for use in this project. It is pumped out through the pipe that connects it to the gas chamber and contains a large rectangular breadboard for mounting optics. The optical layout of the Bob chamber is shown in figure 2.6. The Bob chamber contains a 12 m radius of curvature (f = 6 m) spherical concave mirror for focusing the laser and 6 folding mirrors. The 1% leakage light from the last 45 degree mirror is used for alignment and characterization of the focus. The Bob chamber flexes significantly when it is evacuated, necessitating in-vacuum alignment. The beam is aligned into the chamber by observing the beam on cross 1 with the "Bob-in" CCD camera. The focusing mirror is tilted with pico-motor actuators (New Focus inc.) to align the beam on cross 2, observed with the "Curve-cam" CCD camera. The last 45 degree steering mirror sits 2.3 m from the front of the gas chamber and is also picomotor controlled to align the laser down the beamline. A third CCD camera sits at an equivalent, but low power, focal point for imaging the focal spot.

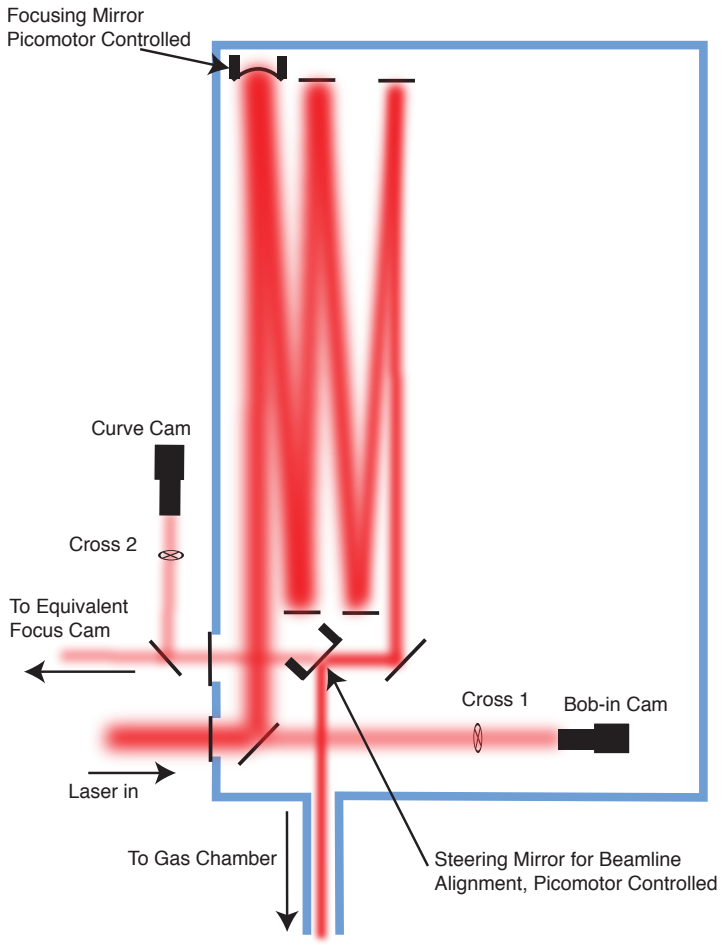

Figure 2.6: **Bob Chamber.** The optical setup of the Bob chamber.

2.3.3 Gas Chamber and Gas Cell

The gas cell is mounted on a translation stage with 50 cm of travel. The translation stage is manually actuated through a rotary feedthrough and can be scanned to either side of the focus. Further adjustment of the relative gas cell/focus position can be achieved by small adjustments to the Galilean telescope in the 4-pass amplifier. The gas cell consists of a 25 mm diameter stainless steel pipe 5 cm in length. Each end of the pipe is sealed by compressing a 50 μm thick, stainless steel disc (shim stock) against an O-ring. Two $\sim$ 1 mm pinholes are drilled in the discs by the laser. The discs must be replaced daily when the laser is realigned, as pointing fluctuations of the laser tend to enlarge the holes.

Gas is introduced in the cell through a swage-lock fitting near the upstream end of the pipe. The gas cell feedline pressure is measured with a capacitance manometer and controlled with an electronically actuated needle valve (MKS inst.). The measurement

point and the gas cell are connected with 1 m of 0.5" diameter flexible tubing. The feedline pressure was operated between 1 and 10 Torr depending on the HHG target gas and the desired wavelengths.

2.3.4 Si Mirror Beamsplitter

The conversion efficiency of HHG is in the range of 10^{-6} to 10^{-5}, so the majority of the laser power emerging from the gas cell is still in the near infrared at 800 nm. To conduct clean VUV pump/probe experiments without contamination from residual laser light, it is necessary to spectrally filter the beam that emerges from the gas cell. This is usually accomplished with a metallic filter. Light below the plasma frequency of the metal is efficiently reflected [60], but XUV light above the plasma frequency is transmitted. However, because of the high XUV atomic absorption cross sections, the filter must be extremely thin, in the range of 0.1-0.2 μm, and the laser damage threshold of these thin metallic filters is on the order of 40 mJ/cm^2 [61]. We can estimate the distance downstream from the focus such a filter would have to sit with equation (2.30). For a 30 mJ, 800 nm laser pulse focused to a peak intensity of 2×10^{14} W/cm^2, a pulse length of 50 fs, $M^2 = 2$, and a safety factor of 2, equation (2.30) gives a minium distance from focus to foil of 8.4 m. This would not fit in the laboratory.

An alternative method for eliminating the 800 nm laser light is through a dichroic beamsplitter [62, 61] at the 800 nm Brewster angle. For a material with a pure real index of refraction n, the Fresnel reflection coefficient is zero for light incident at Brewster's angle and polarized in the plane of incidence (p-polarization) [28], the Brewster angle is given by

$$\theta_B = \tan^{-1}(n) \tag{2.31}$$

For a material with absorption and a finite imaginary component to n, the Brewster condition still provides the minimum reflectivity. Since the harmonics and the fundamental have very different indeces of refraction, a mirror at the Brewster's angle for 800 nm can have a non-zero reflectivity for the harmonics. For glasses with an index of refraction of ~ 1.5, Brewster's angle is around 56°. At this angle of incidence, the XUV reflectivity of dielectric materials is low [11, 39]. For example, the reflection of 40 nm light from an SiO_2 surface at 56° is only 3% [46]. For this reason, XUV optics often operate at grazing incidence. The ideal Brewster angle beamsplitter would then have a large index of refraction in the near infrared, so that the Brewster condition provides a grazing incidence reflection for the XUV light. Other considerations in choosing a material are it's laser damage threshold, chemical stability, and its ability to be polished. Achieving a low surface roughness through polishing is critical for reflectivity at short wavelengths because in order to have a good reflectivity, a mirror must have an rms surface roughness much less than the wavelength.

Silicon has a high index of refraction at the 800 nm wavelength ($n = 3.71 + 0.01i$) [63], corresponding to a Brewster angle of 75°, and high quality silicon surfaces can be fabricated. The femtosecond laser damage threshold of silicon is actually one of the best known numbers in ultrafast science, due to the numerous studies of ultrafast semiconductor melting [64, 65, 66]. At normal incidence it is about 100 mJ/cm^2. From this one can estimate the damage threshold when working at the Brewster angle of 75°. At normal incidence, the

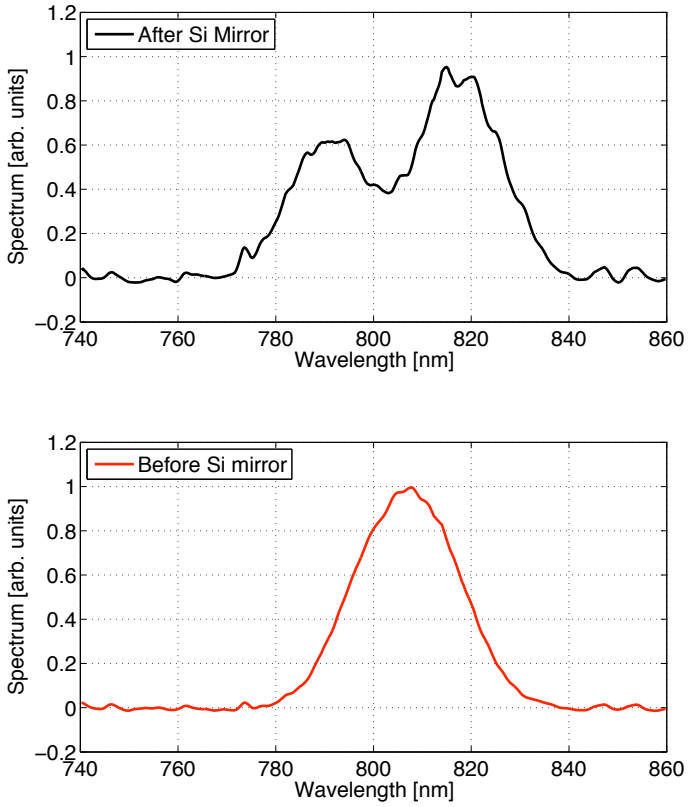

Figure 2.7: **Laser Spectrum After the Si Mirror.** The NIR laser spectrum before and after the Si mirror.

Si surface has a reflectivity of 33%, so that the absorbed fluence at the damage threshold is 67 mJ/cm^2. At Brewster's angle the full fluence of the laser is absorbed, but at grazing angle, the area of the beam is $1/\cos(75°) = 3.86$ larger. These two factors combine to give a laser damage threshold for the Si mirror at Brewster's angle of 260 mJ/cm^2, measured perpendicular to the beam. This is 6 times higher than the thin metallic filter.

Using the Fresnel reflection formulae, the 800 nm reflection of the Si mirror is calculated to be as low as 10^{-5} at the Brewster angle. In practice, the situation is somewhat worse than this due to the finite divergence and spectral bandwidth of the infrared laser light. Figure 2.7 compares the observed IR spectrum before and after the Si mirror, with no gas in the cell. Before the mirror, the spectrum is a Gaussian peaked at 807 nm. The reflected spectrum has a hole in the middle where the IR reflectivity is lowest. Note that both signals are normalized to one so that the relative magnitude of before and after cannot be compared by inspecting the y-axes. I measured the beam power after two Si mirror reflections to be reduced to 1.6×10^{-5} of its original value. This was not limited

by the polarization contrast of the laser because improving the laser polarization contrast with a high quality Glan laser polarizer did not reduce the reflectivity further, indicating a single Si mirror IR reflectivity of $\sim 4 \times 10^{-3}$.

I characterized the XUV reflectivity of the Si mirror at beamline 6.3.2 of the Advanced Light Source (ALS) [67] with XUV light polarized perpendicular to the plane of incidence (s-polarization). Figure 2.8 shows the measured Si mirror reflectivity as a function of photon energy at two points on the mirror surface along with that predicted by the Fresnel equations for a clean Si surface [46]. The reflectivity is decreased from that of a perfect Si surface by the presence of the native oxide SiO_2 and other surface contaminants. The mirror was run for many hours in the HHG beamline before characterization and the the XUV reflectivity is $\sim 25\%$ lower in the center of the mirror, where the beam was present, than the unexposed edge. Figure 2.9 shows a 2D map of the reflectivity of the mirror surface for 42.1 nm light (19th harmonic). The optical reflectivity was found to be uniform over the mirror surface.

The ~ 7 mm size of the degraded region is roughly the same size of the differential pumping aperture 30 cm upstream of the mirror. This indicates that the damage is mainly caused by the NIR laser and not the XUV light, because the XUV light has a much smaller beam size on the mirror (see section 2.4). However, the decreased reflectivity is not caused by an increased surface roughness due to repeated laser induced melting and recrystalization of the surface, as this would show a strong wavelength dependence through the Debye Waller factor [37]. Instead, the reflectivity decrease is roughly independent of wavelength. Further analysis is needed to determine the exact cause of the decreased reflectivity, but a likely suspect is increased oxide growth or carbon contamination. The Si mirror's vacuum chamber was pumped by an oil lubricated turbo pump and while operating, and the pressure over the Si mirror was only 5×10^{-7} Torr. The time scale for the reflectivity degradation was not determined.

The Si mirror reflectivity measurements were made with s-polarized light at beamline 6.3.2, but the mirror reflects p-polarized XUV light in the HHG beamline. It was not possible to rotate the XUV polarization at the ALS's beamline 6.3.2 without rotating the reflectometer endstation or the ALS itself. Neither was practical. A direct inversion of the Fresnel equations for an "effective" index of refraction for the surface is not feasible because the imaginary part of the index is not negligible and the interference between reflections between the Si substrate and oxide or contamination layers may be important. For determining absolute harmonic yields before the mirror, the p-polarization reflectivity was modeled as being that of a smooth Si surface with a 3 nm SiO_2 oxide layer. This model of the mirror gave reasonable agreement with the s-polarization reflectivity data.

2.3.5 Monochromator

The scanning monochromator (Acton Research Corp.) used to measure the HHG spectra consists of a spherical concave grating with $R = 1.5$ m radius of curvature and entrance and exit slits placed on the Rowland circle [11]. The grating has a groove density of 300 lines/mm and is blazed for optimum diffraction of 30 nm light at an angle of incidence of 84°. Photons passing through the exit slit illuminate the face of a lucite light guide coated with a sodium salicylate powder. The 420 nm fluorescence photons from the salicylate are

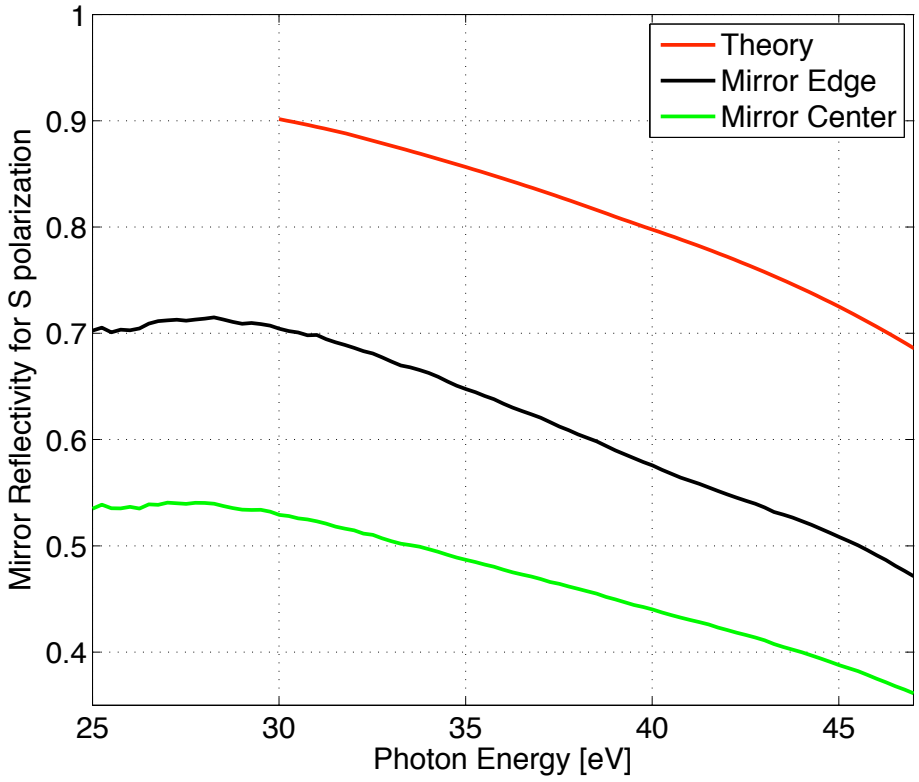

Figure 2.8: **Si Mirror XUV reflectivity.** The XUV reflectivity of the Si mirror for s-polarized light as a function of photon energy. The reflectivity is always less than theory predicts for a perfect Si surface due to oxide layers and contamination of the surface.

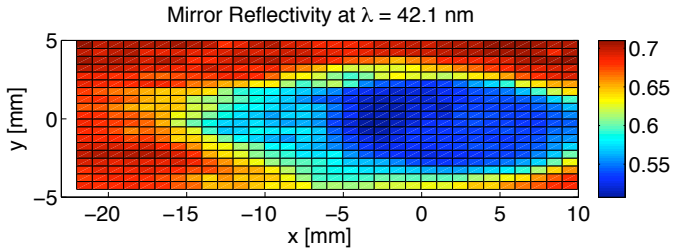

Figure 2.9: **Si Mirror Degradation.** The Reflectivity of the Si mirror for the 19th harmonic as a function of position on the mirror. The $\sim$ 7 mm diameter spot of reduced reflectivity is created by the NIR light.

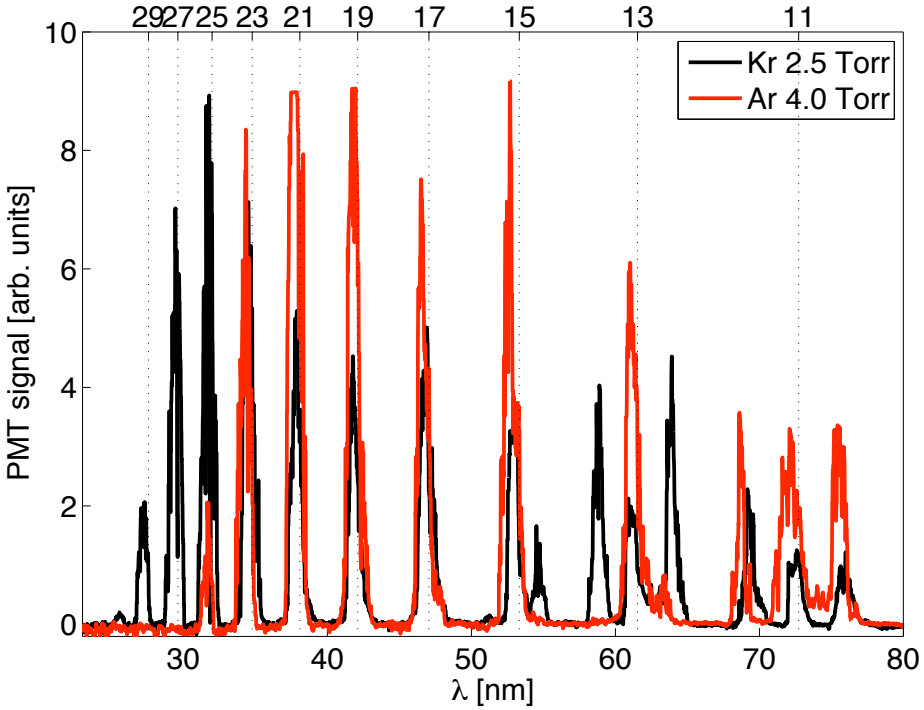

Figure 2.10: **Ar and Kr HHG comparison.** A comparison of harmonics generated in Argon and Krypton gasses. The pressure listed is the cell feedline pressure. Harmonic orders are labelled on the top axis. The second diffraction order of the grating is visible in the peaks that do not line up with the harmonic orders.

detected with a photomultiplier tube (PMT) at the other end of the lucite light guide. Sodium salicylate was chosen because its quantum efficiency is independent of wavelength between 100 and 10 nm [11]. The exit slit and detector assembly is mounted on a precision machined curved way along the Rowland circle. An HHG spectrum is recorded by scanning the exit slit along the Rowland circle and recording the PMT signal as a function of slit position. The grating equation relates wavelength and slit position:

$$m\lambda = d(\sin(\alpha) - \sin(\beta)) \tag{2.32}$$

where m is the diffraction order, d is the groove spacing, α is the angle of incidence of the light measured with respect to the grating normal, and β is the outgoing angle of the diffracted light. The outgoing angle is related to the distance x between the exit slit and the grating through

$$\beta = \cos^{-1}(x/R) \tag{2.33}$$

The grating groove spacing and radius of curvature were taken as knowns from the manufacturer's specification. Calibration of the angle of incidence and the x-scale was achieved by recording the zeroth, first, and second diffraction orders in a single scan and adjusting

α and the offset to the x-scale so that equation (2.32) correctly predicts the x position of the different orders. The grating diffraction efficiency was characterized at BL 6.3.2 of the ALS.

2.4 HHG Spectra, Absolute Yields, and Spatial Profiles

HHG spectra from Ar and Kr gas taken with the same laser conditions and gas cell position are shown in figure 2.10. The gas cell pressure was tuned in each case to maximize the total signal on an aluminum coated photodiode placed after the Si mirror (AXUV100-Al, International Radiation Detectors inc.). The photodiode records signal from all photons above 15 eV ($\lambda < 82$ nm). Both spectra exhibit a cutoff, but the Kr spectra occurs at lower photon energy. This is due to the ionization gate illustrated in figure 2.1. The ionization potentials of Ar and Kr are 15.8 eV and 14.0 eV, respectively. Since the tunnel ionization rate is exponentially sensitive to the ionization potential [41], the Kr atoms ionize earlier in the pulse, and the peak in the phase matching factor $F(t)$ is shifted to earlier times and lower laser intensity. The cutoff energy, given by equation (1.19) is correspondingly reduced.

The absorption limited behavior illustrated in figure 1.9 was observed in both the Ar and Kr HHG cases by varying the gas cell pressure. The optical thickness, $\rho\sigma L = L/L_{\mathrm{abs}}$, of the medium can be varied by changing the gas cell length L, but it can also be varied by changing the gas density ρ. Figure 2.11 shows HHG spectra from Ar at 3.0 and 4.0 Torr feedline pressures along with the photo-absorption cross section or Ar. The lower orders (11-19) have a higher absorption cross section, and thus a shorter absorption length and are generated with a higher optical thickness L/L_{abs}. Increasing the density and L/L_{abs} does not change their yield as they have already reached the absorption limit. The higher orders (21-29) have a smaller absorption cross section and the yield can still be increased by increasing the density. Increasing the density further will start to degrade the phase matching conditions for all the orders through increased plasma density.

The absolute harmonic yields were determined by using the monochromator scans to determine the relative intensities of the harmonics and using the aluminum coated diode to determine the appropriate scale factor. The photodiode was operated without reverse bias and the integrated charge produced in the photodiode was measured by integrating the diode pulse on a digital oscilloscope with 50 Ω termination. No significant changes in the integrated signal were found upon applying a reverse bias voltage up to the photodiode's reverse breakdown voltage of 10 V. The quantum efficiency (electrons/photon) of the photodiode as a function of harmonic order, QE(q), was taken from the manufacturer's data sheets [68]. The integrated charge produced by the diode is given by

$$Q = e \sum_q N_q R_{\mathrm{Si}}(q) \mathrm{QE}(q) \tag{2.34}$$

where N_q is the number of photons in harmonic order q. The reflectivity of the Si mirror, R_{Si}, must be taken into account because the diode sits after the Si mirror to avoid damage. The monochromator sees the direct harmonics beam. With the assumption that the different harmonic orders overfill the monochromator input slit by the same factor, the peak heights

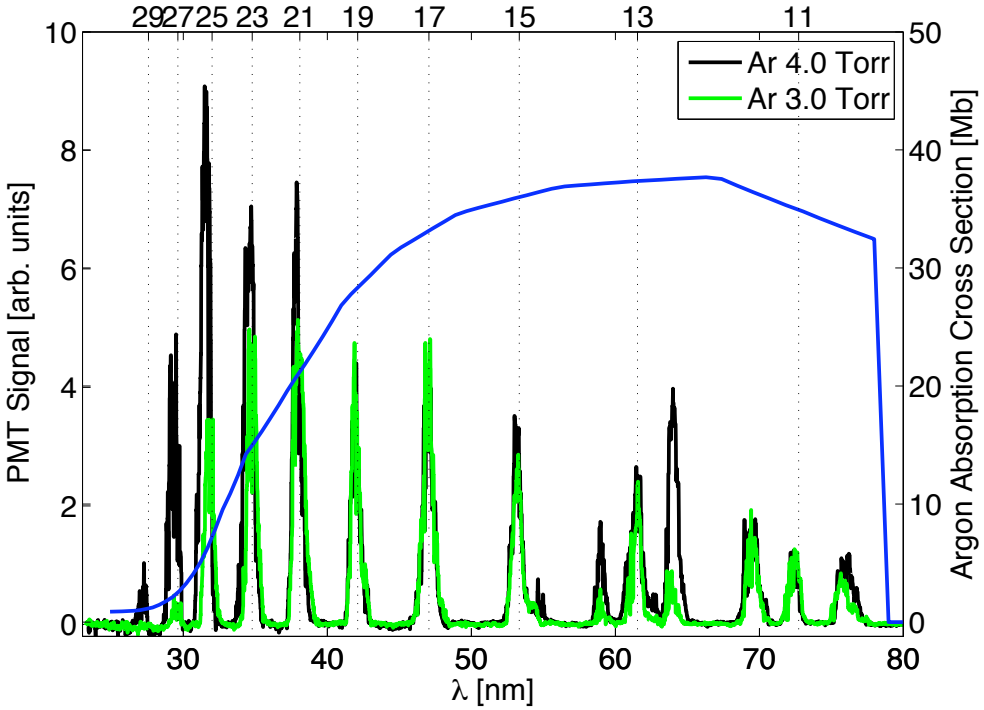

Figure 2.11: **Absorption Limited HHG.** HHG spectra with gas cell feedline pressures of 4.0 Torr (black curve) and 3.0 Torr (green Torr). The photo-absorption cross section of Ar is shown in blue (right scale). Orders 11-19 are absorption limited and show no change as the pressure is increased. Orders 21 through 29 have a lower absorption cross section and can still be enhanced by increasing the pressure from 3 to 4 Torr. Harmonic orders are labelled on the top axis. The second diffraction order of the grating is visible in the peaks that do not line up with the harmonic orders.

recorded in the spectrum S_q, are related to the absolute photon yields N_q through

$$S_q = C\mathrm{GE}(q)N_q \tag{2.35}$$

where $\mathrm{GE}(q)$ is the harmonic dependent grating diffraction efficiency and C is a constant scale factor. We can solve for the scale factor by rearranging equation (2.35) for N_q and inserting it into equation (2.34). The result is

$$C = \frac{e}{Q}\sum_q \frac{S_q}{\mathrm{GE}(q)} R_{\mathrm{Si}}(q)\mathrm{QE}(q) \tag{2.36}$$

with all the parameters on the RHS of equation (2.36) characterized, the sum can be evaluated and the scale factor determined. The scale factor is then reinserted into equation (2.35) to determine the harmonic yields N_q. This technique for determining the absolute

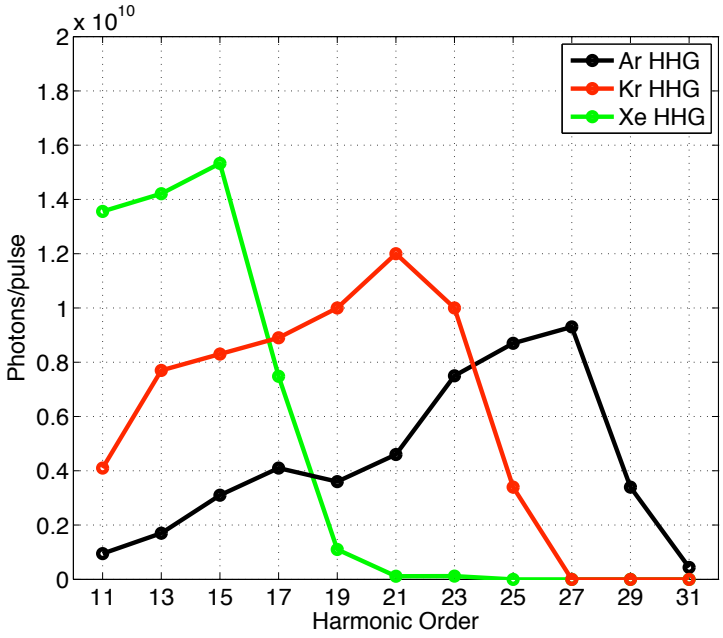

Figure 2.12: **Optimized HHG yields.** The highest harmonic yields at the gas cell exit obtained in this work.

q	Ar 4.0 Torr		Kr 2.5 Torr		Xe 2.4 Torr	
	E [nJ]	CE	E [nJ]	CE	E [nJ]	CE
11	2.6	1×10^{-7}	11	4.4×10^{-7}	38	1.5×10^{-6}
13	5.4	2×10^{-7}	25	1.0×10^{-6}	45	1.8×10^{-6}
15	12	4.8×10^{-7}	31	1.2×10^{-6}	56	2.3×10^{-6}
17	17	6.8×10^{-7}	38	1.5×10^{-6}	31	1.2×10^{-6}
19	17	6.8×10^{-7}	47	1.8×10^{-6}	5	2×10^{-7}
21	24	9.6×10^{-7}	63	2.5×10^{-6}	0.5	2×10^{-8}
23	43	1.7×10^{-6}	57	2.3×10^{-6}	0.6	2×10^{-8}
25	54	2.2×10^{-6}	21	8.4×10^{-7}	-	-
27	62	2.5×10^{-6}	-	-	-	-
29	25	1.0×10^{-6}	-	-	-	-
31	3.4	1.4×10^{-6}	-	-	-	-

Table 2.2: **HHG yields**. The calculated energy of the harmonics at the exit of the gas cell in nanoJoules and conversion efficiencies ($E_{\text{harmonic}}/E_{\text{Laser}}$) for harmonics 11-31.

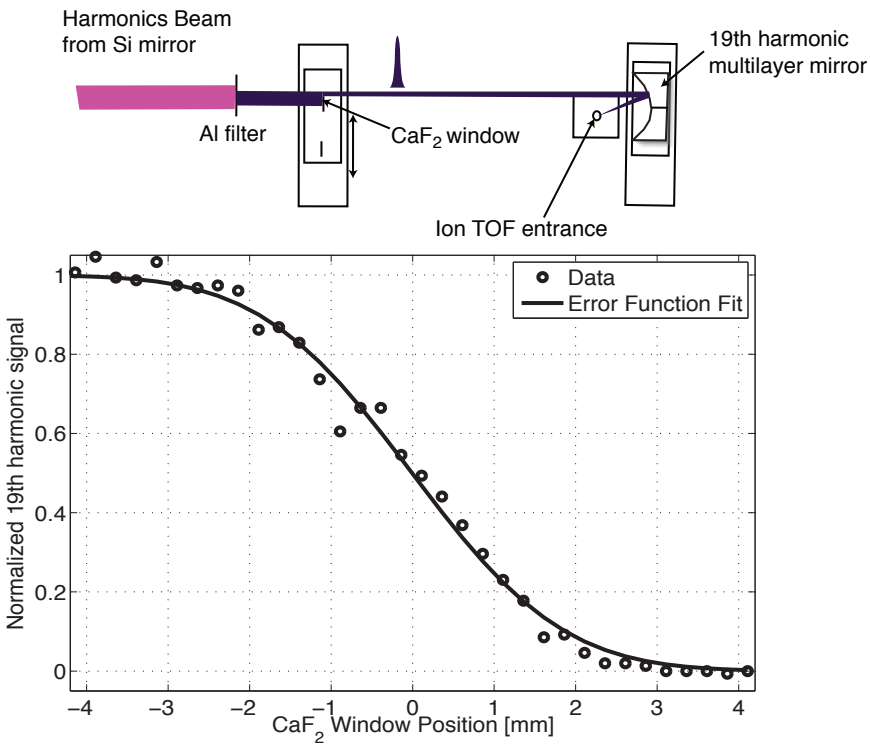

Figure 2.13: **19th Harmonic Knife Edge Scan.** The ion yield from the focused 19th harmonic is recorded as a CaF_2 window is inserted into the beam. The CaF_2 has zero transmission for the 19th harmonic and serves as a knife edge. The data is fit with a error function. The FWHM of the corresponding Gaussian is 3.5 ± 0.1 mm.

yields was cross checked using a He ionization chamber [11] instead of the diode to determine the scale factor for the spectrum. The two methods agreed within 20%.

The best results obtained with with Ar, Kr, and Xe target gasses are shown in figure 2.12, and tabulated in table 2.2. Xe has an I_p of only 12.2 eV and shows an even lower cutoff photon energy than Ar and Kr. The uncertainty of the absolute yields is estimated to be $\sim 50\%$. The conversion efficiency in table 2.2 is calculated assuming 25 mJ of laser energy at the gas cell. The peak intensity at focus was calculated to be 6×10^{14} W/cm^2 from the measured spatial profile and the laser pulse energy and pulse length. In all cases the best conversion efficiency was found for gas cell positions upstream of the focus by 30 to 50 cm. The peak intensity at the gas cell was estimated to be $\sim 1 \times 10^{14}$ W/cm^2 for Ar and Kr HHG and less than this for Xe.

The far field divergence of the 19th harmonic from Kr was measured at the Magnus chamber with the arrangement shown in figure 2.13. All orders lower than 11 are blocked by a 0.16 μm thick Al filter after the Si mirror. The 19th harmonic is selected and focused over the entrance of the ion time of flight spectrometer (Ion TOF) with a Mg/Si:C multilayer mirror. The ion signal is recorded as a CaF_2 window is scanned into the beam. The CaF_2

window has zero transmission for the 19th harmonic and serves as a knife edge. The ion signal is shown in figure 2.13. For a Gaussian beam profile with standard deviation σ_x, the percentage of the beam that passes around the knife edge at position x_e with respect to the center of the beam is

$$\begin{aligned} S(x_e) &= \frac{1}{\sqrt{2\pi}\sigma_x}\int_{x_e}^{\infty} dx e^{-x^2/2\sigma_x^2} \\ &= \frac{1}{2}\left[1-\mathrm{erf}\left(\frac{x_e}{\sigma_x\sqrt{2}}\right)\right] \end{aligned} \tag{2.37}$$

When I fit the knife edge scan signal with equation (2.37), I find a FWHM for the underlying 19th harmonic spatial profile of 3.5 ± 0.1 mm. The CaF_2 window was 4.7 m away from the gas cell position indicating a FWHM divergence angle of 3.5 mm/4.7 m = 0.75 mrad.

2.5 The Fifth Harmonic

The fifth harmonic of 800 nm has a photon energy of 7.75 eV. This energy is ideal for exciting small molecules, which typically have their first absorption band near $\sim \frac{3}{4}I_p$. The lower orders (e.g. 3, 5, 7) of the HHG spectrum can be quite intense. This is because they are not limited by absorption and because they can be generated at the lower intensities of the leading edge of the pulse, before the ionization gate. It also easier to achieve phase matching for the lower orders because of q-scaling of Δk discussed in section 1.3.2.

I measured the fifth harmonic yield of the HHG source with an uncoated silicon photodiode (AXUV100 International Radiation Detectors inc.) behind a bandpass filter designed for 160 nm (Acton Research Corp 160-N). The bandpass filter consists of an aluminum interference coating on a MgF_2 substrate and has a transmission of 17% for the fifth harmonic and less than 10^{-4} for the fundamental and all other orders. Figure 2.14 shows the fifth harmonic power as a function of gas cell pressure for Ar, Kr, and Xe with the gas cell position optimized for the higher orders. Over 150 nJ can be generated under conditions suitable for generating the higher orders. If the gas cell feedline pressure is increased, the fifth harmonic yield can be further increased at the expense of the higher orders. The fifth harmonic yield can also be increased by moving the gas cell further from the focus and working at lower intensity and larger laser spot area at the gas cell.

The fifth harmonic spectra from Ar and Xe target gasses is shown in figure 2.15. The fifth harmonic spectral bandwidth is broad enough to support ~ 13 fs pulses according to equation (1.14) The spectrum from Xe exhibits more structure and a high energy side-band. As the Ar pressure is increased, the spectrum becomes broader and shifts to shorter wavelengths. This can be understood in terms of plasma blue-shifting of the laser pulse in the gas medium [69, 70]. In addition to influencing phase matching (see section 2.1), the rapidly changing index of refraction due to generated free electrons leads to self phase modulation of the drive laser [22]. This will broaden the drive laser pulse spectrum and shift it to shorter wavelengths [69]. The effect is stronger in a higher density medium where there are more electrons.

This phenomena can also be directly observed in the drive laser spectrum after the gas cell and is shown in figure 2.16. I recorded the spectra in figure 2.16 by rotating the

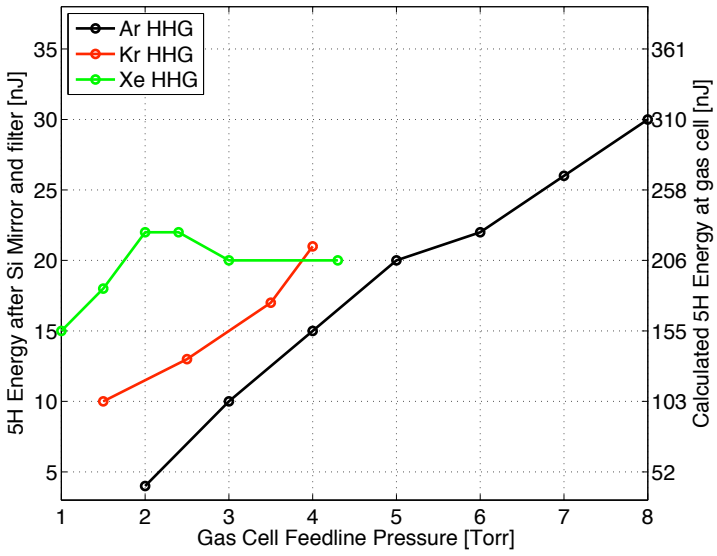

Figure 2.14: **Fifth Harmonic Yield.** The left scale shows fifth harmonic yield measured in the Magnus chamber after the Si mirror and the fifth harmonic bandpass filter. The right scale shows the calculated yield after the gas cell assuming a filter transmission of 17% and a Si mirror reflectivity of 57%.

drive laser polarization 90° so that the Si mirror reflects the drive laser and performing the measurement after the Magnus chamber. A clear shift to shorter wavelengths is observed as the gas cell pressure is increased. The overall amplitude is also reduced because of plasma defocusing in the gas cell [71]. The divergence of the laser after the gas cell is higher at higher plasma densities and the percentage of the beam making it through the differential pumping apertures is reduced.

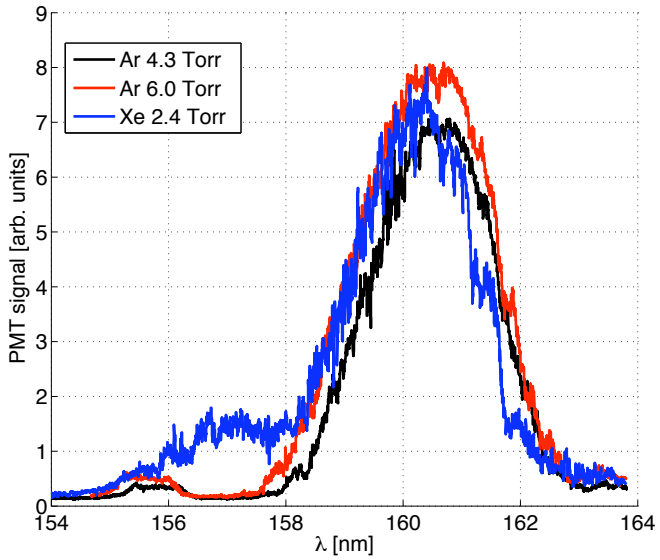

Figure 2.15: **Fifth Harmonic Spectrum.** As the gas cell feedline pressure is increased, the fifth harmonic spectrum is broadened and shifted to shorter wavelengths. The Xe spectrum is also blue-shifted and exhibits more structure.

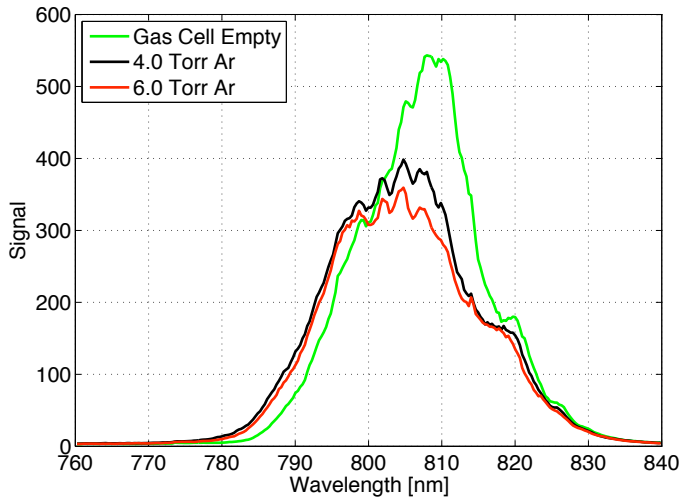

Figure 2.16: **Plasma Blueshifting.** As the Ar pressure is increased, the IR spectrum after the cell exhibits a plasma blueshift. Spectra are recorded after the Si mirror by rotating the drive laser polarization 90° so that the Si mirror reflects the IR. The integrated signal is also reduced at higher intensity due to plasma defocusing of the laser in the gas cell.

Chapter 3

Split Mirror Interferometer

I don't do quagmires.

-Secretary of Defense Donald Rumsfeld

Due to the strong absorption of all materials at XUV wavelengths, no efficient beam splitting optics exist in the extreme ultraviolet. Even if they did, the loss of the routing mirrors necessary to produce a conventional pump/probe interferometer would not be tolerable. Instead, the harmonics are combined with a variable delay at focus with a split mirror interferometer (SMI) [72, 73]. The SMI assembly is shown in figure 3.1. The harmonics are combined at the common focus of the two "D-shaped" spherical concave mirrors. Both mirrors have a 20 cm radius of curvature (f = 10 cm). The SMI focus intersects a pulsed molecular beam described in more detail in section 3.1.

The left mirror in figure 3.1 is coated to reflect XUV light and defines the "high order arm" of the interferometer (HOA). The right mirror in figure 3.1 is coated to reflect the fifth harmonic and defines the "low order arm" of the interferometer (LOA). The HOA mirror is mounted on a piezo-electric translation stage and can be moved with high resolution parallel to the input beam direction. The position of the HOA mirror controls the relative arrival time ("delay") at focus of pulses from the LOA and HOA mirrors. The pitch and yaw motions of the LOA mirror are motorized to allow alignment of the spatial overlap of the two foci while under vacuum. Pitch/yaw control is achieved with the following mechanism. The LOA mirror is mounted on a precision machined flexure which is actuated from behind with stainless steel wobble pins. The wobble pins are in turn moved by picomotor actuators at the ends of 4:1 moment arms. Feedback on the mirror pitch and yaw is provided by linear variable differential transducers (LVDTs) which inductively detect the motion of ferromagnetic rods mounted on the moment arms. The LVDT electronics are hermetically sealed for vacuum compatibility. The angular resolution of this assembly is 3 μrad, corresponding to a 0.3 μm motion of the LOA focus in the focal plane.

Mirror mounting to the SMI is accomplished kinematically, so that mirrors can be changed easily. The mirrors are glued to bases made of magnetic stainless steel with a low outgassing epoxy. A kinematic mate is made between three grooves machined in the back

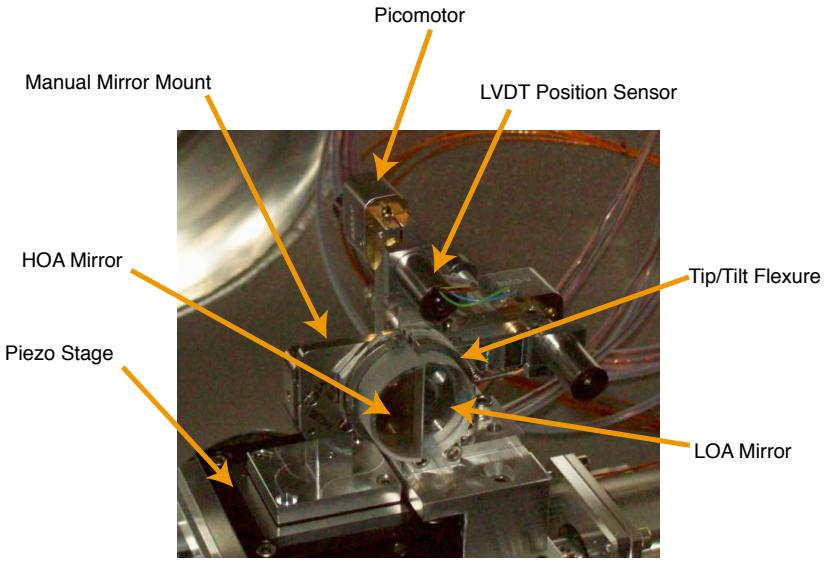

Figure 3.1: **Split Mirror Assembly.** The circle formed by the two D-shaped mirrors is 1" in diameter.

of a magnetic base and three ruby balls on the SMI mirror mounts. The mirrors are held in place by magnets in the SMI mirror mounts.

The many wavelengths produced in HHG are both a blessing and a curse for pump/probe measurements. A blessing because of the broad array of wavelengths available for pump and probe. A curse because there are many wavelengths in each arm of the SMI whether you want them there or not. In general, it is not possible to attain sufficient wavelength specificity in each arm of the SMI using the mirror coatings alone. For example, an XUV multilayer coating designed to reflect the 19th harmonic will contain metals, and will have a non-zero reflectivity for the fundamental and lower harmonic orders. If the harmonics beam is directly reflected off the mirror, the 19th harmonic probe light is then "contaminated" with longer wavelength radiation, and the ion signals are difficult to interpret. The residual fundamental and third harmonic light reflected off the Si mirror are still strong enough to produce ions through multiphoton absorption and can be particularly problematic.

Better wavelength specificity is achieved by inserting filters between the Si mirror and the SMI. A mirror/filter scheme I used to perform clean 5th harmonic pump/19th harmonic probe experiments is shown in figure 3.2. In the high order arm, a 0.16 μm thick aluminum foil blocks all harmonic orders lower than the 11th and residual fundamental light. The 19th harmonic is then selected from the remaining orders by the Mg/Si:C multilayer mirror [74]. In the low order arm, a 230 μm thick CaF_2 window blocks all orders higher than the 5th. The fifth harmonic is reflected by a dichroic mirror with high ($> 90\%$) reflectivity at 160 nm and low reflectivity for the third harmonic and fundamental. Further discrimination between the fifth harmonic and residual 3rd/fundamental is provided by the

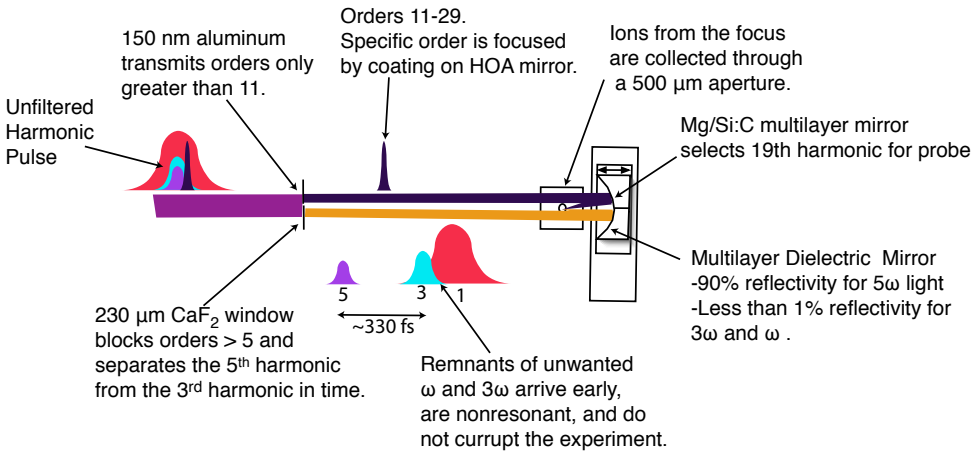

Figure 3.2: **5th Harmonic Pump/19th Harmonic Probe Configuration.**

group velocity dispersion of the CaF_2 window (see section 3.2). The fifth harmonic has a much slower group velocity in the window, and is delayed by more than 300 fs with respect to the third harmonic and fundamental. Any unwanted multiphoton excitation from remnant 3rd/fundamental light is then temporally separated from effects due to the fifth harmonic. In practice, for the target molecules used in this work, the 3rd/fundamental reflectivity of the dichroic mirror was low enough that multiphoton excitation from the 3rd/fundamental was sufficiently suppressed. However, the 300 fs temporal separation ensured that multiphoton excitation pathways involving the 5th harmonic and 3rd harmonic or 5th harmonic and fundamental were not present.

The entire SMI assembly and the upstream filters are mounted on translation stages with motion axes perpendicular to the beam. When the mirrors and filters are moved side to side, the percentage of the beam illuminating each half of the SMI changes. The power in each arm of the interferometer can then be controlled. Upstream of the filters, an edge can be inserted to block either half of the beam and observe the signal from each arm of the SMI separately.

3.1 Time of Flight Mass Spectrometer and Ion Detection

The signal measured in all the VUV pump/probe measurements described in this thesis is photoion yield. The photoions were collected and measured with the time of flight mass spectrometer illustrated in figure 3.3. Ion fragments with different mass to charge ratio m/q traverse the flight tube to the detector with flight time approximately $\propto \sqrt{m/q}$. The spectrometer is run with a strong 3 kV/cm extraction field in a decidedly non-Wiley-MacLauren configuration. In addition to mass and charge, an ion fragment's time of flight (TOF) depends sensitively on in its birth height above the bottom extraction plate. This allows for discrimination between ions from the unfocused XUV beam passing through the extraction region and the focused light reflected from the SMI. Ions produced from the

back-focused beam appear as sharp peaks in the TOF spectrum, whereas ions from the unfocused incident beam appear as a broad background reflecting the incident beam profile in the vertical direction.

Further focus to background discrimination is achieved by extracting ions from the SMI focus through a 500 μm pinhole in the bottom plate of the extraction region. The extraction assembly (circled in figure 3.3) can be moved in three dimensions via a vacuum manipulator feedthrough mounted on the lid of the Magnus chamber, allowing precise positioning of the extraction pinhole under the SMI foci.

Most gas targets were introduced at focus with a supersonic pulsed molecular beam source consisting of a piezo-electric valve behind a conical skimmer [75]. The molecular beam traveled between the extraction plates in a direction orthogonal to the plane of figure 3.3. Calibration of the time resolution of the pump/probe experiments was obtained by observing the ultrafast dissociation of H_2O molecules (see chapter 4). To introduce high densities of H_2O molecules at focus, a solenoid valve was mounted on the extraction assembly and backed with 1-3 Torr of water vapor (see figure 3.3). This valve was used for H_2O because the vapor pressure of water is only 18 Torr at room temperature. The piezo valve/skimmer arrangement used for C_2H_4 and O_2 gasses was $\sim$ 15 cm from the focus and operated with 1-10 psi backing pressure above atmosphere (800-1300 Torr absolute). The piezo valve/skimmer arrangement could not produce high enough H_2O densities at focus with only 18 Torr backing pressure. The solenoid valve was located only 5 mm away from the focus produced sufficient H_2O densities at focus.

3.1.1 Fragment Kinetic Energy Dependent Extraction Efficiency

When molecules or molecular ions dissociate along a repulsive potential energy surface, the fragments have non-zero kinetic energy. This fragment kinetic energy can be in the range of 0 to $\sim$ 5 eV, depending on the reaction, excitation energy, etc. Ions emerging from SMI focus with kinetic energy T at angle θ will not proceed in a straight line towards the extraction pinhole, but will instead follow a parabolic trajectory governed by Newton's equations of motion. Some example trajectories are illustrated in figure 3.4.

While the extraction pinhole prevents many undesired ions from outside the SMI overlap volume from entering the TOF mass spectrometer, one can also see from figure 3.4 that it has a finite angular acceptance for the desired ions born in the SMI overlap volume with kinetic energy. In what follows, I will estimate the collection efficiency as a function of the spectrometer for ions born from a point a height y_0 above the center of the extraction pinhole. The trajectory $y(r)$ for an ion originating from an initial height y_0 above the bottom plate with initial kinetic energy T and angle to vertical θ is:

$$y(r,\theta) = y_0 - \frac{qE}{4T\sin^2\theta}r^2 - \cot(\theta)r \tag{3.1}$$

where E is the electric field between the extraction plates, r is the distance from the center of the pinhole, and q is the charge of the ion. Let's define the dimensionless quantity

$$\alpha \equiv \frac{T}{qEy_0} \tag{3.2}$$

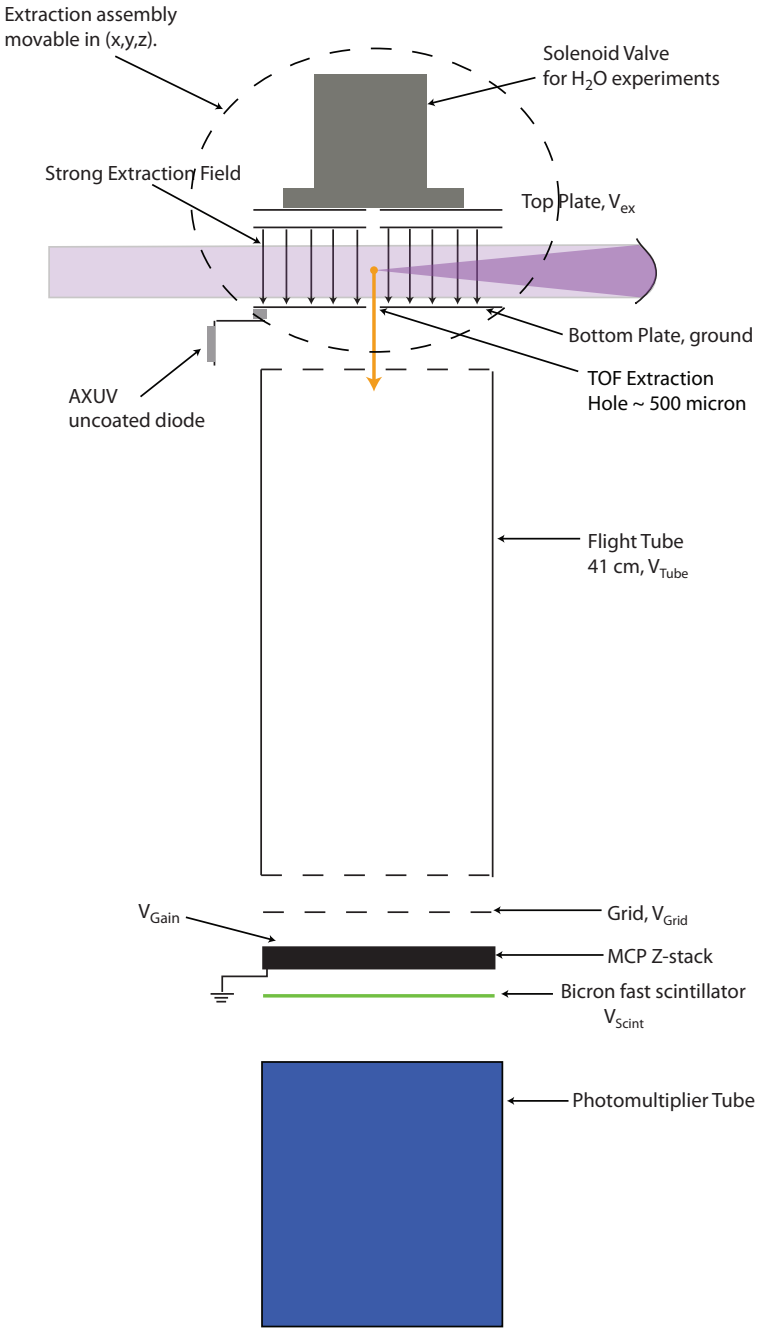

Figure 3.3: **Mass Spectrometer.** Time of Flight mass spectrometer and extraction assembly used for photoion detection.

α is the ratio of the initial kinetic energy of the ion to the kinetic energy gained in the extraction field. The radius r_f at which the ion reaches the plane of the bottom extraction plate is found by setting $y = 0$ in equation (3.1). After some rearrangement,

$$r_f = 2y_0\sqrt{\alpha}\sin\theta\left[\sqrt{1+\alpha\cos^2\theta} - \sqrt{\alpha}\cos\theta\right] \tag{3.3}$$

The TOF mass spectrometer was typically run under conditions such that $qEy_0 \approx$ 800-1000 V, so that $\alpha \ll 1$. We can then approximate

$$r_f \approx 2y_0\sqrt{\alpha}\sin\theta \tag{3.4}$$

With a hole radius of d, equation (3.4) thus defines a critical angle $\theta_c(\alpha)$ beyond which ions will not be collected.

$$\theta_c(\alpha) = \sin^{-1}\left(\frac{d}{4y_0\sqrt{\alpha}}\right) \tag{3.5}$$

Within the approximation of equation (3.4), ions traveling at slight downward angle θ toward the bottom plate have the same final radius r_f as ions traveling at slight upward angle $\pi - \theta$. This is also seen to be very nearly the case in the two (exact) rightward trajectories in figure 3.4. Neglecting integration over the focal volume, the collection efficiency for molecules emitted from the focus with an angular distribution $P_T(\theta, \phi)$ is:

$$CE(T) = 2\int_0^{2\pi} d\phi \int_0^{\theta_c(T)} d\theta \sin(\theta) P_T(\theta, \phi) \tag{3.6}$$

For an isotropic distribution ($P_T(\theta, \phi) = 1/4\pi$), the energy dependent collection efficiency is :

$$CE(T) = 1 - \cos(\theta_c(T)) = 1 - \sqrt{1 - \frac{d^2}{16y_0^2\alpha}} \tag{3.7}$$

This function is depicted in figure 3.5.

3.1.2 Ion Detection

The ion detector is sketched at the bottom of figure 3.3 and works in two stages. In a first stage, ions hit a three plate micro-channel plate z-stack biased at between 1900 and 2400 V (V_{Gain} = -1900 to -2400 V). The z-stack acts as an electron multiplier, creating a plume of electrons at the exit of the stack for each ion hit. These electrons are then accelerated to a fast scintillator where the signal is converted to visible light at $\sim$ 400 nm. This light is then subsequently detected by a fast photomultiplier tube (PMT). The scintillator/PMT setup acts as an optical isolator and allows the voltages of the spectrometer or channel plates to be pulsed without introducing electrical pickup noise in the signal.

At least one ion producing signal on the photomultiplier tube constitutes an "event". Events are recorded with a threshold discriminator and a time to digital converter (LeCroy 3377). The PMT signal level at particular TOF corresponding to a particular ion fragment (m/q) signal can be divided into two regimes: (1) A "counting regime" in which the mean number of ions/shot μ producing signal on the detector is small, and the event

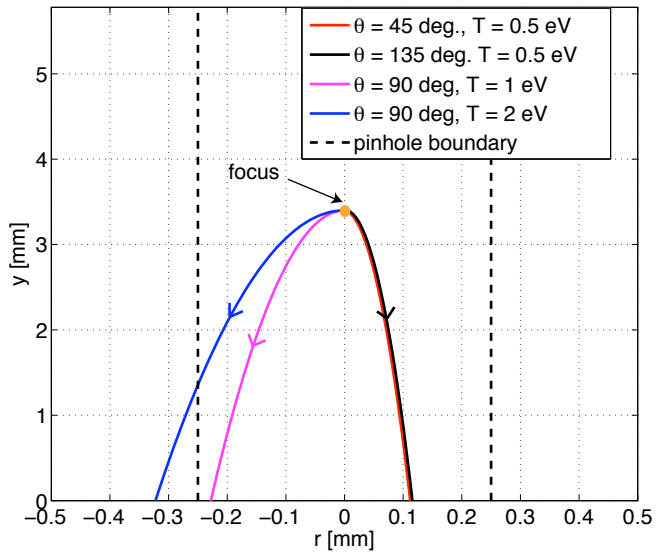

Figure 3.4: **Ion Trajectories.** Example ion trajectories in the extraction region of the mass spectrometer under typical conditions. Ions originate from the SMI focus 3.4 mm above the bottom plate. Note the difference in the r and y scales.

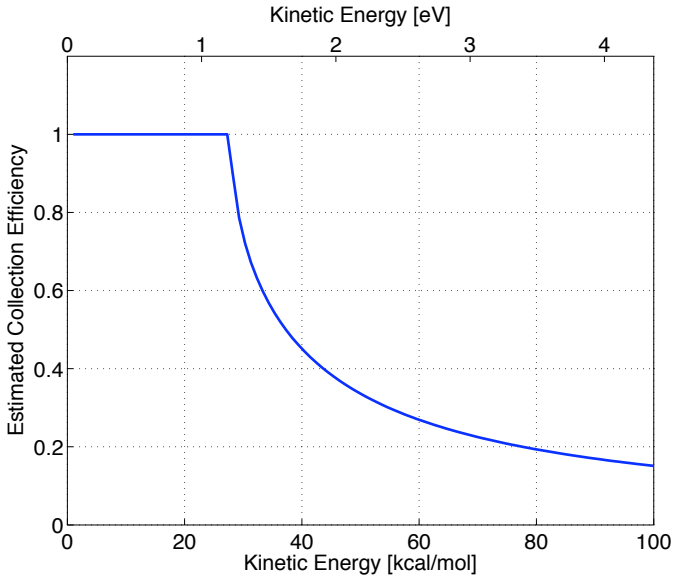

Figure 3.5: **KER dependent Collection Efficiency.** Collection efficiency for an isotropic distribution estimated with all ions originating from one point at the SMI focus.

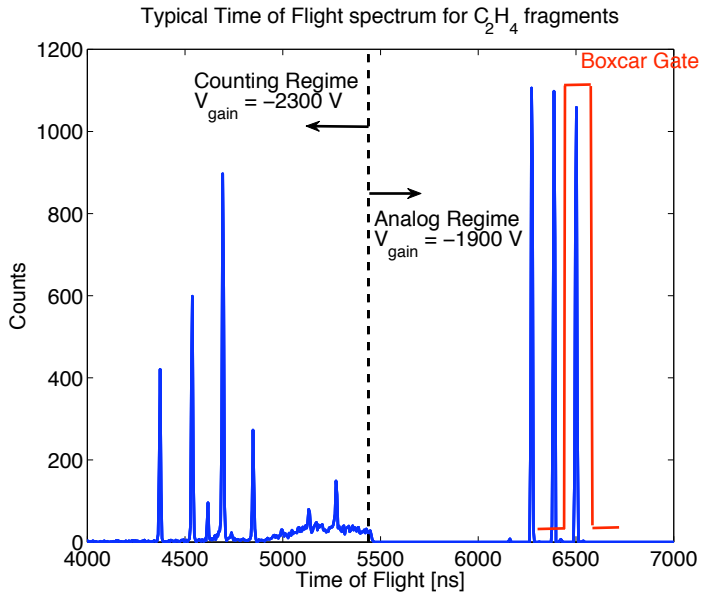

Figure 3.6: **Time of Flight Histogram.** Typical histogram for ion fragments of C_2H_4. The high voltage on the MCP (V_{gain}) is switched from -2300 V to -1900 V at 5.5 μs. to reduce the gain for fragments with rates of many ions per shot. The signal from fragments with rates of many ions/shot can be processed with a boxcar integrator. Note the broad background between 5 and 5.5 μs, these are ions from the unfocused beam.

rate y is somewhat less than one per shot, and (2) an "analog regime" in which the event rate is saturated at 1 per shot. To collect data in the analog regime, a boxcar integrator (Stanford Research Systems inc. model SR250) is used. While running a VUV pump/probe experiment, it is common to want to collect data in both regimes simultaneously. This is accomplished by switching the voltage V_{gain} applied to the MCP between ion fragment arrival times. A typical time of flight spectrum illustrating these two regimes is shown in figure 3.6. The signal and noise properties of these two regimes are discussed in the following two sections.

3.1.3 Discriminated Data in the Counting Regime

For ion fragments with signal rates in the range of a few ions per shot or less, the raw signal is processed with a threshold discriminator and a time digital converter. An ion fragment signal N_i (e.g. CH^+) is defined as the sum of all events within a certain TOF gate corresponding to this mass peak in the spectrum. If the mean number of detected ions in a given fragment per laser shot is μ, the probability $P_\mu(\nu)$ that ν ions are detected on a given shot follows Poisson statistics:

$$P_\mu(\nu) = e^{-\mu}\frac{\mu^\nu}{\nu!} \tag{3.8}$$

When the discriminator registers an event at a particular TOF, it does not tell us how many ions actually hit the detector, it just tells us that some number of ions hit the detector at that TOF. It is insensitive to the pulse height. The event rate seen by the discriminator is

$$y \equiv N_i/N_{shots} = \sum_{\nu=1}^{\infty} P_\mu(\nu) \tag{3.9}$$

The number of ions initiating a discriminator event is almost always one when $\mu \ll 1$, because from equation (3.8): $P_\mu(2)/P_\mu(1) = \mu/2 \ll 1$, and then $\mu \approx y$. However, as the mean ion rate μ increases, the probability of multiple ions hitting the detector at once but only being registered as one "hit" becomes appreciable. In this regime, the discriminator does *not* accurately record the ion rate because it cannot distinguish between one ion and two. This is illustrated graphically in figure 3.7 for several values of y.

However, when the discriminator does not record a hit, no ions hit the detector. The discriminator *does* accurately record the probability that a fragment was not detected on a given laser shot, or $P_\mu(0) = (1 - N_i)/N_{shots} = 1 - y$. Armed with the knowledge that the true ion signal follows Poisson statistics, we can calculate the true mean count rate from our measured $P_\mu(0)$:

$$P_\mu(0) = e^{-\mu} \tag{3.10}$$

$$\mu = -\ln\left(P_\mu(0)\right) = -\ln(1 - y) \tag{3.11}$$

The correction function $\mu(y)$ is shown in figure 3.8. Now we must also estimate the statistical error associated with the calculated quantity μ. For $y \ll 1$, $\mu \approx y$ and

$$\sigma_\mu \approx \sigma_y \approx \frac{\sqrt{N_i}}{N_{shots}} = \frac{\sqrt{y}}{\sqrt{N_{shots}}} \text{ (for } y \ll 1) \tag{3.12}$$

as is normal for a counting experiment. However, when y is not small, this formula is no longer valid since y no longer represents the true count rate. The uncertainty in y must be propagated using equation (3.11):

$$\sigma_\mu = \left|\frac{d\mu}{dy}\right| \sigma_y = \frac{1}{1 - y}\sigma_y \tag{3.13}$$

The uncertainty in y is also no longer given by equation (3.12) because y is *not* a count rate. So what is y? The discriminator event rate y is the average result of an experiment with a binary outcome: either at least one ion was detected or zero ions. This is similar to a coin flip or dice experiment. The statistics of y are thus governed by the binomial distribution for N_i discriminator events in N_{shots} [76]:

$$P(N_i, N_{shots}) = \frac{N_{shots}!}{N_i!(N_{shots} - N_i)!} y^{N_i}(1 - y)^{N_{shots} - N_i} \tag{3.14}$$

The statistical uncertainty in the number of events N_i in N_{shots} is given by [76]:

$$\sigma_{N_i} = \sqrt{N_{shots} y(1 - y)}. \tag{3.15}$$

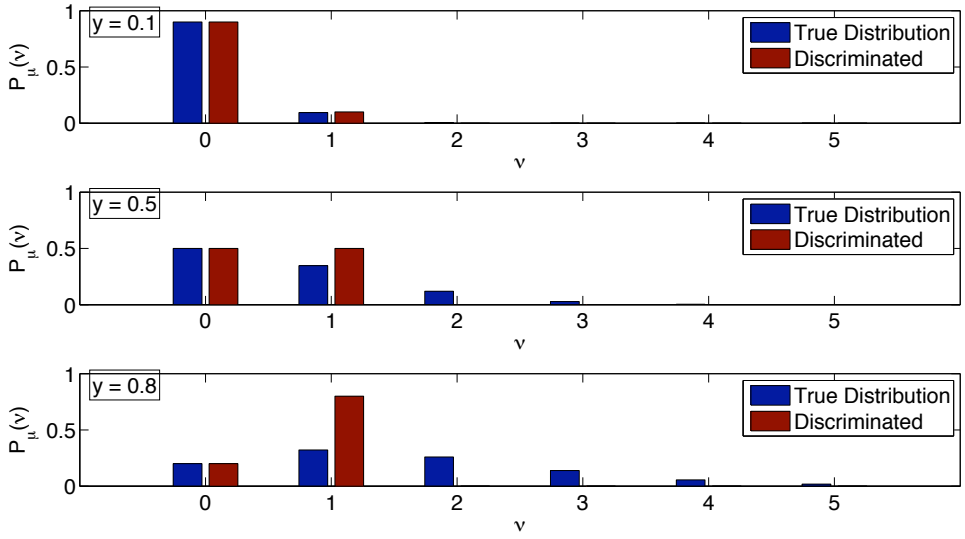

Figure 3.7: **Binary Detection.** Comparison between Poisson distribution of hits on the detector and events recorded by the discriminated. Note that the discriminator accurately records $P_\mu(0)$ regardless of μ

So the uncertainty in y is

$$\sigma_y = \frac{\sigma_{N_i}}{N_{shots}} = \frac{\sqrt{y(1-y)}}{\sqrt{N_{shots}}} \tag{3.16}$$

and the uncertainty in the quantity of interest μ is:

$$\sigma_\mu = \frac{1}{\sqrt{N_{shots}}}\sqrt{\frac{y}{1-y}} \tag{3.17}$$

Figure 3.9 shows how the non-ideal "binary" detection of the discriminator introduces error. I have plotted the fractional uncertainty $\sqrt{N_{shots}} \times \sigma_\mu/\mu$ versus the true ion rate μ for the discriminated data and the ideal detector capable of distinguishing multiple ions per shot. In the ideal case, the fractional uncertainty decreases as the inverse square root of the count rate, as expected. In the binary detection case, the error introduced in calculating μ is always higher than the ideal case and increases sharply as $y \to 1$.

3.1.4 Pulse Height Detection in the Analog Regime

For ion fragment channels with mean ion rates μ much greater than 1, the number of laser shots where no events are recorded becomes vanishingly small, and measuring the event rate y is no longer meaningful or practical. In this regime, I recorded the ion yield by integrating the signal corresponding to a given fragment with a boxcar integrator. The boxcar integrator integrates the area under a peak in the raw PMT signal and outputs a

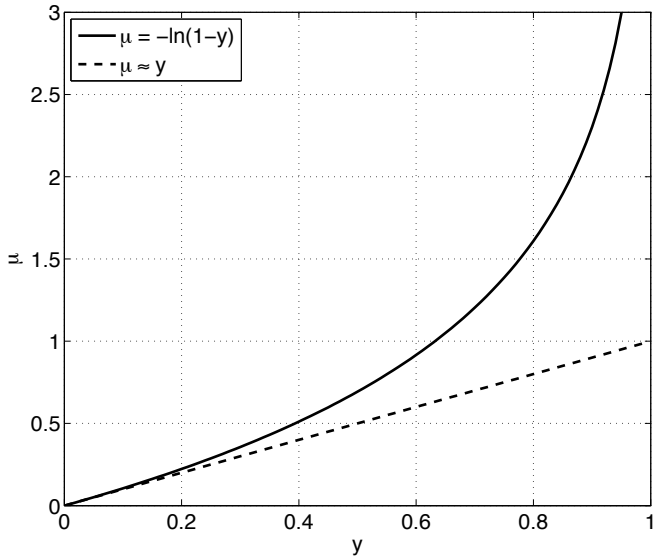

Figure 3.8: **Correction for Multiple Counts.** Comparison between true ion rate μ and event rate y

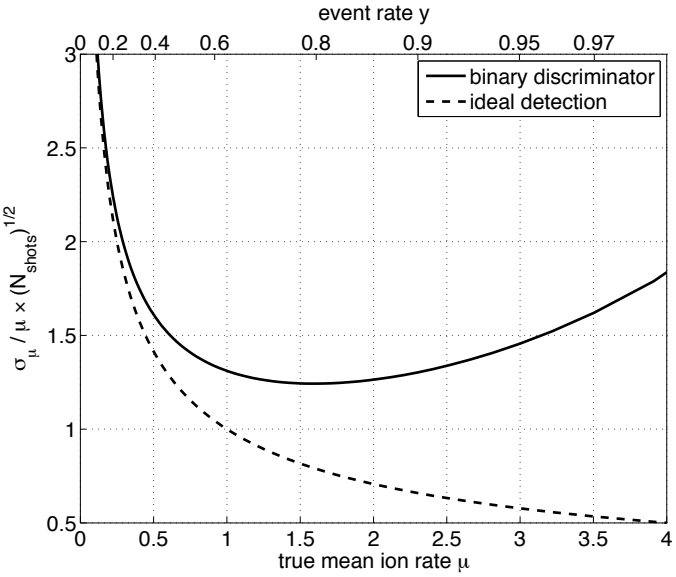

Figure 3.9: **Error Propagation.** Fractional Uncertainty (per shot) of μ in the ideal case and the binary discriminated case. The ideal case represents the so called "shot noise" limit

DC voltage proportional to this area. This DC voltage is then recorded shot by shot with an analog to digital converter.

When working with these high signals of many ions per shot, one can escape the cold, hard realities of counting statistics which are quite limiting when the laser repetition rate is only 10 Hz. Indeed, by processing these large signals with a boxcar integrator, one can get much closer to the "shot noise" limit of figure 3.9. Figure 3.10 shows a comparison of the noise characteristics of an analog ion signal ($C_2H_4^+$ in this case) estimated to be at about $\mu = 100$ ions/shot and the simultaneously recorded upstream ion plate intensity monitor (see section 2.3). The distribution for the ion fragment measured with the mass spectrometer is observed to be much broader than the incident intensity fluctuations. There is also no strong correlation between the signals. The signal to noise of the $C_2H_4^+$ is $\sim 10 = \sqrt{100}$, indicating that the signal is near the shot noise limit.

If a boxcar integrator is used for smaller signals in the range of a very few ions per shot ($y < 0.6$), the noise is dominated by the ion response pulse height distribution of the detector, and one is better off using the discriminated signal. In the intermediate regime where counting is saturated, but still workable ($0.8 < y < 0.95$), either method is found to be acceptable. Figure 3.11 compares the analog and discriminated signal processing on a fragment with $y = 0.91$ ($\mu = 2.4$). The agreement between the two signal processing schemes is excellent.

3.2 CaF_2 and MgF_2 window properties

The harmonic pulses have different group velocities in the CaF_2 window of figure 3.2 and are temporally separated at the exit of the window. The variation of a light pulse's group velocity with wavelength in a material is called group velocity dispersion (GVD). The data in figure 3.12 shows the time shifts introduced by the CaF_2 window on the fifth harmonic, third harmonic, and fundamental pulses. The CaF_2 window was inserted in both arms on the SMI so that both the pump and the probe consist of the time separated lower orders. With no photons with $hv > I_p$ present behind the CaF_2 window, ionization of the $C_2H_4^+$ target gas proceeds through multiphoton ionization (MPI) only. When pulses from the HOA and LOA are overlapped in time, the light intensity at focus is higher and the MPI signal is dramatically increased. The cross-correlation between the pulse sequences shows several peaks corresponding to the overlap of the pulses from the HOA and LOA. To collect this data, I used an aluminum coated mirror in the LOA arm, which had a high reflectivity for the 3rd/fundamental light as well as the fifth harmonic. The HOA mirror was a Mg/Si:C multilayer which also reflects all three wavelengths, but with different efficiencies.

The origin of the time axis in figure 3.12 was determined by turning off the gas cell and rotating the polarization of the drive laser so that it reflects off the Si mirror. In this configuration, only the 800 nm laser light is present. The strong-field ionization signal produced by the 800 nm laser light at focus is extremely sensitive to the spatio-temporal overlap of the two pulses, and the apparatus then becomes an interferometric autocorelator. The time zero of the interferometer with no group delay effects was then determined from the 800 nm laser autocorrelation trace.

Note that the shifts on the order of 10-30 fs between the signal peaks and the

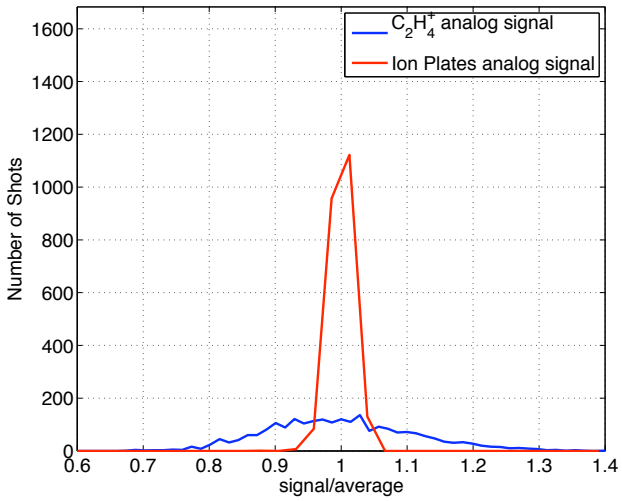

Figure 3.10: **Noise in Analog Detection.** Measured distribution of fluctuations of the boxcar integrated ion plate signal (red curve) and $C_2H_4^+$ signal. The $C_2H_4^+$ ion rate μ is estimated to be roughly 100 from the measure CH_2^+ event rate and the branching ratios of Ibuki et. al. [77]. The x axis has been scaled so that the mean value of both distributions is at $x = 1$.

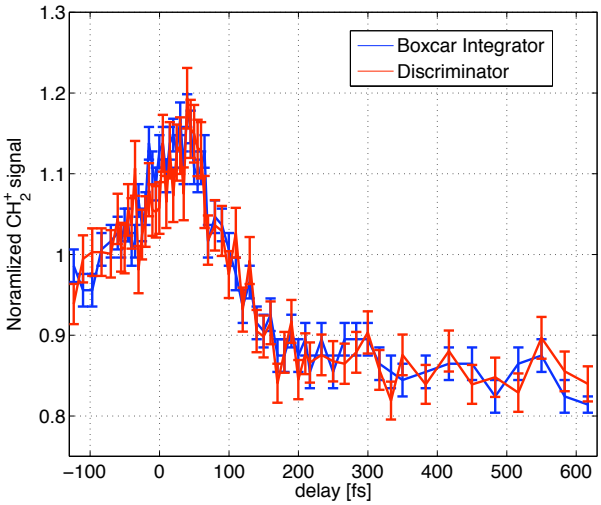

Figure 3.11: **Analog vs. Binary in the High Count Rate Regime.** Comparison of both signal processing schemes on a signal with a mean ion rate of about $\mu = 2.4$.

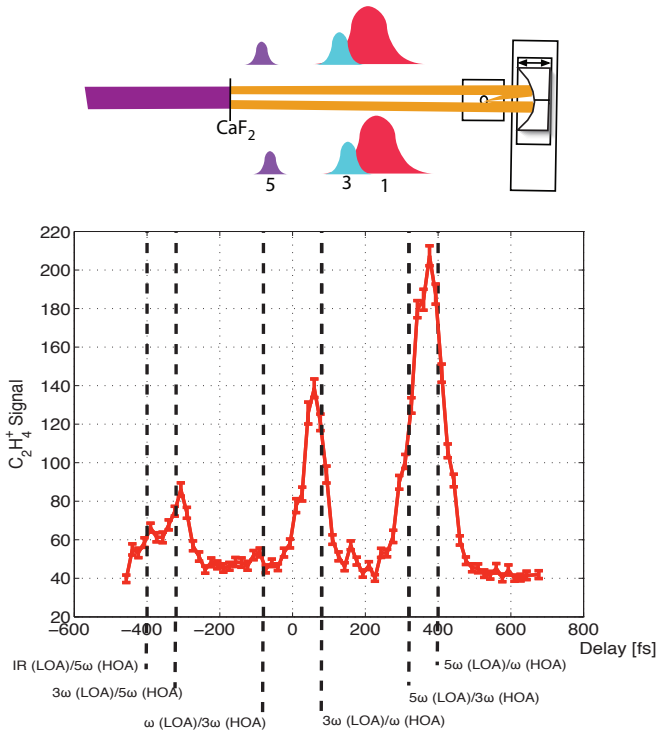

Figure 3.12: **Order Separation with a CaF_2 window.** The cross correlation in a C_2H_4 shows the temporal separation between the fundamenta, 3rd, and 5th harmonics. The vertical lines show the positions of temporal overlap from the harmonics in the LOA and HOA predicted from the values in table 3.1 for a thickness of 230 μm. An aluminum mirror was used in the LOA which had a high reflectivity for 3rd/fundamental light.

	ω/ω_0	n	k' [fs/μm]	k'' [fs^2/μm]
LiF	1 (800 nm)	1.389	4.65	0.026
	3 (267 nm)	1.415	4.93	0.101
	5 (160 nm)	1.484	5.83	0.339
	7 (114 nm)	1.705	11.32	3.78
MgF_2	1	1.375	4.60	0.023
	3	1.398	4.85	0.092
	5	1.461	5.74	0.370
CaF_2	1	1.430	4.79	0.032
	3	1.462	5.13	0.125
	5	1.553	6.47	0.593

Table 3.1: **Flouride Window Properties.** Index of refraction, group delay, and group delay dispersion, for the harmonics of 800 nm in fluoride windows. MgF_2 results are for the ordinary index of refraction.

vertical lines in figure 3.12 labeling the calculated temporal overlap positions between the harmonic orders are expected for two reasons. The first is the molecular dynamics of the intermediate ethylene V-state populated by the fifth harmonic or multiphohton excitation with the fundamental (see chapter 4). The second is the that the harmonic pulses can start out with small time shifts with respect to the fundamental due to the ionization gating effects in HHG (see chapter 2).

GVD also affects the pulse length [1, 19] of the transmitted harmonic pulses. For a chirped Gaussian input pulse with full width at half maximum (FWHM) τ_0, and initial chirp β, described by

$$E(t) = E_0 \exp\left[-2\ln 2\left(\frac{t}{\tau_0}\right)^2 + i\beta t^2\right]\exp(i\omega t), \tag{3.18}$$

the pulse length after propagating through a window of thickness L is

$$\tau(L) = \tau_0\left[(1+2k''L\beta)^2 + \left(\frac{4\ln(2)k''L}{\tau_0^2}\right)^2\right]^{1/2}. \tag{3.19}$$

To select the material and appropriate thickness of the fluoride window, I performed calculations for LiF, MgF_2, and CaF_2 for their respective ranges of transparency [11]. Table 3.1 lists the index of refraction n, group delay ($k' = n_g/c$), and second order dispersion term $k'' = d^2k/d\omega^2$ for the 3rd, 5th, and 7th harmonics of 800 nm. The index of refraction data and fits of LaPorte et. al. [78] were used for MgF_2 and LiF. Data of Daimon and Masumura [79] was used for CaF_2.

Figure 3.13 shows the output pulse length predicted by equation (3.19) as function of CaF_2 window thickness. The dashed curves are for transform limited input pulses ($\beta = 0$). Unlike harmonics generated in perturbative nonlinear optics, harmonics generated in the strong field regime acquire an intrinsic negative chirp due to the intensity dependence of the atomic dipole phase [80, 81]. The solid curves are for $\beta = -3 \times 10^{27}$ rad/s^2, predicted by the expression of Sekikawa *et al.* for a peak drive laser intensity of 3×10^{14} W/cm^2. For window thicknesses of a few hundred microns, the third and fifth harmonics are separated by hundreds of femtoseconds, while the effect of GVD on the pulslength is minor for pulses of 20 fs or longer. Figure 3.13 indicates that the window thickness should be less than 300 μm to avoid stretching of the fifth harmonic pulse.

3.3 Alignment Tricks

For pump/probe measurements, the two foci from the SMI mirrors must be spatially overlapped. The foci are less than 10 μm in diameter, so their overlap must be aligned to a high precision. The range of travel of the HOA translation stage is also only 250 μm. To ensure that the time zero of pump/probe delay falls near the middle of the translation stage's range of motion, relative longitudinal position of the LOA and HOA mirrors must also be determined to $\pm \sim 10$ μm. This must be accomplished with the Magnus chamber vented to air, because unless you have a midget in a space suit, there is no way to move the time zero to within the range of the piezo stage once the chamber is pumped out.

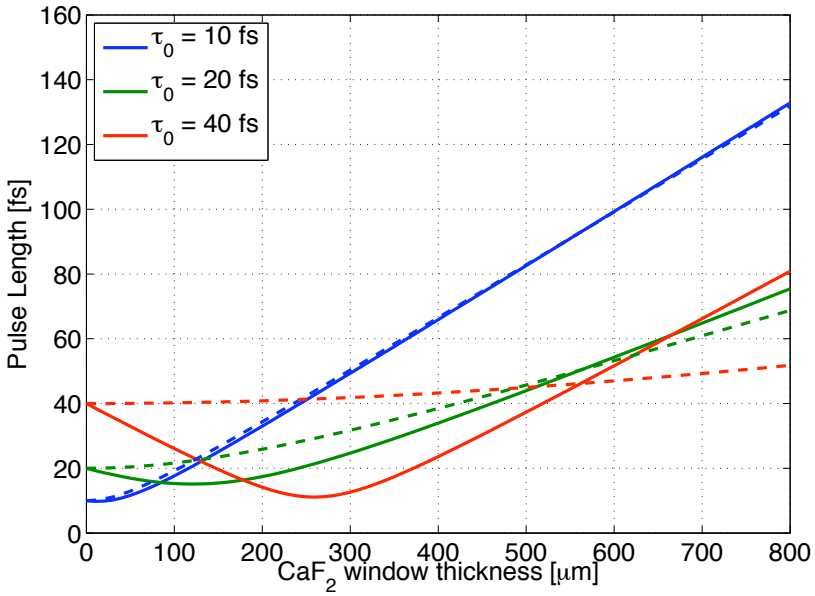

Figure 3.13: **Fifth Harmonic Pulse Compression.** Fifth harmonic pulselength vs. propagation distance in CaF_2. Solid curves are for chirped input pulses with $\beta = -3 \times 10^{27}$ rad/s^2. Dashed curves are for transform limited input pulses with $\beta = 0$.

If the LOA and HOA mirrors have comparable reflectivities for the 800 nm laser (e.g. Aluminum), alignment of the SMI can be performed by generating white light (WL) [82] at the SMI foci with 800 nm laser light. To do this, the polarization of the 800 nm laser is rotated so that some 800 nm laser light is reflected from the Si mirror. The rest of the HHG beamline must be under vacuum to avoid damage to the Bob chamber optics and the Si mirror due to self focusing of the laser in air. Let's denote the vertical tip/tilt angle of the LOA mirror θ_y (pitch), the horizontal θ_x (yaw), and the pump probe delay stage position z (delay). The maximum WL signal is generated when the intensity at focus is highest, or when the two SMI foci are overlapped in θ_x, θ_y, and z. To reduce the number of degrees of freedom to two, one starts by stretching the 800 nm pulse length to several picoseconds by detuning the compressor grating separation. The WL generation is then relatively insensitive to z. One can get the spatial overlap pretty close by imaging the fluorescence from the laser produced plasma at focus with a CCD camera. Fine tuning is then achieved by maximizing the WL signal by varying θ_x and θ_y. The time overlap is then found by compressing the pulse again and maximizing the WL signal by varying z. If you're lucky, the time zero falls within the 250 μm travel of the piezo stage. If you're unlucky, you need to nudge the LOA mirror position by hand and try again.

The dichroic 5th harmonic mirror, however, did not reflect the IR sufficiently for the WL alignment procedure to work. To align this mirror, a mechanical position indicator was used (Heidenhain gmbh). The position indicator was mounted on an x-y-z translation

stage (I-stage). In step one, the position indicator tip is slowly moved with the I-stage until it touches the LOA mirror surface near the edge and changes the indicator reading. In step 2, the piezo stage position, z, is set to be as far away from the indicator as possible and the SMI assembly is translated sideways so that the position indicator arm now points at the HOA mirror near its edge. In step 3, time zero is found by slowly incrementing z until the HOA mirror surface contacts the indicator tip, and the indicator reading changes. If the time zero is not in the desired location in the delay stage travel, the mirror position is nudged by hand and steps 1-3 repeated.

With some confidence in the time zero from the mechanical measurement, the spatial overlap must then be achieved in vacuum with the photo-ion signal. Fortunately there is a trick to reduce the parameter space that must be searched from two dimensions to one. As discussed in section 3.1, the time of flight of an ion born between the extraction plates is extremely sensitive to the height above the bottom plate. The θ_y position can be aligned by observing the ion time of flight spectrum produced by multiphoton ionziation from the LOA and HOA mirrors. If the θ_y position of the LOA mirror is off, two peaks can observed in the time of flight spectrum (TOF), one corresonding to the focus of each mirror. The θ_y position is adjusted until only one peak in the TOF is observed. The last degree of freedom, θ_x, can then be determined with a spatial cross-correlation of the 5th harmonic from the LOA and 3rd/IR from the HOA. To do this, the CaF_2 mirror is inserted in both arms of the interferometer, and the delay position z is set to correspond to the rightmost peak in figure 3.12. A scan of θ_x will have a large peak corresponding to the spatial overlap position.

3.4 Fifth Harmonic at Focus

The fifth harmonic has a photon energy of 7.7 eV and can ionize molecules through 2 photon absorption. The two photon ionization signal scales as the intensity of the fifth harmonic squared. Figure 3.14 shows the I^2 scaling of the two photon ionization of oxygen molecules. The fifth harmonic power behind a 160 nm bandpass filter (Acton Research Corp. 160-N) was varied by changing the Ar gas pressure in the cell, as described in section 2.5. The O_2^+ yield is fit with a power law of the form $y = ax^b$ with $b = 1.9 \pm 0.2$.

The fifth harmonic multiphoton ionization signal can be used to characterize the spatial profile of the fifth harmonic at focus. Spatial cross-correlations of the two fifth harmonic foci using multiphoton ionization of C_2H_4 are shown in figure 3.15. The harmonics were generated in Ar with a gas cell feedline pressure of 4.1 Torr. I modeled the spatial profiles with Gaussian fits to estimate the beam size. The fit to the vertical cross-correlation has a FWHM of 6 μm. The cross-correlation is observed to be three times larger in the horizontal for a FWHM of 18 μm. The main source of the poor beam quality in the horizontal plane is likely the sharp edge in each half beam produced by the gap between the mirrors. Another source could be the larger illuminated area of the Si mirror in the horizontal plane (see figure 2.9). Assuming the vertical cross correlation represents the cross correlation of two Gaussian beams, the vertical beam size at focus is 6 μm/$\sqrt{2}$ = 4.2 μm FWHM, corresponding to an M^2 for the fifth harmonic of roughly 2.

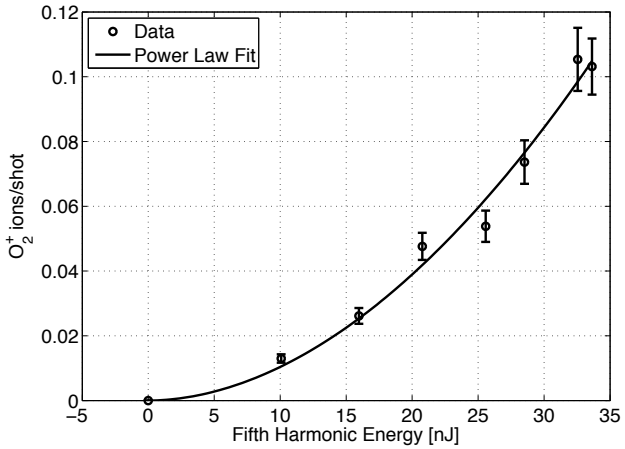

Figure 3.14: **Multiphoton Ionization of O_2.** O_2^+ yield versus fifth harmonic power. The fifth harmonic filter was inserted in both arms of the SMI and the power of the fifth harmonic varied by changing the Ar gas cell pressure. The data is fit with a power law of the form $y = ax^b$. The result of the fit is $b = 1.9 \pm 0.2$.

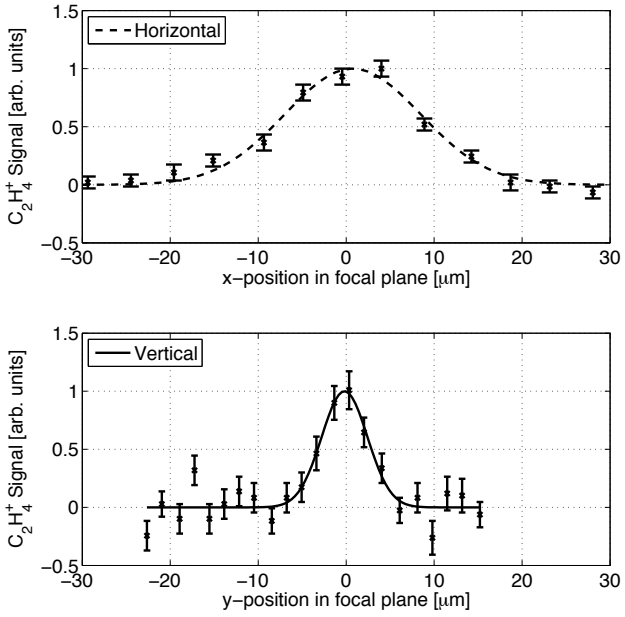

Figure 3.15: **Fifth Harmonic Profile at Focus.** Multiphoton ionization of C_2H_4 as a function of the overlap of the two SMI foci in the horizontal (top) and veritcal (bottom) directions. Gaussian fits give a fifth harmonic focus size of 4×12 μm.

Chapter 4

Ultrafast Internal Conversion In Ethylene

I can't tell you if the use of force in Iraq today will last five days, five weeks or five months, but it won't last any longer than that.

-Secretary of Defense Donald Rumsfeld

The ultrafast internal conversion of photo-excitation energy into a directed molecular motion or chemical reaction is a process of fundamental importance in nature. Two important examples were mentioned in chapter 1, the isomerization of excited rhodopsin molecules [7] and the quenching of electronic excitation in DNA bases [18]. Several trends emerge from the studies of these complex systems and many others. First, conical intersections between different electronic states dominate the dynamics by providing the path for electronic relaxation [17]. Second, the dynamics are often initiated by the promotion of an electron in a π orbital of a double bond or conjugated double bond to an antibonding π^* orbital [83]. This allows the molecule to flex around the double bond and rapidly find the non-radiative decay path.

The simplest molecule with a carbon double bond is ethylene (C_2H_4), yet even this simple case exhibits rich internal conversion dynamics. In this chapter, I will present a series of pump-probe measurements which track the dynamics of ethylene upon $\pi \rightarrow \pi^*$ excitation from the initial excitation all the way to dissociation on the ground state potential energy surface.

4.1 The "Simplest" Double Bond

Ethylene is an extremely important molecule, both industrially and in nature. As the precursor to polyethylene (shopping bags) and polyvinyl chloride (PVC pipes), ethylene is the most produced organic compound in the world [84]. In 2005, global production exceeded 10^8 metric tons. Ethylene is also an important hormone in plants. Ethylene

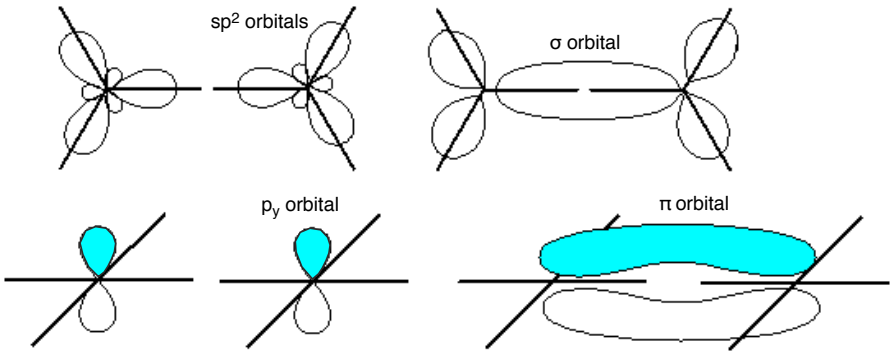

Figure 4.1: **Bonding in Ethylene.** The hybridized carbon sp^2 orbitals of ethylene form the σ bond of ethylene's double bond. The remaining p_y orbitals form the π bond, which keeps the molecule in a planar geometry. Adapted from [89].

regulates many aspects of the plant life cycle, including seed germination, root initiation, flower development, fruit ripening, senescence, and responses to stress [85].

The industrial and biochemical uses of ethylene stem from its carbon double bond. Bonding in ethylene is the textbook example of a double bond and sp^2 hybridization of carbon's valence electrons [86]. Figure 4.1 shows how the orbitals of two CH_2 groups arrange to form the double bond of C_2H_4. The valence electrons from the carbon atom arrange into three sp^2 orbitals and an orthogonal p_y orbital. The sp^2 orbitals oriented along the C-C axis form the σ orbital of the double bond. The remaining p_y orbitals form the π bond, the highest occupied molecular orbital (HOMO) of the molecule. Ethylene is the simplest molecule with a carbon-carbon double bond, or the simplest alkene. The energy of the π orbital is lowest in a planar configuration of the molecule, and it is the π bond that is responsible for ethylene's stiffness. The potential energy goes up roughly 3 eV higher [16] if one of the CH_2 groups is twisted 90°, and the vibration corresponding to torsion around the C=C bond has the high fundamental frequency of 1026 cm^{-1} [87]. For comparison, the ethane molecule(C_2H_6), without the double bond, has the much lower torsional frequency of 289 cm^{-1} [88].

The π orbital is the result of the in-phase combination of the two p_y oribitals; the positive lobes of the p_y wave function combine on the same side of the molecule. An out of phase combination is also possible, which leads to an anti-bonding orbital with a node between the carbon atoms. The anti-bonding orbital is commonly termed π^*. The π and π^* oribtals of ethylene are illustrated in figure 4.2. Unlike the π orbital, the energy of the π^* state is much lower in a twisted configuration [16, 90].

An electron in the π orbital can be promoted to the π^* orbital through the absorption of a photon in the vacuum ultraviolet. As a prototypical system, the VUV excitation and subsequent photodissociation of ethylene have been the subject of extensive studies. Ethylene's first absorption band, shown in figure 4.2, peaks around 165 nm. The oscillator strength of the broad continuum is dominated by the $\pi \rightarrow \pi^*$ transition [92, 93], but also spectrally overlaps with transitions to 3s and 3p Rydberg states [92, 94]. Mulliken [93]

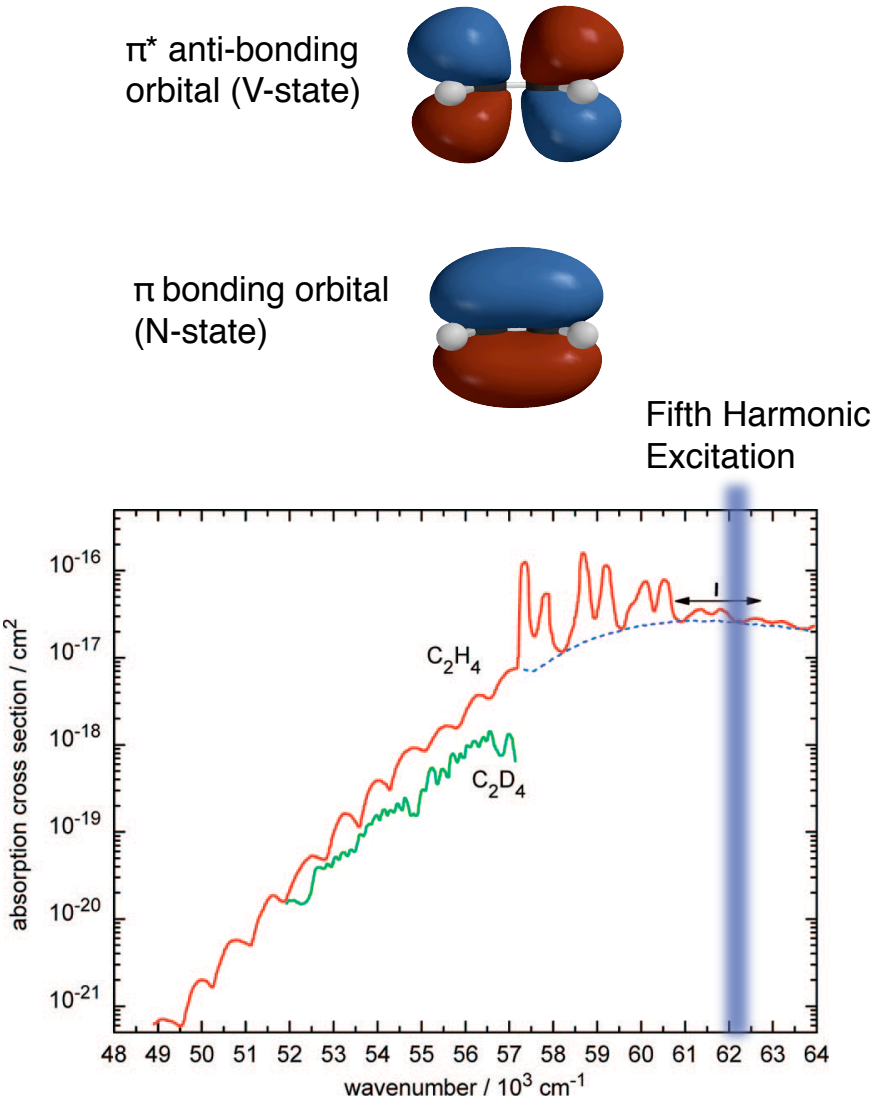

Figure 4.2: **VUV Absorption Spectrum of Ethylene.** The VUV absorption spectrum is shown along with the HOMO π orbital and LUMO π^* orbitals. Superposed on the the broad $\pi \rightarrow \pi^*$ transition are peaks due to excitation of the 3s and 3p Rydberg states. The wavelength band of the fifth harmonic at 62,000 cm^{-1} is shown in purple. Absorption data is adapted from [91], orbital diagrams are from [89].

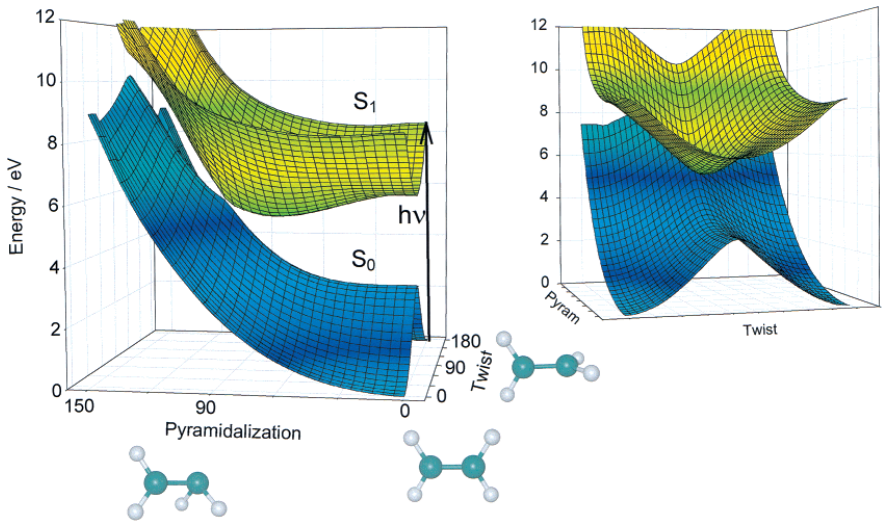

Figure 4.3: **Twist-Pyramidilization Conical Intersection.** Theoretical potential energy surfaces of the ethylene molecule from ref. [16]. Photon excitation starts a wavepacket on the S_1 (V) surface from the planar equilibrium geometry of the ground state. The nuclear wavefunction quickly finds the conical intersection, transitioning to the S_0 (N) surface.

established the labels N for the ground state in which the π orbital is filled (π^2) and V for the valence excited state ($\pi\pi^*$). Also energetically in the vicinity of the V state is a doubly excited state with zwitterionic character labelled Z (π^{*2}). VUV Resonance Raman studies [87] of ethylene indicate that a combination of twist, C-C stretch, and pyramidilization motions are launched upon $\pi \rightarrow \pi^*$ excitation, as would be expected from inspection of the π and π^* orbitals.

Because of ethylene's small size, the dynamics following $\pi \rightarrow \pi^*$ excitation have served as an important benchmark case for ab initio calculations using various techniques [16, 95, 96, 97, 94, 98] that seek to predict the non-adiabatic dynamics of larger systems. The calculations predict that the molecule relaxes to the ground state N through two conical intersections, one occuring at a twisted and pyramidilized structure and the other near an ethylidene configuration (CH_3CH), in which one of the hydrogens has migrated across the double bond. The energy of the VUV photon is thus converted into vibrational excitation on the ground state potential energy surface (PES). The molecule subsequently dissociates from the ground state PES. The PES's for the N and V states calculated by Ben-Nun [16] in the vicinity of the twist-pyramidilization conical intersection are shown in figure 4.3.

Experimentally, the asymptotes of the dynamics have been studied in detail. The molecule is observed to eventually dissociate via two main channels: (1) Eliminating a hydrogen molecule (H_2) or (2) eliminating two hydrogen atoms (2H). The group of Y.T. Lee has conducted several studies of the kinetic energy distributions of the photodissociation products from ethylene and its di-deuterated forms (e.g. CH_2CD_2) after 157 nm excitation [99, 100, 101, 102]. The studies of deuterated isoptomers illuminate pathways for hydrogen

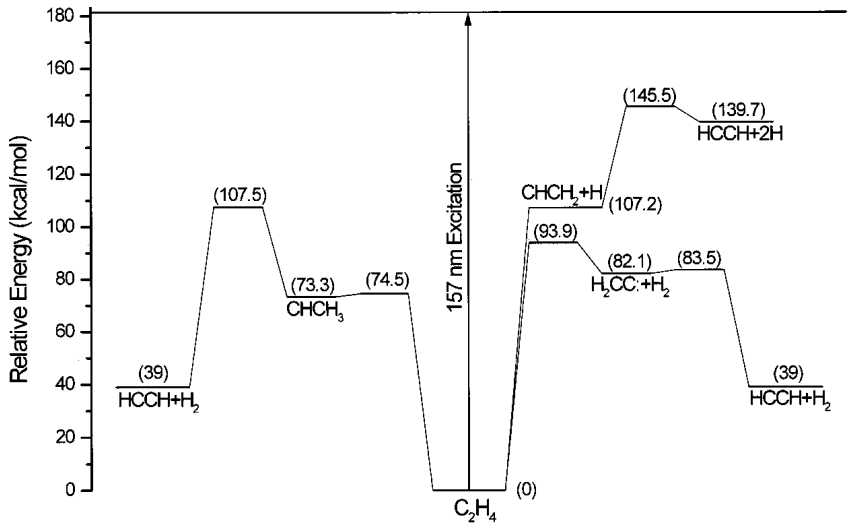

Figure 4.4: **Energies of Ethylene Configurations.** The potential energies of the asymptotes and transition states of ethylene, relative to the ground state. From ref. [100].

molecule elimination and provide indirect evidence for a fraction of the dissociating population proceeding through the theoretically predicted ethylidene configuration. For example, H_2 and D_2 molecules can be eliminated from trans HDC=CHD. However, the differences observed between HD elmination from trans HDC=CHD and cis HDC=CHD show that the hydrogens are not randomized.

Calculated potential energies [100] of different configurations of the ethylene molecule and the asymptotes of dissociation are shown in 4.4. The atomic hydrogen elimination ($2H$) channel is $\sim$ 100 kcal/mol higher in potential energy than molecular elimination due to the binding energy of H_2. This leaves much more energy to be distributed in the kinetic energy and internal vibrational energy of the fragments in the H_2 elimination case. Analysis of the kinetic energy distributions of the fragments shows that most of this energy difference manifests itself as vibrational excitation of the C_2H_2 and H_2 fragments, which from the fragment kinetic energy distributions is calculated to be 3.7 eV (85 kcal/mole) higher on average in the H_2 channel [101]. Figure 4.4 also shows that the vinylidene (H_2CC:) configuration of acetylene (C_2H_2) is 82.1-39 kcal/mol (1.9 eV) higher than the ground state of acetylene. This energy difference is observable in the kinetic energy distribution of HD molecules from H_2CCD_2, which is shifted to higher energies than the H_2 or D_2 kinetic energy distributions. Further indirect evidence for hydrogen migration comes from the presence of the dissociation channel $CH_2CD_2 \rightarrow C_2H_2 + D + D$, which should be energetically forbidden if both D atoms come off the same side of the molecule and the C_2H_2 molecule is left in the energetically higher vinylidene configuration [101].

4.2 Previous Time Resolved Work

The complex dynamics involving multiple transition states discussed above make ethylene an ideal candidate for femtosecond spectroscopy, and time resolved measurements can provide important constraints for theory. However, ethylene's small size puts its excitation and ionization energies in the VUV, beyond the spectral range of conventional femtosecond pump/probe techniques. As a result it has been the subject of relatively little time resolved work.

An early attempt at a time resolved measurement of the excited state dynamics was made by Farmanara et. al [103] using pump pulses at $\lambda = 155$ nm and probe pulses at $\lambda = 258$ nm. The pump pulse was generated by near resonant four-wave difference frequency mixing in argon, and this method produced rather long pulses in the range of 350-450 fs. Ionization of the molecule proceeds through the absorption of a $\lambda = 258$ nm probe photon from the excited V-state surface. Despite the poor time resolution, a time constant for the decay of the $C_2H_4^+$ signal of 40 ± 20 fs was estimated from the shift of the peak of the pump-probe cross-correlation from time zero. A similar measurement was performed by Mestdagh et. al. [104] using ~ 180 fs fourth harmonic pulses for the pump, with an extracted time constant of 20 ± 10 fs for the decay of the $C_2H_4^+$ signal.

In addition to the poor time resolution, these measurements are complicated by a detection window effect [97]. The sum energy of the pump and probe pulses only barely exceeds the ionization potential of ethylene, and the probe can only ionize the molecule from a small portion of the V-state PES. The measured time constant does not necessarily then give the excited state lifetime, but rather the time the molecule resides in a region of the PES where it is still energetically possible to ionize it.

To try to overcome the detection window and provide slightly better time resolution, Stert et. al. [105] probed the V-state dynamics through multiphoton ionization (MPI) with intense 400 nm and 800 nm laser pulses. Again, a very short time constant of (~ 10 fs) was observed for the decay of $C_2H_4^+$ signal. However, now the multiphoton probe was capable of leaving the ion in its first excited state ($\tilde{A}$) which can dissociate to produce $C_2H_3^+$ and $C_2H_2^+$ signals. The cross-correlations for these signals peak at a later delay than $C_2H_4^+$ and indicated a second time constant in the decay of the V-state. Recently, an experiment using 160 pump pulses and intense 800 nm probe pulses has been conducted by Kosma et. al. [91] with 11 fs time resolution. They again observe two decay times in the decay of the $C_2H_4^+$ (21 fs), and $C_2H_3^+/C_2H_2^+$ (17 fs) signals. They also observe oscillations in the photo-ion yields which they assign to a combination of torsion and C-C stretch vibrations.

Since the ionization of the excited V state requires at least three 800 nm photons, in these experiments the probe pulse must be intense to produce a photoion signal and may not be a perturbation. The MPI signal is complicated by the presence of AC stark shifts, intermediate resonances, and the increasing number of photons required to ionize the molecule as the valence excitation decays. Indeed, at longer delays, as the molecule relaxes to the ground state PES, higher intensities are needed to produce a photo-ion signal and interpretation of the MPI data is even more problematic. The complexity of the MPI probe also makes direct comparison to theory difficult. An attempt to numerically simulate the experiment must not only accurately calculate the non-adiabiatic dynamics initiated by the pump pulse, but the complex MPI process. With single photon ionization, direct

comparisons between theory and experiment are more feasible [106].

In the present work, I performed pump-probe experiments on ethylene using a range of VUV and XUV wavelengths from the HHG source. The results allow one to track the dynamics from photoexcitation all the way to dissociation. In a first step, similar to a recent demonstration by Conde et. al. [107], I measured the dynamics on the V state PES using 7.7 eV photons for both pump and probe. As in the multiphoton probe studies, two time scales for the decay of the electronic excitation are observed. To follow the dynamics onto the ground state PES, I also conducted experiments using a band of XUV harmonics ($h\nu = 17 - 23$ eV) for the probe. These XUV photons can break the C-C bond, revealing transient structures of the molecule, or directly photo-ionize the H_2 dissociation product. In both experiments, the pump and probe pulses act on the molecule perturbatively through single photon excitation.

4.3 7.7 eV pump/7.7 eV probe results

Barbatti et. al. [97] calculated that in order to measure the excited state lifetime of ethylene without detection window effects, the probe photon energy in a pump/probe experiment should be greater than 7.4 eV. This is the energy required for vertical ionization from the two minimum energy conical intersections (MECI) discussed above. Thus, within the Franck-Condon approximation, a 7.4 eV probe photon can ionize the molecule from the V-state PES, but not from the ground state PES below the conical intersections. To measure the lifetime of the wavefunction on the V-state surface, I thus used the fifth harmonic at 7.7 eV for the probe as well as the pump. Energetically, two fifth harmonic photons is sufficient to produce the ion signals $C_2H_4^+$, $C_2H_3^+$, and $C_2H_2^+$ [77].

To deliver the 5th harmonic at 7.7 eV for both pump and probe, harmonics were generated using 8 Torr of Argon for the gas cell feedline pressure. To select only the fifth harmonic in each arm of the SMI, a spectral bandpass filter (Acton Research 160-N on 0.2 mm MgF_2 substrate) was inserted in both arms. The filter has a transmission of 17 % for the fifth harmonic and $< 10^{-4}$ for everything else. The LOA mirror had a UV enhanced aluminum coating (CVI Laser DUVA). The HOA mirror was a Mg/Si:C multilayer. The HOA multilayer mirror was optimized for reflecting the 19th harmonic, but its 5th harmonic reflectivity was sufficient to conduct the experiment without having to vent the chamber and install/align another mirror. Neat ethylene was introduced at focus with the piezo-electric valve/skimmer discussed in section 3.1. Signals were recorded at several backing pressures between 1 and 10 psi gauge to be sure that the results were not affected by clusters in the molecular beam.

Since the pump and probe pulses are the same, the pump/probe delay traces are symmetric around time zero. The photo-ion signals are shown in figure 4.5. The finite instrument response function (FIR, convolution of pump and probe pulses) is estimated to be a gaussian with FWHM 25 ± 7 fs based on the simultaneously recorded two photon ionization of background water molecules. The extra width of the ion yields in figure 4.5 is due to the excited state lifetime of the ethylene V state. The $C_2H_4^+$ parent ion signal quickly decays as the nuclear wavefunction moves away from the Franck-Condon region and acquires kinetic energy, while the $C_2H_3^+$ and $C_2H_2^+$ signals persist for longer delays as the

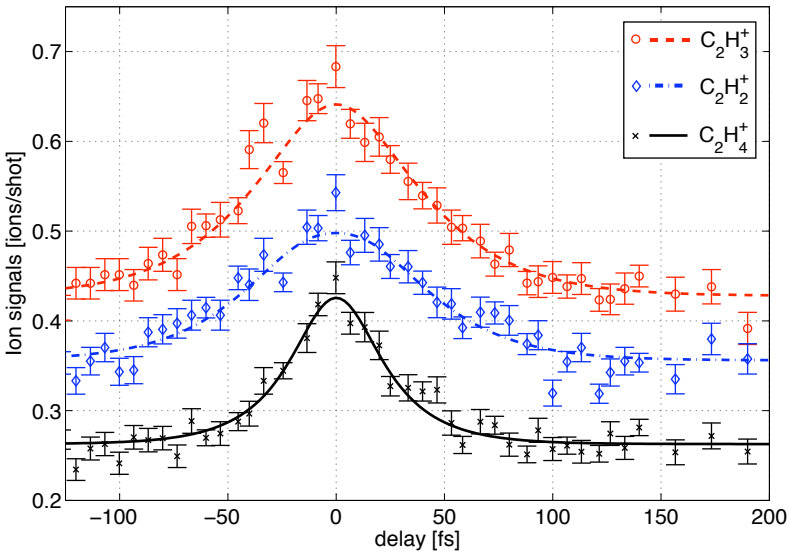

Figure 4.5: **Excited state dynamics.** Time resolved photo-ion yields from 7.7 eV pump/7.7 eV probe experiments. The $C_2H_4^+$ signal (black x's) is modeled with a single exponential decay with a time constant of 21 fs convolved with the finite instrument response (solid black curve). The $C_2H_3^+$ (red circles) and $C_2H_2^+$ (blue diamonds) signals are modeled with a two step exponential decay model described in the text.

nuclear wavefunction samples the V state PES, eventually vanishing as the molecule relaxes non-adiabatically to N.

For comparison with previous work, I modeled the signals with exponential decays. The $C_2H_4^+$ signal is fit to a single exponential decay with time constant $\tau_1 = 21 \pm 4$ fs convolved with the FIR (solid black curve in figure 4.5). For the $C_2H_3^+$ and $C_2H_2^+$ signals, I used the two step exponential decay model proposed by Mestdagh [104] and indicated by the MPI probe studies discussed above. The signals before convolution with the FIR are assumed to have the form

$$S(t) = A_1 e^{-t/\tau_1} + A_2 \frac{\tau_2}{\tau_2 - \tau_1} \left[1 - e^{-\left(\frac{1}{\tau_1} - \frac{1}{\tau_2}\right)t} \right] e^{-t/\tau_2} \tag{4.1}$$

Equation (4.1) describes the signal as occurring from two locations on the potential surface with decay constants τ_1 and τ_2. The population at location L_1, near the initial Franck-Condon region, decays with time constant τ_1 and gives rise to population at location L_2, which decays to the ground state. The signal amplitude for ionization from locations L_1 and L_2 are A_1 and A_2, respectively. I took τ_1 to be the decay constant of the $C_2H_4^+$ signal, as in [91, 105]. Convolving equation (4.1) with the FIR and fitting to the $C_2H_3^+$ ($C_2H_2^+$) data gives $\tau_2 = 27 \pm 5$ fs (23 ± 6 fs).

The $C_2H_3^+$ and $C_2H_2^+$ data taken by themselves do not indicate the two step decay model over a single exponential decay or another model. If the $C_2H_3^+$ ($C_2H_2^+$) data is

modeled as a single exponential decay convolved with the FIR, the result is a decay time constant of 41 ± 4 fs (39 ± 6 fs). All of the uncertainty intervals listed here correspond to to 67% variation of χ^2 as the fit parameter is varied [76]. Regardless of the model used, the data indicate a lifetime for the excited electronic state of less than 50 fs, in agreement with the MPI probe studies.

4.4 7.7 eV pump/XUV probe results

To follow the dynamics onto the ground state PES, I conducted experiments using the XUV harmonics 11, 13, and 15 for the probe ($h\nu = 17 - 23$ eV). The harmonics were generated using 2.4 Torr of Xenon in the gas cell. The XUV probe photon energy band was selected with a 0.16 μm thick tin (Sn) foil and a B_4C coating on the probe arm mirror [108]. The probe photons now produced an ion signal from both excited and unexcited molecules, so it was necessary to pump a larger fraction of molecules in the focal volume, and the loss from the 160 nm bandpass filter was unacceptable. To select the 5th harmonic for the pump, I instead used a dichroic mirror with high reflectivity ($R > 90\%$) for 160 nm and a low reflectivity for residual 3rd harmonic and fundamental light (Layertech gmbh). To further discriminate against any other orders, a 230 μm thick CaF_2 window was inserted in the pump arm (see chapter 3). The CaF_2 window blocks all harmonic orders greater than 5 and temporally separates the 5th harmonic from residual 3rd harmonic and fundamental light. Thus, residual 3rd harmonic and fundamental light pulses arrive at the focus more than 300 fs earlier than the 5th harmonic, and being non-resonant with with the C_2H_4 target gas, pass through unabsorbed and do not corrupt the experiment. I confirmed this by scanning the pump/probe delay to the large negative delays where the 3rd and fundamental would be coincident with the probe. No effects on the photo-ion yields were observed. The mirrors and filters were moved perpendicular to the beam path to adjust the power in pump and probe arms. The fraction of molecules excited in the focal volume (as measured by depletion of the $C_2H_4^+$ signal) was varied between 3 and 9%. A small constant background ion signal due to multiphoton ionization from the pump arm alone was recorded and subtracted off. I also performed measurements where I replaced the Sn foil with an oxidized Al foil to shift the XUV probe photon spectrum to higher photon energies. The shape of the time resolved photo-ion signals reported here was found to be independent of the excitation fraction and the metallic foil used in the XUV probe arm.

To estimate the time resolution for the 5th harmonic pump/XUV probe configuration, I performed a complimentary experiment on the H_2O molecule. Water vapor was introduced at focus with the solenoid valve discussed in section 3.1. Upon excitation to the $\tilde{A}^1B_1$ state with 160 nm light, the H_2O molecule rapidly dissociates to OH + H along a purely repulsive potential [109]. The step-like increase of the OH^+ signal shown in figure 4.6 is observed as the molecule dissociates. I assume this very fast reaction to occur within the time resolution of the instrument and fit it with an error function to give an upper limit for the finite instrument response of 44^{+15}_{-10} fs FWHM (convolution of pump and probe).

Time resolved photo-ion yields for C_2H_4 target gas are shown versus pump-probe delay t in figures 4.7-4.9. Through photoionization, the XUV probe projects the wavefunction of the excited ethylene molecule onto the manifold of states of the cation and their

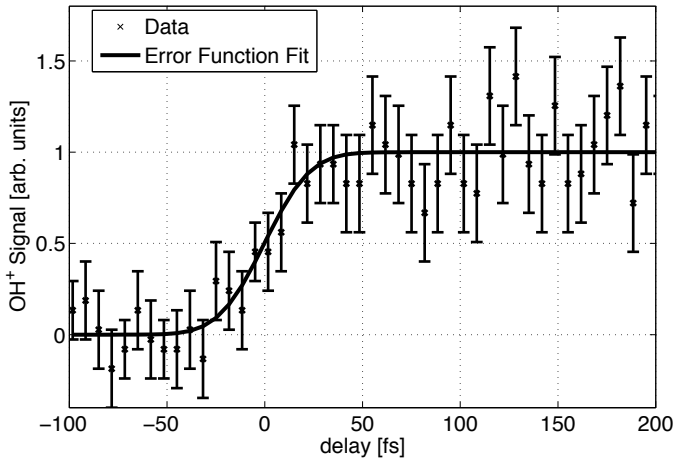

Figure 4.6: **Dissociation of Water.** Calibration of the 7.7 eV pump/XUV probe instrument response. The time resolved OH^+ yield from H_2O molecules excited to the $\tilde{A}^1B_1$ state with the fifth harmonic pump is shown along with an error function fit. The fit corresponds to a Gaussian FIR with a FWHM of 44^{+15}_{-10} fs. The error in the time zero is ± 10 fs. Positive delay corresponds the 7.7 eV pump pulse arriving first.

asymptotes. As in the 7.7 eV pump/7.7 eV probe data, the $C_2H_4^+$ signal rapidly decays as the nuclear wavefunction moves away from the Franck-Condon Region and its overlap with bound states of the cation becomes negligible. The XUV probe is sufficiently energetic to break the C-C bond of the ion through ionization of the σ-like inner valence orbitals ($2a_g$ and $2b_{1u}$) [77], resulting in symmetric breakup (CH_2 + CH_2^+) or asymmetric breakup (CH + CH_3^+) of the ion. For short times comparable to the V state lifetime, there is a transient increase of the CH_2^+ yield peaking at $t \approx 40$ fs. The peak in the CH_2^+ signal then decays giving rise to a peak in the CH_3^+ yield at $t \approx 80$ fs which slowly decays as the molecule dissociates. The magnitude of the observed effects on the partial photoionization cross sections are of order $\Delta\sigma_i/\sigma_i \approx 100\%$. Because the time dependence of the CH_2^+ and CH_3^+ signals are not the same, the signals cannot be assigned to an increased probability for ionization of the inner valence shells alone; the nuclear wave function of the excited neutral must play a role. Indeed, a large increase in the asymmetric breakup is expected if the molecule is ionized from an asymetric (CH_3CH) structure of the neutral. For these reasons, I assign the transient increase in the CH_3^+ yield to ionization of the molecule as it rearranges to the ethylidene structure.

On longer time scales, the molecular hydrogen elimination from the ground state PES is observed. The probe photon energies are higher than the ionization potential of H_2 and are sufficient to directly photo-ionize the H_2 molecule. The H_2^+ signal is shown in figure 4.8. I assign this signal to the ionization of H_2 molecules during and following the dissociation process based on the following facts: (1) Within the statistical error, the signal is monotonically increasing. (2) The production of H_2^+ fragments from the ionization

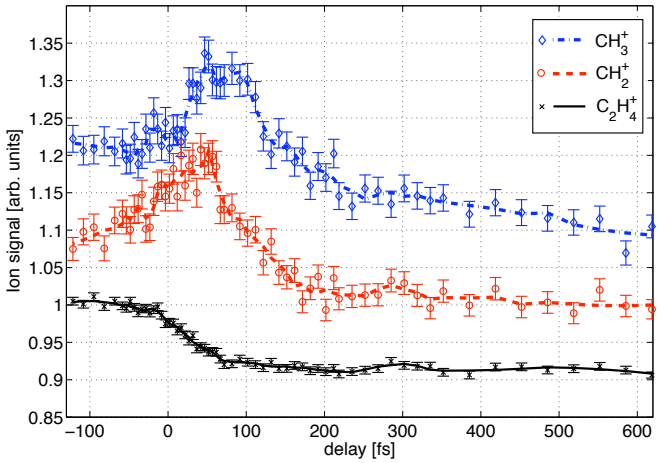

Figure 4.7: **Hydrogen Migration.** Time resolved photo-ion yield from 7.7 eV pump/XUV probe experiments. The parent ion $C_2H_4^+$ (black x's) decays as the system moves away from the Franck-Condon region. At short times, an increase in the symmetric breakup (CH_2^+ + CH_2, red circles) is observed upon dissociative photoionization, due to the electronic and vibrational excitation of the molecule. At longer times, the asymmetric breakup (CH_3^+ + CH, blue diamonds) is observed as the molecule rearranges to an ethylidene (CH_3CH) configuration. The lines are adjacent point smoothed. Positive delay corresponds to the 7.7 eV pump pulse arriving first.

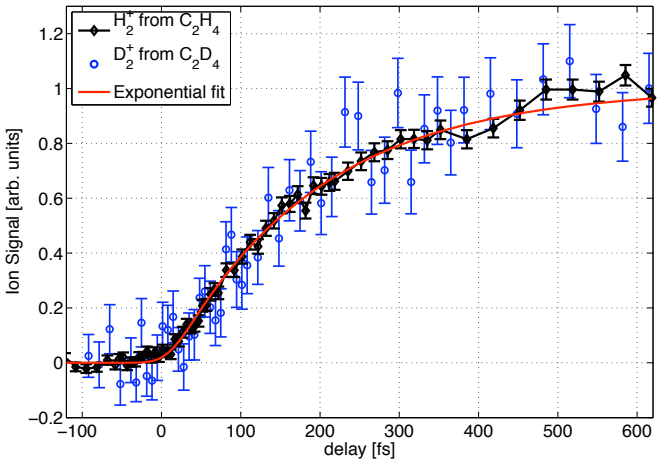

Figure 4.8: **Hydrogen Molecule Elimination.** Time resolved photo-ion yield from 7.7 eV pump/XUV probe experiments. The H_2^+ (black diamonds) signal from C_2H_4 and the D_2^+ (blue circles) signal from C_2D_4 rise on the same time scale. The solid red curve is an exponential fit with time constant 184 fs.

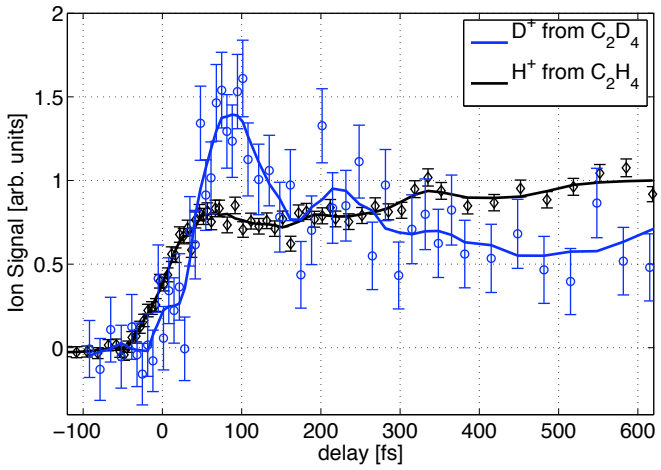

Figure 4.9: **H^+ and D^+ signals.** Time resolved photo-ion yield from 7.7 eV pump/XUV probe experiments. The H^+ (black diamonds) and D^+ (blue circles) signals from C_2H_4 and C_2D_4 both show a peak at early times after excitation. The signals are rescaled using the simultaneously measured H_2^+ and D_2^+ at long delay and the measured ratio of H_2 to D_2 dissociation products from ref. [101]. Solid curves are adjacent point smoothed.

of C_2H_4 is observed to be extremely small below the double ionization theshhold [77]. (3) The H_2^+ ion count rate is in reasonable agreement with what would be estimated from the observed excitation fraction, the measured branching ratios [101], the photoionization cross section of H_2, and the mass spectrometer collection efficiency (see section 4.5.3 for details). To estimate a time scale for the dissociation, I fit the rise in the H_2^+ signal to a single exponential, and obtain a time constant $\tau_D = 184 \pm 5$ fs. The fit, shown as the solid red curve in figure 4.8, agrees very well with the data out to delays of 350 fs. However, for longer delays, the H_2^+ signal diverges from the simple exponential behavior. Also shown is the D_2^+ signal from from C_2D_4 (blue circles in figure 4.8), which rises with the same time scale.

As discussed above, the vibrationally hot ground state can also dissociate by eliminating hydrogen atoms, and a large increase in the H^+ signal is also observed. Figure 4.9 shows the H^+ and D^+ signals recorded from C_2H_4 and C_2D_4. However, the interpretation of the H^+ signal is less clear because for the H^+ signal conditions (1) and (2) above are not met. Instead of increasing monotonically, both signals show a peak within 100 fs after excitation. Significant H^+ and D^+ signals are also observed upon ionization of unexcited ethylene with the probe photon energy band [77]. A component of the H^+ and D^+ signal increases are expected to come from the ionization of excited ethylene near time zero [77], and vibrationally hot acetylene molecules [110] at later times after dissociation. Indeed, I also observed increases in the fragments CH^+ and C^+ that persist to long delay, which are likely due to the ionization of vibrationally hot acetylene molecules. The CH^+ and C^+ signals are not shown because the shape of the signals was found to depend on the

excitation fraction and the metallic filter used in the probe arm. Also not shown are the deuterated versions of the signals in figure 4.7. Due to the limited quantity of C_2D_4 that was available for running the experiment, the acquisition time with C_2D_4 was extremely limited, and the signal to noise of the CD_2^+, CD_3^+ and $C_2D_4^+$ was insufficient to make a meaningful comparison to the data of figure 4.7.

4.5 Discussion

Multiple time scales are observed in the data of figures 4.5-4.9. This is expected from the predicted multi-surface dynamics and the studies of the asymptotes discussed in section 4.1. I will now make some comparisons between the observed time constants and previous work.

4.5.1 The Excited State Lifetime

The very fast time constants for the excited state lifetime extracted from the MPI probe studies, surprisingly, agree with those measured in the present work with single 7.7 eV photon ionization. The many theoretical calculations [16, 95, 96, 97], however, consistently predict a longer life-time for the V state in the range of 90 to 180 fs. Previously, the discrepancy between theory and experiment was rationalized [16, 97] on the basis of the multiphoton probe studies being limited by an energy detection window. In other words, the short time constants measured by the multiphoton probe experiments were presumed to be mainly a measurement of the residence time of the system in the Franck-Condon region, where the V-state potential energy is high and the number of photons required to ionize the molecule is lowest. As the system moves downward on the sloped V-state potential, the gap in the electronic energy between the V-state and the ground state of the ion increases and the order of the MPI process increases, reducing the ion signal amplitude on a time scale shorter than the V-state lifetime. The 7.7 eV probe photon energy used for the data of figure 4.5, however, should be sufficient to ionize the molecule via single photon absorption for the entire time the dynamics proceed on the V-state PES [97].

Resolving the source of this discrepancy between theory and experiment is of fundamental importance if the predictions of the theoretical techniques are to be trusted with larger molecules. One possible source of error is the accuracy of the potential energy surfaces used as input to the dynamical models. In general, when a molecule absorbs a photon, the nuclear wavepacket launched on the excited PES is started from from equilibrium. This means that a large area of the excited PES is energetically accessible, and the excited PES must then be calculated over a large volume of the nuclear coordinate phase space. Even for a molecule as small as ethylene, accuracy in the electron structure calculation must be balanced against speed, and the sophistication of the method used to calculate the electronic structure is somewhat limited. For more than ten years now, the group of T. J. Matrinez has conducted a series of calculations on the photodynamics of ethylene using the Ab Initio Multiple Spawning (AIMS) technique with various inputs for the electronic structure. The trend is that as the accuracy of the electronic structure calculation increases, the calculated excited state lifetime gets shorter [96].

Another possibility is that the time constants measured in the 7.7 eV probe data

correspond to the vanishing of the photoionization dipole matrix elements, and not the excited state lifetime. If this were the case, it is then odd that the 7.7 eV probe and MPI signals vanish on the same time scale, as the photoionization matrix elements are very different in the two cases. However, both measurements will share a similar Franck-Condon factor for the probe step (see section 1.2), and it is possible that the decay of the photo-ion signals is due to the decay of the overlap integral between the nuclear wave function on the V-state surface and that on the cation surfaces populated after photoionization. This is likely the dominant source of the decay of the bound $C_2H_4^+$ signal; as the nuclei move away from the point of vertical excitation on the V-state surface, the overlap between the nuclear wave function and that of the bound states of the cation becomes negligible. However, for the $C_2H_3^+$ and $C_2H_2^+$ signals, products of dissociation in the cation, the nuclear wave functions form a continuum. Furthermore, the transition states predicted in the dissociation of the low-lying states of the cation [111, 112] are similar to those predicted for the non-adiabatic decay of the V-state, so the Franck-Condon overlap should be non-zero near the MECIs.

The assignment of the short decay time of the $C_2H_3^+$ and $C_2H_2^+$ signals in the 7.7 eV probe to the lifetime of the electronic excitation is further reinforced by two features of the XUV probe data. First, the decay of the $C_2H_4^+$ ion yield in figure 4.7 is slightly slower than in the 7.7 eV probe data. If I fit this signal with an exponential decay convolved with the 44 fs FIR, I get a decay constant of 32 fs, compared to the 21 fs decay observed in the 7.7 eV probe data. This could indicate that the decay of the $C_2H_4^+$ signal in the 7.7 eV probe data is not completely due to the decay of the Frank-Condon factor, and is partially due to the decay of the excited electronic state. Second, the monotonic increase of the H_2^+ signal begins very shortly after time zero. If the H_2 elimination occurs from the ground state surface, as is the conventional wisdom [100, 113], the nuclear wave function is indeed making it to the ground state surface quickly.

4.5.2 Ethylidene

In section 4.4, the increase in the CH_3^+ signal between 50 and 100 fs was assigned to hydrogen migration based on its independence from the CH_2^+ signal and the fact that an increase in the asymmetric breakup of the ion is expected for ionization of an asymmetric molecule. Several claculations have been published showing the time scale for hydrogen migration and theory is in better agreement with the observed signal here than for the excited state lifetime. In a series of semi-empirical molecular dynamics simulations [97, 98, 94], Barbatti et. al. find significant population reaching hydrogen migrated geometries between 60 and 100 fs. Using the Ab initio multiple spawning (AIMS) method, Tao et. al. [96] show trajectories in which hydrogens traverse the double bond at $t \approx 100$ fs. Also using the AIMS method, Levine et. al. [114] show the population on the V-state PES at twist angles around 90° and high pyramidalization angles greater than 120° peaking between 50 and 100 fs. A high pyramidilization angle indicates hydrogen migration across the double bond (see figure 4.3).

Although the ethylidene structure is predicted to be a pathway for electronic relaxation of the molecule, the persistence of the CH_3^+ signal to times much longer than the excited state lifetime does not present an inconsistency with this assignment. The

molecule can persist in the ethylidene configuration even after the system has relaxed to the ground state PES. Furthermore, the calculations predict that the main path for electronic relaxation is through the twisted/pyramidilized structure, and thus measurements of the electronic excitation lifetime will be biased towards this pathway [96, 98].

4.5.3 Hydrogen Molecule Elimination

The non-adiabatic transfer of population through a conical intersection is not expected to occur at the MECI alone, but in an extended region around the MECI where the energy gap between the two electronic states is small [96]. This explains why the signals in figure 4.5 exhibit a smooth decay, as opposed to an abrupt cutoff at a certain delay when the wavepacket reaches the MECI. The transfer of the nuclear wave function from one surface to another is then disorderly. An analogy can be made to a skier hitting a tree: when a skier hits a tree the wave function of him and his equipment is dispersed over a large area on the ski slope below. In the case of ethylene, with 6 atoms and 12 internal degrees of freedom, one might then expect that the 180 kcal/mol of excitation energy could be redistributed in a nearly statistical, or Boltzmann-like fashion in the vibrationaly hot ground state. Indeed, some features of the kinetic and internal energy distributions of the H_2 photoproduct appear statistical, while others do not. Cromwell et. al. [115] measured the rovibrational state distribution of H_2 molecules from photolysis of ethylene at 193 nm and find a good agreement between the vibrational state distribution and a Boltzmann distribution with $T = 5000$ K. The rotational state distribution, however, is nonstatistical and shows features indicative of the multiple hydrogen elimination channels. Chang et. al. calculated the dissociation branching ratios and kinetic energy distributions of the H and H_2 dissociation products in the context of a statistical model [113, 116] using ab initio calculations of the ground state PES as input. The Branching ratios were calculated with the Rice-Ramsperger-Kassel-Marcus (RRKM) transition state theory. The kinetic energy distributions were calculated assuming a statistical redistribution of the above-barrier energy into the vibrational modes of the system at the transition state. Energy in the stretching modes was assigned to the translational kinetic energy release of the dissociation. The model achieves qualitative agreement with experiment [100], but significant discrepancies appear upon close comparison of both the measured branching ratios [101] and kinetic energy distributions [100].

The RRKM model of Chang et. al. [113] also predicts time constants for the molecular hydrogen elimination of roughly 1 ps - much longer than the 184 fs time constant observed here. The present work then indicates that H_2 elimination proceeds directly, in a nonstatistical fashion. This is supported by observation of the same rate for elimination of D_2 from C_2D_4. If the molecular elimination were the result of tunneling through a potential barrier at the transition state, the tunneling rate [14] would take the form

$$k \sim \exp\left(-\frac{1}{\hbar}\int dx\,|p(x)|\right) \tag{4.2}$$

where $p(x)$ is the momentum of the system as it traverses the barrier. If the system has an energy E along the H_2 - C_2H_2 coordinate, the momentum is then $p \sim \sqrt{2ME}$, and the tunneling rate would be exponentially sensitive to the reduced mass M. The lack of a mass

effect on the molecular elimination indicates that the dissociation rate is not dominated by tunneling through a potential barrier.

It is unknown, of course, if there are further dynamics on longer time scales than the maximum delay of 620 fs measured here. It is possible that the RRKM theory becomes more appropriate at longer delays after the vibrational energy has more time to distribute throughout the normal modes of the system. The maximum delay of 620 fs was limited by the travel of the piezo-electric delay stage driving the HOA mirror (see chapter 3). In one of the MPI probe studies discussed above, Kosma et. al. [91] did observe a long lived ($\tau \approx 5$ ps) tail in the $C_2H_3^+$ and $C_2H_2^+$ signals. However, the MPI signal level after delays longer than 500 fs is less than 10^{-3} of the peak value, making the assignment of the tail problematic. It could, for example, be due to one of the Rydberg states which spectrally overlaps the V-state in the VUV absorption spectrum, or it could be due to 10^{-3} residual population of the V-state remaining.

In the present work, the H_2^+ signal at long delays is large and unambiguous. One can attempt to determine the completeness of the dynamics within 620 fs by comparing the measured increase in the H_2^+ count rate to what would be expected from the known asymptotes. I will attempt a rough estimate of the expected asymptotic H_2^+ count rate in the SMI apparatus here. The increase in the mean H_2^+ ion rate $\Delta\mu_{H_2^+}$ is given by

$$\Delta\mu_{H_2^+} = \int d^3\mathbf{r}\,[\eta(\mathbf{r})F_\gamma\rho\mathrm{DE}]\,\sigma_{H_2}\beta_{H_2}\int dT P_{H_2}(T)\mathrm{CE}(\mathbf{r},\mathrm{T}) \tag{4.3}$$

where $\eta(\mathbf{r})$ is the position dependent excitation fraction of the C_2H_4 target gas, F_γ is the XUV probe photon fluence, ρ is the target gas density, DE is the ion detector efficiency, σ_{H_2} is the XUV photoionization cross section of H_2, β_{H_2} is the percentage of excited C_2H_4 molecules that dissociate via H_2 elimination, $P_{H_2}(T)$ is the kinetic energy distribution of the H_2 photoproduct, and CE($\mathbf{r}$,T) is the collection efficiency for an ion born at position $\mathbf{r}$ with kinetic energy T (see section 3.1.1). The first integral runs over three dimensional space in the vicinity of the SMI focus and ion extraction pinhole. The second integral runs over the kinetic energy of the H_2 molecules. The angular distributions for H_2 and D_2 molecules photo-dissociated from C_2H_4 and C_2D_4 are observed to be nearly isotropic [117], so more integrals over the angles of emission of the molecules are not necessary. Assuming every C_2H_4 molecule that absorbs a 7.7 eV pump can no longer be ionized to bound states of $C_2H_4^+$ at long delays, a large chunk of equation (4.3) also appears in the expression for the change in the $C_2H_4^+$ ion rate.

$$\Delta\mu_{C_2H_4^+} = -\int d^3\mathbf{r}\,[\eta(\mathbf{r})F_\gamma\rho\mathrm{DE}]\,\sigma_{C_2H_4} \tag{4.4}$$

The expression for the $\Delta\mu_{C_2H_4^+}$ does not contain the integral over the initial kinetic energy T, because there is no kinetic energy release in the reaction $C_2H_4 + h\nu \rightarrow C_2H_4^+$, and all the $C_2H_4^+$ ions from the focus are collected with high efficiency. If spatial dependence of the collection efficiency is neglected, we can approximate CE($\mathbf{r}$,T) $\approx$ CE($\mathbf{r}_0$,T), where $\mathbf{r}_0$ is a point directly above the center of the extraction pinhole. Equation (4.4) can then be used to rewrite equation (4.3):

$$\Delta\mu_{H_2^+} = -\Delta\mu_{C_2H_4^+}\frac{\sigma_{H_2}}{\sigma_{C_2H_4}}\beta_{H_2}\int dT P_{H_2}(T)\mathrm{CE}(\mathbf{r}_0,\mathrm{T}) \tag{4.5}$$

The $C_2H_4^+$ signal in figure 4.7 is reduced by $\Delta\mu_{C_2H_4^+}/\mu_{C_2H_4^+} = 9\%$ by the pump pulse. The absolute ion rate at negative delays for $C_2H_4^+$ is estimated to be 83 ions per shot from the CH_3^+ yield of 0.28 ions/shot and the branching ratios of Ibuki et. al. [77]. The change in the $C_2H_4^+$ count rate is then $\Delta\mu_{C_2H_4^+} = -0.09 \times 83 = -7.5$ ions/shot. I numerically performed the integral over T using the $CE(\mathbf{r}_0, T)$ from equation (3.7) and the H_2 kinetic energy distribution from ref. [100]. The result is that 60% of the H_2^+ ions should make it through the extraction hole. The branching ratio for H_2 production from photolysis of C_2H_4 is 46 % [101]. Inserting these numbers and the photoionization cross sections for $H_2 + h\nu \rightarrow H_2^+$ and $C_2H_4 + h\nu \rightarrow C_2H_4^+$ into equation (4.5) gives an expected count rate of 0.9 ions/shot for $\Delta\mu_{H_2^+}$. The value recorded in the experiment at 620 fs delay was 0.35 ions/shot.

The above calculation certainly overestimates the expected H_2^+ count rate because of the approximation CE($\mathbf{r}$,T) $\approx$ CE($\mathbf{r}_0$,T). Inspection of figure 3.4 shows that ions born away from $\mathbf{r}_0$ will have a lower collection efficiency. I estimate the 5th harmonic to have a confocal parameter $2z_R$ of roughly 200 μm from scans of the the extraction pinhole in the longitudinal direction, indicating that the spatial integration over the SMI focal volume is not negligible. The precision with which the extraction hole was centered on the SMI focus is also not known. Misalignment of the extraction hole would also reduce the H_2^+ collection efficiency. Considering these uncertainties, the agreement between the above calculation and the measurement is reasonable. While it cannot be concluded that the hydrogen elimination is complete, the above analysis indicates that a large fraction of the H_2 elimination occurs within the 620 fs observation window of the present work, and that this fraction is nonstatistical in nature. Further insight into the molecular elimination dynamics can be gained by conducting the time resolved experiment on di-deuterated isoptomer targets (e.g. $C_2H_2D_2$) as has been done extensively in the studies of the asymptotes to observe the multiple molecular elimination channels illustrated in figure 4.4.

4.5.4 H^+ and D^+ Signals

The fastest feature in the XUV probe data is the rise of the H^+ signal in figure 4.9. The $\sim$ 50 fs rise time is presumed to be limited by the finite instrument response of the apparatus. The H^+ signal also rises earlier than the observed decay of the $C_2H_4^+$ signal, indicating that at short times after excitation, the H^+ yield is enhanced by the electronic excitation of the molecule alone, before the nuclei have moved. A possible source of this increased H^+ yield is inner valence ionization of valence excited ethylene. A satellite in the photoelectron spectrum with large oscillator strength has been seen at 27.4 eV excitation energy [118]. A configuration interaction study [118] identifies the leading configurations responsible for the satellite as being inner valence ionized and valence excited: $(2b_u^1)^{-1}(\pi\pi^*)$ and $(2b_u^1)^{-1}(\pi^*\pi^*)$. This means that ionization of the σ-like $(2b_u^1)$ inner valence orbital is energetically possible with the probe photons from the V and Z states of the neutral. Unfortunately, the subsequent dissociation of the satellite state has not been studied with coincidence techniques to determine the H^+ yield. However, Ibuki et. al. [77] did observe an increase in the H^+ yield as the photon energy is swept through the satellite threshold. More work is needed to conclusively determine the reason for the increased H^+ yield from

the photoionization of valence excited ethylene observed here.

The fact that the H^+ signal is *not* monotonic indicates that the signal cannot be interpreted as being cleanly due to the ionization of dissociated H atoms alone, as was done in the H_2^+ case. Interpreting the H^+ yield at longer delays is difficult because of the several potential sources of H^+. Whereas the production of H_2^+ signal from the photoionization of the acetylene dissociation product is expected to be negligible based on previous photoionization studies of acetylene [110, 119], the production of H^+ is not, especially considering the large vibrational energy left in the C_2H_2 molecule after H_2 elimination. Indeed, if the absolute H^+ count rate is analyzed in a similar manner to what was done for H_2^+ in the previous section, the measured H^+ signal is found to be larger than expected. Furthermore, while the overall shape of the H^+ signal level in different experimental runs was approximately the same, the ratio of the effect on the H^+ count rate at long delays to that of the other ion fragments was found to vary with the excitation fraction and the metallic filter in the probe arm. More work is needed to separate the different channels contributing to the H^+ signal.

Despite my inability to interpret the H^+ signal, I included it here because of the striking isotope effect shown in figure 4.9. The previous MPI probe studies had found no significant difference in the early dynamics of ethylene and deuterated ethylene, and in the present work, the elimination of H_2 and D_2 from C_2H_4 and C_2D_4 are observed to be the same. This is surprising considering the conventional wisdom that the dynamics are determined by the motions of twist and pyramidilization of the CH_2 groups and hydrogen migration. All of these motions should show a strong isotope effect. Here, although the interpretation is unclear, a strong isotope effect is clearly observed in the dynamics. The peak in the D^+ signal is shifted to later times and is more pronounced.

Chapter 5

VUV Dissociation of Oxygen

We will, in fact, be greeted as liberators.

-Vice President Dick Cheney

It is the VUV absorption of oxygen that is responsible for the "vacuum" in vacuum ultraviolet. The first absorption band of the O_2 molecule starts at $\lambda = 200$ nm and is called the Schumann-Runge Continuum. The VUV absorption and photodissociation of O_2 and O_3 in the Schumann-Runge bands are extremely important for the chemistry of the upper atmosphere. In this chapter, I will describe pump probe-experiments on the photodissociation of O_2 upon excitation at 161 nm.

5.1 Potential Energy Curves

The potential energy curves for the ground state of O_2 ($X\ ^3\Sigma_g^-$) and several excited states in the vicinity of vertical excitation with the pump photon energy are shown in figure 5.1. For 161 nm excitation, the absorption is dominated by excitation of the $B\ ^3\Sigma_u^-$ state [99, 120]. Lin et. al. [121] studied the kinetic energy release distribution of the O atoms upon 157 nm excitation and find that less than 1% of the population of the initial $B\ ^3\Sigma_u^-$ state predissociates along the other excited states shown in figure 5.1 to the O (^3P) + O (^3P) asymptote. Instead, the dissociation mainly proceeds directly along the B-state potential surface to the O (^1D) + O (^3P) asymptote.

Since O_2 is a diatomic molecule with only one internal degree of freedom, the nuclear dynamics upon excitation of the $B\ ^3\Sigma_u^-$ state are amenable to simulation via numerical solution of the time dependent Schrödinger equation. I performed calculations using the Crank-Nicholson finite difference method described in [122]. The results are shown in figure 5.2. Potential energy curve data was taken from the configuration interaction calculations of Saxon [123], rescaled and shifted to match experimental measurements for the potential minimum and the energy difference between O (^3P) and O (^1D) at the asymptote. The initial nuclear wave function was taken to be the ground vibrational state of the electronic ground state of oxygen, in the approximation of a harmonic potential:

$$\chi(R,0) = \exp\left(-\frac{M\omega_0}{2\hbar}(R-R_0)^2\right) \tag{5.1}$$

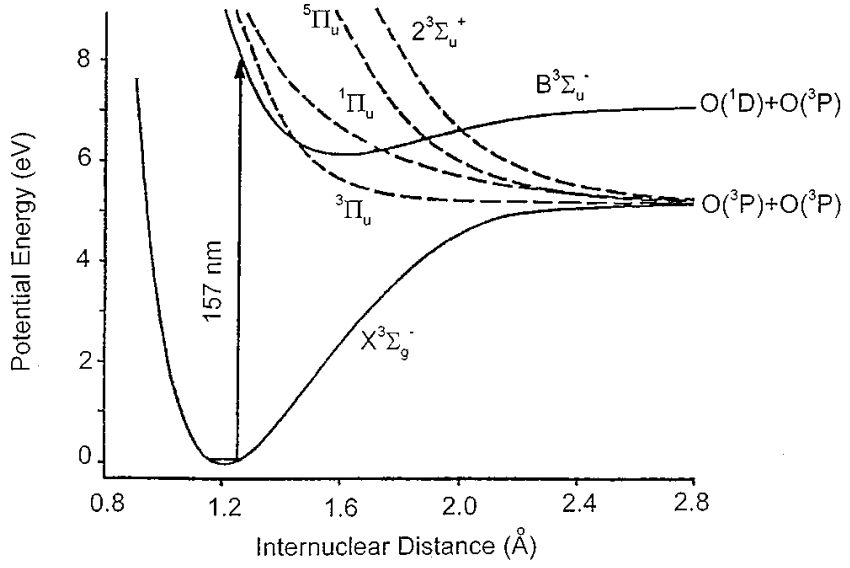

Figure 5.1: **O_2 Neutral Potential Energy Curves.** Potential energy curves for the ground state ($X^3\Sigma_g^-$) and several excited states in the vicinity of the pump photon energy. From ref. [121].

where $M = 8$ Daltons is the reduced mass for O_2, $\omega_0 = 1580$ cm^{-1} is the natural frequency of vibrations in the ground electronic state, and $R_0 = 1.21$ Å is the equilibrium distance of O_2 in its ground state [123]. Note that projection onto the nuclear basis functions of the B-state through the Franck-Condon factors has been neglected here. The time step for the simulations was Δt =2 atomic units (48 attoseconds) and the spacing of the grid used for finite differencing the Shrödinger equation was 0.0025 atomic units (0.0013 Å). At each time step, the wave function is multiplied by a "gobbler" function [124] which tapers to zero at the large R grid boundary of 6.6 Å. The smooth first derivative of the gobbler function eliminates reflection of the wave function from the grid boundary. The 7.7 eV photon energy excites the system 0.63 eV above the O (^1D) + O (^3P) asymptote. The simulations show the molecule directly dissociating with no appreciable portion of the wave function getting trapped in the potential well of the B-state curve.

5.2 7.7 eV pump/29.2 eV probe results

Figure 5.3 shows the results of fifth harmonic (7.7 eV) pump/19th harmonic (29.2 eV) probe experiments. The 19th harmonic was selected in the HOA with a 0.16 μm thick aluminum filter and a Mg/Si:C multilayer coating on the HOA mirror. The fifth harmonic was isolated for the pump with a dichroic mirror (Layertech gmbh) and a 230 μm CaF_2 window. The mirror/filter arrangement is depicted in figure 3.2 of chapter 3. The harmonics were generated with a gas cell feedline pressure of 3.2 Torr Krypton.

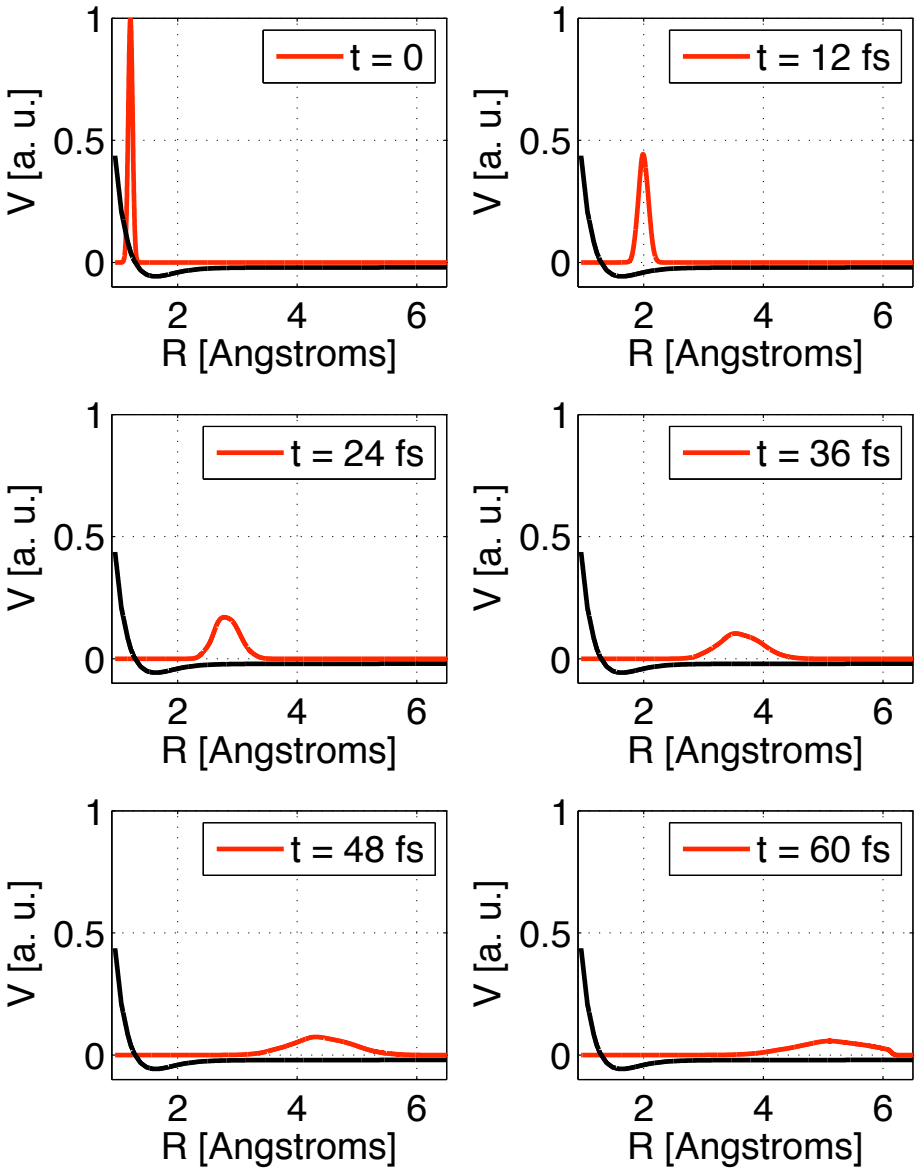

Figure 5.2: **Numerical Simulations of O_2 Photodissociation.** The oxygen molecule directly dissociates along the B-state potential energy surface. The square modulus of the nuclear wave function is plotted in red at 12 fs increments. The potential energy curve of the $B\ ^3\Sigma_u^-$ state is plotted black. The ground vibrational state of O_2 in its electronic ground state was taken as the initial wave function.

The fall time of the O_2^+ signal is observed to be extremely fast. Indeed this is expected as the HOMO $1\pi_g$ orbital of the ground state of O_2 is actually an antibonding orbital. The equilibrium internuclear distance is actually 0.1 Å shorter in the ground state of O_2^+ than O_2 and the bond energy is 1.6 eV stronger. The delay window over which the probe efficiently brings the system to the first few states of O_2^+ is then very small. Higher excited states of O_2^+ with larger equilibrium distance have been observed to predissociate, leading to O + O^+ [125]. The very short time window for photoionization to bound states of O_2^+ from the $B\ ^3\Sigma_u^-$ state was also observed by Conde et. al. [107] with 7.7 eV probe pulses.

Assuming the drop in the O_2^+ yield to be limited by the finite time resolution of the apparatus, the error function fit in figure 5.3 corresponds to a Gaussian finite instrument response function (FIR) with a FWHM of 13±9 fs. The confidence interval here is the 67% confidence interval of the error function fit. However, the width of the FIR is further constrained to be greater than 13 fs by the measured bandwidth of the 5th harmonic under the Kr HHG conditions and equation (1.14). The O_2^+ signal then indicates a fifth harmonic pulse width near the transform limit after the 230 μm CaF_2 window and 3.2 Torr Kr HHG. The width of the FIR is then more accurately represented as 13^{+9}_{-0} fs. For comparison, the width of the FIR in the 7.7 eV pump/7.7 eV probe measurements in chapter 4, where the harmonics were generated with 8 Torr Ar feedline pressure, was measured to be 25 ± 7 fs, indicating a fifth harmonic pulse width of 18 ± 5 fs after division by $\sqrt{2}$. The fifth harmonic pulse width is expected to dominate the width of the FIR in the 5th harmonic/19th harmonic cross correlation because of the narrow ionization gate on the phase matching of the 19th harmonic (see chapter 2).

At long delays, the two oxygen atoms are separated by a large distance and the photoionization of the system must be that of two oxygen atoms. The cross section for O^+ production is increased. The O^+ signal in figure 5.3 rises to its long delay value in 50 fs.

5.3 Discussion

In the present work, the partial cross section for $h\nu$+ $O_2 \rightarrow$ O + O^+ of the dissociating O_2 molecule is observed to be atom-like within 50 fs after excitation of the $B\ ^3\Sigma_u^-$ state. It is then tempting to call 50 fs the "dissociation time" of the molecule. The status of the molecule in the numerical simulations is clear. At 50 fs delay, the center of the wave packet is at R = 4.45 Å, and the probability for finding the system at $R < 3$ Å is 0.0014. As this internuclear distance is more than three times larger than the equilibrium internuclear distance in O_2 of 1.21 Å, and the potential curves for states of the neutral and singly ionized molecule appear flat viewed on a linear scale for separations of $R > 3.5$ Å [126], this seems like a reasonable assignment. Indeed, in chapter 4, I assigned the monotonic H_2^+ signal increase to H_2 molecules eliminated from C_2H_4 based on the correspondence between the measured H_2^+ signal and that expected from the depletion of the $C_2H_4^+$ signal and the photoionization cross section of H_2.

However, of course the two oxygen atoms will remember the chemical bond from which they came for all times, and the atomic wave functions will always show some alignment along the molecular axis. In this sense, the chemical bond is never really broken.

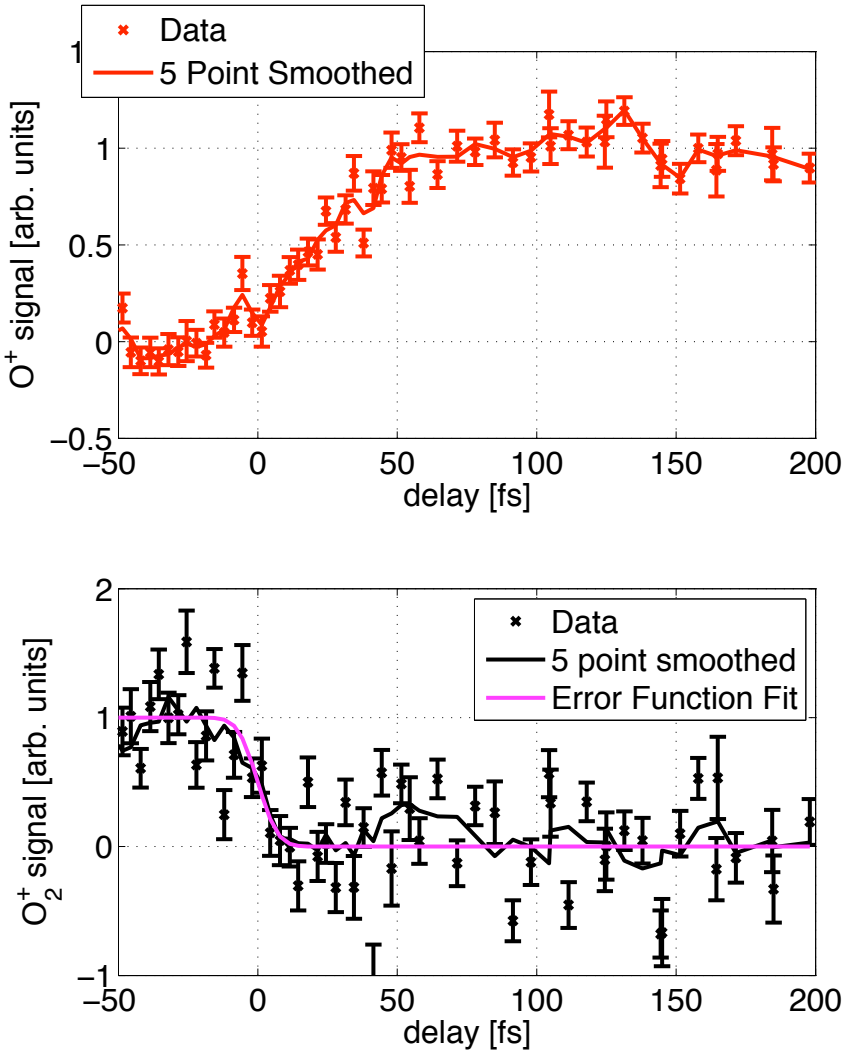

Figure 5.3: **Time Resolved Photoionization of Dissociating O_2.** Results of 7.7 eV pump/29.2 eV probe experiments. The O_2^+ signal is fit with an error function. The fit corresponds to a Gaussian finite instrument response with FWHM of 13 fs. The O^+ signal rises to its long delay value within 50 fs.

Detailed studies of Br_2 molecules during a direct photodissociation process similar to that studied here in O_2 [127, 128, 129, 130] indicate that the exact "dissociation time" depends on exactly what you measure. For example, Nugent-Glandorf et. al. [128] and Strasser et. al. [129] prepared the Br_2 molecule in the dissociative $^1\Pi_u$ state and recorded photoelectron spectra with time delayed XUV pulses. They observe the appearance of atomic photoelectron lines to be shifted by 40 fs from time zero, indicating a dissociation time of 40 fs [128, 129]. This delay corresponds to an internuclear distance of $R_d \sim 3$ Å or 1.4 times the equilibrium internuclear distance of $R_e = 2.2$ Å of Br_2 [128]. In a similar XUV photoionization study with a complicated background subtraction technique, Wernet et. al. [127] extract a dissociation time of 80 fs, or $R_d = 3.8$ Å $= 1.7R_e$. Yet in a study using strong field ionization as the probe, Li et. al. [130] observe molecule-like features in the kinetic energy of Br^+ fragments extending out to delays of 140 fs, or internuclear distances of 5 Å $= 2.3R_e$.

Chapter 6

Conclusions and Outlook

Mission Accomplished

- Banner over President George W. Bush during a televised address aboard the USS Abraham Lincoln.

The present work establishes techniques for performing femtosecond spectroscopy with vacuum ultraviolet and extreme ultraviolet pulses. The HHG results of chapter 2 demonstrate the scaling of high order harmonic generation to peak powers sufficient to simultaneously provide pump and probe pulses in the VUV/XUV. I estimate that it was possible to ionize up to 3% of the molecules at focus with the 17-23 eV probe pulses used in the ethylene experiments, indicating that the pump wavelength was not restricted to the intense fifth harmonic. Indeed, a small $C_2H_3^{2+}$ peak is observable in ion mass spectra at the highest probe intensities used, which is likely due to sequential ionization from the probe arm.

The split mirror interferometer provides a stable and robust platform for delay and recombination of wavelengths for which conventional optical technology is lacking. The mechanical stability of the design presented here was remarkable: Over roughly a two month period the spatial overlap was checked before every experimental run using strong field ionization with the 800 nm laser (see chapter 3), and the overlap appeared at the same readings of the LVDT tip/tilt sensors for the entire period. The maximum delay was limited to 620 fs by the travel of piezo-electric delay stage driving the HOA mirror and the requirement that the time-zeros with and without the CaF_2 window lie within the travel of the stage. However, even with a stage with longer travel, because moving the HOA mirror changes the relative longitudinal position of the SMI foci, the SMI in the current apparatus will run into problems for delay path lengths ct much larger than the Rayleigh ranges of the focused harmonics [73]. This could be mitigated by implementing the split and delay at the Si mirror, although the alignment procedure would then be more complex.

The time resolution of the apparatus was observed to depend on the harmonics used, the way they were generated, and the filters used between the Si mirror and the SMI. However, in all cases, the harmonic pulses were significantly shorter than the 50 fs, 800 nm pulse used to generate the harmonics. As the calibration of the finite instrument response was often more difficult than the pump-probe experiment of scientific interest, a

HHG	Pump (LOA)	Probe (HOA)	FWHM	Method
Argon 8.0 Torr	Fifth Harmonic ~ 200 μm MgF_2 UV enhanced Al mirror	Fifth Harmonic ~ 200 μm MgF_2 Mg/Si:C Multilayer	25 ± 7 fs	MPI of H_2O
Xenon 2.4 Torr	Fifth Harmonic ~ 200 μm MgF_2 Dielectric Stack	Fifth Harmonic ~ 200 μm MgF_2 B_4C 30 nm	43^{+7}_{-5} fs	MPI of O_2
Xenon 2.4 Torr	Fifth harmonic 230 μm CaF_2 Dielectric Stack	Harmonics 11-15 0.16 μm Sn filter B_4C 30 nm layer	$< 44^{+15}_{-10}$ fs	Dissociation of H_2O OH^+ increase
Krypton 3.2 Torr	Fifth Harmonic 230 μm CaF_2 Dielectric Stack	19th harmonic 0.16 μm Al filter Mg/Si:C Multilayer	13^{+9}_{-0} fs	Dissociation of O_2 O_2^+ drop

Table 6.1: **Time Resolution.** The FWHM of the finite instrument response measured for various experimental conditions. MPI stands for multiphoton ionization.

systematic study of the harmonic pulse lengths as a function of the experimental conditions was not made. The measured finite instrument response (FIR, convolution of pump and probe) widths for some different experimental conditions are summarized in table 6.1. In all cases, it is expected that the instrument response is dominated by the fifth harmonic pulse width, as the XUV harmonics are expected to be generated efficiently for only a small portion of the driver laser pulse (see chapter 2). The observation of fifth harmonic pulse lengths near the transform limit in the Ar and Kr HHG cases indicates that the ~ 200 μm thickeness of the MgF_2 and CaF_2 windows used here provide the correct amount of GVD to compensate the negative chirp of the fifth harmonic emerging from the gas cell. The fifth harmonic pulses generated in Xenon were observed to be somewhat longer. One possible reason for this is the proximity of Xenon's $5p^6$ ($^1S_0$) $\rightarrow$ $5p^5 6s$ ($^2P_{3/2}$) resonance line at 8.4 eV to the fifth harmonic at 7.7 eV. Although this is still a large detuning by atomic physics standards, it may affect the fifth harmonic generation process and/or chirp the fifth harmonic as it propagates in the Xe background gas over the several meters of optical path length towards the Magnus chamber. I estimate the GVD of the 2.4 Torr, 5 cm long Xe cell to be 4.2 fs^2. This is small compared to the 118 fs^2 of the CaF_2 window, but not completely negligible. Also, significant structure was often observed in the fifth harmonic spectrum from Xe, indicating a less clean pulse structure.

The ability to perform femtosecond spectroscopy with VUV and XUV pulses represents a significant advance in ultrafast science. Many previous experimental studies of non-adiabatic dynamics in molecules have been restricted to larger molecules where the excitation and ionization energies are lower [131]. In the case of the important ethylene molecule, the information available from the previous pump-probe measurements using multiphoton ionization (MPI) to probe the dynamics was insufficient for direct comparison with theory. In addition to being more difficult to interpret, the MPI probe is restricted to measuring the dynamics for the first ~ 50 fs on the excited state surface. Like reading

Lewis Caroll's *Alice in Wonderland* only up until the point where Alice falls down the hole, the MPI probe cannot follow the system through the conical intersection. The story is not over when Alice falls down the hole, it has just begun. The XUV probe pulses allow the dynamics to be followed for longer times to the ground state potential energy surface and its asymptotes. In the case of ethylene, this allowed measurement of the time scale hydrogen migration and the H_2 elimination rate. The observed rates are important quantities for constraining theories of non-adiabatic dynamics in molecules. Furthermore, since the pump-probe signal is produced by single photon absorption from the pump and probe only, it may be possible for theory to "simulate the experiment" and allow a direct comparison [106] between theory and experiment. It is essential that a good agreement between theory and experiment be made for ethylene, the simplest molecule with a carbon double bond, if the field is to progress to a complete understanding of the non-adiabatic dynamics of more complex systems.

As all molecules absorb in the VUV and XUV, the techniques presented here can be applied to study the dynamics of a wide variety of systems. For example, the fifth harmonic could excite the Rydberg states of many molecules, or one could use the 7th harmonic to pump a molecule to the lowest PES of the cation. Undoubtedly, the methods described in this thesis will be built upon and improved with advances in laser technology. I will describe some future directions in the following sections

6.1 Photoelectron Angular Distributions

The measurement of total ion fragment yield used in this work was relatively simple to implement experimentally. Ions can be extracted from the focal volume with a strong electric field and go where you tell them to. However, by today's charge particle detection standards, the measurement of total ion fragment yield is extremely crude. Much more information can be obtained from the photoionization process if more of its details are measured. Consider for example, the dynamics of the oxygen molecule considered in chapter 5. The 29.2 eV probe projects the wave-packet on the $^3\Sigma_u^-$ potential energy curve onto the many states of the ion. Some of these states lead to dissociated ion fragments O and O^+ and some remain bound as O_2^+. In the present work, all that is measured are the total cross sections

$$\sigma(O_2^+) : h\nu + O_2^* \rightarrow O_2^+ \tag{6.1}$$

$$\sigma(O^+) : h\nu + O_2^* \rightarrow O + O^+ \tag{6.2}$$

Each of these cross sections represents the sum of many partial cross sections for populating different states of the ion and the photoelectron. For example, if the photoelectron gets energy E, and leaves the molecule in direction $\hat{\Omega}$, the total cross section $\sigma(O_2^+)$ can be written as

$$\sigma(O_2^+) = \int dE \int d\Omega \left[\frac{\partial^2 \sigma(O_2^+)}{\partial \Omega \partial E} \right] \tag{6.3}$$

The term in brackets is called a *differential cross section*. Differential photoionization cross sections can contain a great deal of information about the symmetry of the molecular orbitals [132] and the geometry of the molecule [133]. In the case of O^+, one could also

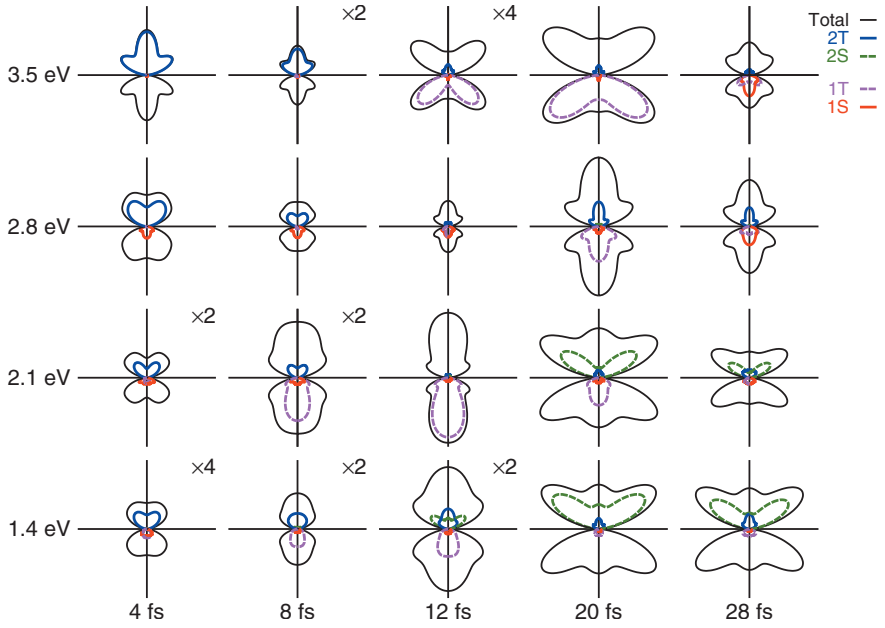

Figure 6.1: **Time Resolved Photoelectron Angular Distributions.** Theoretically predicted photoelectron angular distributions calculated by Arasaki et. al. [136] from aligned NO_2 molecules are shown as a function of delay and photoelectron energy. Pump and probe pulses are polarized in the vertical direction. Solid black lines indicate the total MFPAD, colored line indicate the partial distribution for different final states of the cation.

measure the kinetic energy release in the fragmentation of the molecule to learn about the potential energy curves of the cation [125]. In the present work, all of this information has been integrated away into a total cross section. Many studies have examined differential photoionization cross sections of atoms and molecules, but most of this work has been carried out with discharge lamp sources [134] and synchrotrons [135] and is not time-resolved. The merging of the technologies that measure differential photoionization cross sections and the VUV/XUV pump-probe techniques discussed in this thesis promises to be a challenging and exciting field of research in the years to come.

The potential rewards of this merger for our understanding of conical intersections and molecular dynamics are great. For example, in the present work, the decay of the excited electronic state C_2H_4 was inferred from the vanishing of the photoion signal produced by 7.7 eV probe photons just energetic enough to ionize the molecule from the minimum energy conical intersection. The argument for assigning the decay of the photoion signal to that of the excited electronic state is based on the energetics alone, but as discussed in chapter 4, other factors can cause the total photoion signal to vanish besides electronic relaxation. A better probe would examine the symmetry of the molecular orbital, which can change abruptly near the conical intersection. This will manifest itself in large changes in the angular distribution of the escaping electrons with respect to the molecule [136], or

the "molecular frame photoelectron angular distribution" (MFPAD). Measurements of the MFPAD perhaps offer the best probe of the evolution of the wave function in the vicinity of the conical intersection. Indeed, in a pioneering study measuring the time resolved MFPADs from excited CS_2 molecules, Bisgaard et. al. [137] detected oscillations in the MFPADs that reflect changes in the orbital character. In another example shown in figure 6.1, Arasaki et. al. [136] calculated time resolved MFPADs of the NO_2 molecule as the nuclear wave function crosses a conical intersection. Dramatic changes in the theoretically predicted distributions are observed as the system crosses the conical intersection near 12 and 20 fs, and the changes are directly attributable to changes in the electronic wave function [136].

Experimentally, the measurement of MFPADs requires determination of the orientation of the molecule under study. This is because when linearly polarized light interacts with an ensemble of randomly oriented molecules in the electric dipole approximation, the angular distribution of particles is, quite generally, restricted by angular momentum conservation to be of the functional form [138]

$$\frac{d\sigma}{d\Omega} = \frac{\sigma}{4\pi}\left[1 + \beta P_2(\cos\theta)\right] \tag{6.4}$$

where P_2 is the second order Legendre polynomial, θ is the angle between the emitted particle and the light polarization, and the "β-parameter" is restricted to be between -1 and 2. Alternative polarizations of the light field yield no information not contained in the β-parameter [138]. The structure of the MFPAD, which can have very high angular momentum content indicative of the orbital from which the photoelectron comes from, is then washed out into the p-wave distribution in equation (6.4) by the averaging over many molecules.

At the time of this writing, molecules are "aligned" for the measurement of differential photoionization cross sections in one of two ways: (1) torquing the molecule with a laser pulse [139], or (2) determining the emission angle of each detected electron with respect to its parent molecule by measuring the vector momenta of fragmentation products of the parent ion in coincidence [140]. Example experimental configurations of these two methods are depicted in figure 6.2. Each method has its advantages and disadvantages. Method (2) is commonly termed cold target recoil ion momentum spectroscopy, or COLTRIMS. The COLTRIMS technique also simultaneously records the kinetic energy release spectrum of the photofragments and thus constitutes a "kinematically complete experiment" from which fully differential cross sections can be reconstructed. However, it is restricted to cases where the molecular cation breaks apart after photoionization, and quickly, so that the momenta of the photoion fragments can be used to deduce the molecular orientation at the time of photoionization. It would be useless, for example, in measuring, the MFPAD for photoionization to states of O_2^+ that do not dissociate. Furthermore, since the method relies on the detection of particles in coincidence, the ion and electron count rates are limited to be on the order of ~ 1/shot or less to avoid false coincidences. The laser alignment technique is not restricted to dissociating cation states or low count rates. Furthermore, with short laser pulses, one can impulsively "kick" the molecule and one can have the probe pulse come picoseconds later at a revival of the rotational wave packet [141]. This allows a pump-probe experiment to be conducted under "field-free" conditions, without the extra perturbation of the aligning laser pulse [137]. However, in addition to requiring the spatiotemporal overlap

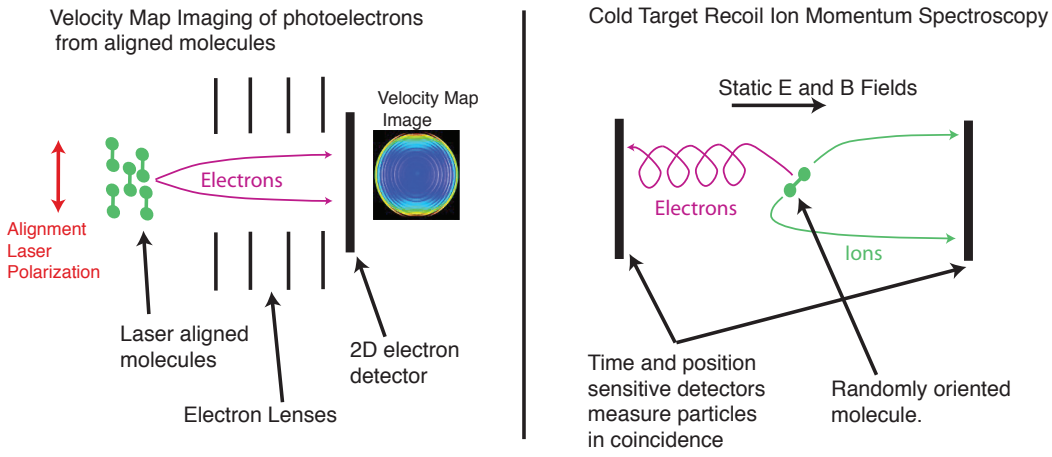

Figure 6.2: **Techniques for Measuring Molecular Frame Photoelectron Angular Distributions.** Left: the angular distribution of electrons with respect to laser aligned molecules can be recorded with an imaging electron detector. Right: With randomly oriented molecules, the orientation of the molecule can be reconstructed after the fact by measuring the vector momenta of two repulsive fragments in coincidence. The vector momenta of the particles are derived from Newton's equations of motion and from the measured times and positions of hits on two detectors, one for ions and one for electrons.

of yet another laser pulse, laser alignment is restricted to molecules with a large anisotropy in their polarizability tensors, so that one orientation of the molecule in the laser field has a decidedly lower energy.

The implementation of one or both charged particle detection schemes illustrated in figure 6.2 in a VUV/XUV pump-probe endstation will allow for detailed, systematic studies of the non-adiabatic dynamics of many small molecules. The largest hurdle to directly implementing differential cross section measurement on the present apparatus is the 10 Hz repetition rate. Since the ion and electron count rates are limited to be of order 1/shot or less in a COLTRIMS apparatus, repetition rate is the key parameter. The highest resolution COLTRIMS measurements currently come from experiments at synchrotrons with a pulse repetition rate in the MHz range. Some work has been done at kHz repetition rates with Ti:Sapphire lasers [40, 38], but 10 Hz is prohibitively low. Collecting charged particles from laser aligned molecules is not limited to 1 event/shot, but does require more data acquisition than in the present work to characterize the degree of alignment and obtain sufficient signal to noise in the differential cross section.

Increasing the repetition rate of the VUV/XUV pump probe apparatus requires high energy laser pulses at high repetition rate. At the time of this writing, several emerging laser technologies show promise towards this goal. The first to become commercially available is based on cryogenic cooling of Ti:Sapphire [142]. The average power limit in solid state lasers is often limited by the ability to remove heat from the solid state gain medium. At 77 K, the thermal conductivity of Ti:sapphire increases by a factor of 30

and the dependence of the refractive index on temperature responsible for thermal lensing, dn/dT, decreases by a factor of 7 compared to their respective values at 300 K [143]. The average power then becomes mainly limited by that available from pump-lasers. In another technique, the output of a femtosecond laser oscillator can be amplified through difference frequency generation (DFG) in an optical parametric amplifier (OPA). This method is called optical parametric chirped pulse amplification (OPCPA) [144]. Since in OPCPA no population inversion is pumped in the crystal used for DFG, no heat is deposited in the crystal. The single pass gain and gain bandwidth in OPCPA can also be much higher than in a conventional amplifier based on Ti:Sapphire. However, the OPCA method requires much more sophisticated pump lasers. A third route to high average power HHG uses a broad bandwidth Fabry-Perot cavity to passively amplify the pulse train of a carrier envelope phase stabilized laser [145]. The power inside the cavity is increased by a factor of F/π with respect to the input laser power, where F is the cavity finesse. Enhancement factors of over 230 with intracavity powers of 3 kW have been achieved [146]. This has allowed HHG at repetition rates exceeding 100 MHz at an intracavity focus [145, 147]. However, since the drive laser pulses are reused after HHG in such a system, distortions to the drive laser pulse as observed in figure 2.16 may impose limitations on the attainable HHG conversion efficiency. At the time of this writing the average power scaling of HHG sources remains an active areas of research.

6.2 X-ray Techniques

The measurement of differential XUV photoionization cross sections will be a powerful probe of dynamics of small molecules with a high degree of symmetry. However, for larger systems with less symmetry or no symmetry (e.g. Rhodopsin), there are conceptual and experimental difficulties. Conceptually, with the loss of symmetry in the molecule and the electronic orbitals beginning to form bands, the photoelectron angular distribution will likely just revert to the simple p-wave distribution of equation (6.4). Experimentally, both methods for obtaining MFPADs to image the evolution of a molecular orbital run into problems for larger systems. For laser alignment, simple diatomic or triatomic molecules do often display a much larger polarizability along the molecular axis, but the anisotropy of the polarizability tensor in general gets smaller as the size and complexity of a molecule grows. For COLTRIMS, the reconstruction of the molecular orientation from the ion fragment momenta becomes ambiguous for larger molecules with many fragmentation pathways. For this reason, most COLTRIMS studies have also so far been limited to simple diatomics and triatomics [140]. Both techniques, of course, are also out of the question for molecules in solution.

Several techniques to understand the structure of complex systems have been developed using x-rays from synchrotron light sources. Hard x-rays, with wavelengths on the order of 1 Å can be used to form diffraction images of molecules or larger complexes. Indeed, x-ray crystallography has become a workhorse method for biology, with many dedicated beamlines devoted solely to imaging biological macromolecules. Soft X-rays can be used for element specific absorption studies. Element specificity is achieved by tuning the x-ray wavelength near the binding energy of an element's core electrons. Near this "ab-

sorption edge" the absorption of a specific element can be much larger than other atoms of the host molecule. The excitation is then localized around the selected atom, and with this method, a smaller subunit of a larger molecule can be studied. Extending these techniques to the time domain with femtosecond x-ray pulses holds great promise for studying complex systems. Diffraction can be used to directly determine the positions of the nuclei during a phase transition [148, 149] or chemical reaction. Soft x-rays can be used to pump or probe the electronic structure around a specific element [150].

The extension of pump-probe techniques to the x-ray regime so far has been difficult due to a lack of sufficiently intense sources. Extensions of HHG into the soft x-ray may be possible [1, 151], but this has remained an experiment in itself for the last decade. In pioneering work, Schoenlein et. al. [152] have developed a technique to produce femtosecond pulses of x-rays from a synchrotron light source, but at a severe reduction in flux. HHG and synchrotron light sources can probably be safely ruled out for producing sufficient peak x-ray power to simultaneously provide pump *and* probe pulses in an x-ray pump/x-ray probe experiment. The most promising route towards high power femtosecond x-ray pulses is based on x-ray free electron laser (XFEL) technology. In an XFEL, micro-bunching in a relativistic electron beam leads to coherent x-ray power emerging from an undulator that scales quadratically with the number of electrons in the bunch, N_e^2, as opposed to the incoherent radiation from synchrotrons which scales only linearly with N_e. With nano-Coloumb bunches containing $\sim 10^{10}$ electrons, this means an increase in the peak x-ray power of 10 orders of magnitude. At the time of this writing, the Linac Coherent Light Source [2] has just become operational, and is producing pulse energies exceeding 2 mJ at photon energies up to 8.3 keV, or greater than 10^{12} photons per shot in $\sim$ 100 fs pulses. At these obscene peak x-ray powers, multiple photon absorption is the rule rather than the exception [153, 154] at the focus of a full power XFEL beam, and the peak power is no longer a limitation for pump-probe studies.

There are many technical issues still to confront, but it is not unreasonable to forecast that the orchestration of infrared and visible laser technology, high order harmonic generation, and seeded free electron lasers working in concert will lead to the ability to expose a system to a nearly arbitrary coherent electromagnetic waveform of the experimenter's desire, at least with amplitude and frequency modulation on timescales relevant to chemistry and biology. The work in this thesis represents some small steps towards that larger goal.

Bibliography

[1] T. Brabec and F. Krausz. Intense few cycle laser fields: Frontiers of nonlinear optics. *Rev. Mod. Phys.*, 72:545–591, 2000.

[2] http://lcls.slac.stanford.edu/.

[3] J. Corlett, K. Baptiste, J. Byrd, P. Denes, R. Falcone, J. Kirz, W. McCurdy, H. Padmore, G. Penn, J. Qiang, D. Robin, F. Sannibale, R. Schoenlein, J. Staples, C. Steier, M. Venturini, W. Wan, W. Wells, R. Wilcox, and A. Zholents. Design studies for a vuv soft x-ray free-electron laser array. *Synchrotron Radiation News*, 22, 2009.

[4] G. Stupakov. Using the beam-echo effect for generation of short-wavelength radiation. *Phys. Rev. Lett.*, 102(7):074801, Feb 2009.

[5] F.C. Kafatos and T. Eisner. Unification in the century of biology. *Science*, 303:1257, 2004.

[6] John Hemminger. Directing matter and energy: Five challenges for science and the imagination, a report from the basic energy sciences advisory committee. Technical report, U.S. Dept of Energy, 2007.

[7] RW Schoenlein, LA Peteanu, RA Mathies, and CV Shank. The first step in vision: femtosecond isomerization of rhodopsin. *Science*, 254(5030):412–415, 1991.

[8] Graham R Fleming and Rienk van Grondelle. Femtosecond spectroscopy of photosynthetic light-harvesting systems. *Current Opinion in Structural Biology*, 7(5):738 – 748, 1997.

[9] U. Fano and J. W. Cooper. Spectral distribution of atomic oscillator strengths. *Rev. Mod. Phys.*, 40:441, 1968.

[10] J. Berkowitz. *Photoabsorption, Photoionization, and Photoelectron Spectroscopy*. Academic Press, 1979.

[11] J. A. R. Samson. *Techniques of Vacuum Ultraviolet Spectroscopy*. Pied Publications, 1967.

[12] W. Kohn. Nobel lecture: Electronic structure of matter—wave functions and density functionals. *Rev. Mod. Phys.*, 71(5):1253–1266, Oct 1999.

[13] D. J. Tannor. *Introduction to Quantum Mechanics, A Time Dependent Perspective*. University Science Books, 2007.

[14] D. J. Griffiths. *Introduction to Quantum Mechanics*. Prentice-Hall, 1995.

[15] John A. Pople. Nobel lecture: Quantum chemical models. *Rev. Mod. Phys.*, 71(5):1267–1274, Oct 1999.

[16] M. Ben-Nun, J. Quenneville, and T. J. Martinez. Ab initio multiple spawning: Photochemistry from first principles quantum molecular dynamics. *J. Phys. Chem. A*, 104(22):5161–5175, 05 2000.

[17] David R. Yarkony. Conical intersections: The new conventional wisdom. *The Journal of Physical Chemistry A*, 105(26):6277–6293, 06 2001.

[18] Christer Z. Bisgaard, Helmut Satzger, Susanne Ullrich, and Albert Stolow. Excited-State Dynamics of Isolated DNA Bases: A Case Study of Adenine. *Chem. Phys. Chem.*, 10(1):101–110, 2009.

[19] A.E. Siegman. *Lasers*. University Science Books, 1986.

[20] Y. Wang, E. Granados, M. A. Larotonda, M. Berrill, B. M. Luther, D. Patel, C. S. Menoni, and J. J. Rocca. High-brightness injection-seeded soft-x-ray-laser amplifier using a solid target. *Phys. Rev. Lett.*, 97(12):123901, Sep 2006.

[21] Ph. Zeitoun, G. Faivre, S. Sebban, T. Mocek, A. Hallou, M. Fajardo, D. Aubert, Ph. Balcou, F. Burgy, D. Douillet, S. Kazamias, G. de Lacheze-Murel, T. Lefrou, S. le Pape, P. Mercere, H. Merdji, A. S. Morlens, J. P. Rousseau, and C. Valentin. A high-intensity highly coherent soft x-ray femtosecond laser seeded by a high harmonic beam. *Nature*, 431(7007):426–429, 09 2004.

[22] R.W. Boyd. *Nonlinear Optics*. Academic Press, Amsterdam, second edition, 2003.

[23] Y. R. Shen. *The Principles of Nonlinear Optics*. Wiley, 1984.

[24] L. V. Keldysh Sov. Phys. JETP. *20*, page 1307, 1965.

[25] P. B. Corkum. Plasma perspective on strong-field multiphoton ionization. *Phys. Rev. Lett*, 71:1994–1997, 1993.

[26] M. Lewenstein, Ph. Balcou, M. Yu Ivanov, Anne L'Huillier, and P. B. Corkum. Theory of high order harmonic generation by low-frequency laser fields. *Phys. Rev. A*, 49:2117–2132, 1994.

[27] Ferenc Krausz and Misha Ivanov. Attosecond physics. *Rev. Mod. Phys.*, 81(1):163–234, Feb 2009.

[28] E. Hecht. *Optics*. Addison-Wesley, 1998.

[29] F. Quéré, C. Thaury, P. Monot, S. Dobosz, Ph. Martin, J.-P. Geindre, and P. Audebert. Coherent wake emission of high-order harmonics from overdense plasmas. *Phys. Rev. Lett.*, 96(12):125004, Mar 2006.

[30] T. D. Donnelly, T. Ditmire, K. Neuman, M. D. Perry, and R. W. Falcone. High-order harmonic generation in atom clusters. *Phys. Rev. Lett.*, 76(14):2472–2475, Apr 1996.

[31] W. Boutu, S. Haessler, H. Merdji, P. Breger, G. Waters, M. Stankiewicz, L. J. Frasinski, R. Taieb, J. Caillat, A. Maquet, P. Monchicourt, B. Carre, and P. Salieres. Coherent control of attosecond emission from aligned molecules. *Nature Physics*, 4(7):545–549, 2008.

[32] M. A. Heald and J. B. Marion. *Classical Electromagnetic Radiation*. Saunder College Pub., 1995.

[33] P. Balcou, P. Salieres, A. L'Huiller, and M. Lewenstein. Generalized phase-matching conditions for high harmonics: The role of field gradient forces. *Phys. Rev. A.*, 55:3204, 1997.

[34] Mette B. Gaarde and Kenneth J. Schafer. Quantum path distributions for high-order harmonics in rare gas atoms. *Phys. Rev. A*, 65(3):031406, Mar 2002.

[35] Y. Mairesse, A. de Bohan, L. J. Frasinski, H. Merdji, L. C. Dinu, P. Monchicourt, P. Breger, M. Kovacev, R. Taieb, B. Carre, H. G. Muller, P. Agostini, and P. Salieres. Attosecond Synchronization of High-Harmonic Soft X-rays. *Science*, 302(5650):1540–1543, 2003.

[36] E. Constant, D. Garzella, P. Breger, E. Mevel, Ch. Dorrer, C. Le Blanc, F. Salin, and P. Agostini. Optimization of high harmonic generation in absorbing gasss model and experiment. *Phys. Rev. Lett.*, 82:1668, 1999.

[37] E.J. Takahashi, Y. Nabekawa, H. Mashiko, H. Hasegawa, A. Suda, and K. Midorikawa. Generation of strong optical field in soft x-ray region by using high-order harmonics. *IEEE Journal of Selected Topics in Quantum Electronics*, 10(6):1315–1328, Nov.-Dec. 2004.

[38] Arvinder S. Sandhu, Etienne Gagnon, Robin Santra, Vandana Sharma, Wen Li, Phay Ho, Predrag Ranitovic, C. Lewis Cocke, Margaret M. Murnane, and Henry C. Kapteyn. Observing the Creation of Electronic Feshbach Resonances in Soft X-ray-Induced O-2 Dissociation. *Science*, 322(5904):1081–1085, 2008.

[39] D. T. Attwood. *Soft X-rays and Extreme Ultraviolet Radiation*. Cambridge University Press, 1999.

[40] Etienne Gagnon, Predrag Ranitovic, Xiao-Min Tong, C. L. Cocke, Margaret M. Murnane, Henry C. Kapteyn, and Arvinder S. Sandhu. Soft x-ray-driven femtosecond molecular dynamics. *Science*, 317(5843):1374–1378, 2007.

[41] M. V. Ammosov, N. B. Delone, and V. P. Krainov. *Zh. Eksp. Teor. Fiz.*, 91:2008.

[42] Charles G. Durfee, Andy R. Rundquist, Sterling Backus, Catherine Herne, Margaret M. Murnane, and Henry C. Kapteyn. Phase matching of high-order harmonics in hollow waveguides. *Phys. Rev. Lett.*, 83(11):2187–2190, Sep 1999.

[43] Mark J. Abel, Thomas Pfeifer, Phillip M. Nagel, Willem Boutu, M. Justine Bell, Colby P. Steiner, Daniel M. Neumark, and Stephen R. Leone. Isolated attosecond pulses from ionization gating of high-harmonic emission. *Chemical Physics*, 366(1-3):9 – 14, 2009. Attosecond Molecular Dynamics.

[44] J.-F. Hergott, M. Kovacev, H. Merdji, C. Hubert, Y. Mairesse, E. Jean, P. Breger, P. Agostini, B. Carré, and P. Salières. Extreme-ultraviolet high-order harmonic pulses in the microjoule range. *Phys. Rev. A*, 66(2):021801, Aug 2002.

[45] S. Kazamias, D. Douillet, C. Valentin, Th. Lefrou, G. Grillon, G. Mullot, F. Augé, P. Mercère, Ph. Zeitoun, and Ph. Balcou. Optimization of the focused flux of high harmonics. *Eur. Phys. J. D*, 26(1):47–50, oct 2003.

[46] X-ray interactions with matter calculator: http://henke.lbl.gov/.

[47] A. Börzsönyi, Z. Heiner, M. P. Kalashnikov, A. P. Kovács, and K. Osvay. Dispersion measurement of inert gases and gas mixtures at 800 nm. *Appl. Opt.*, 47(27):4856–4863, 2008.

[48] J. D. Jackson. *Classical Electrodynamics*. Wiley, 1998.

[49] Yusuke Tamaki, Jiro Itatani, Minoru Obara, and Katsumi Midorikawa. Optimization of conversion efficiency and spatial quality of high-order harmonic generation. *Phys. Rev. A*, 62(6):063802, Nov 2000.

[50] Eiji Takahashi, Yasuo Nabekawa, Tatsuya Otsuka, Minoru Obara, and Katsumi Midorikawa. Generation of highly coherent submicrojoule soft x rays by high-order harmonics. *Phys. Rev. A*, 66(2):021802, Aug 2002.

[51] J. Bonse, S. Baudach, W. Kautek, E. Welsch, and J. Krger. Femtosecond laser damage of a high reflecting mirror. *Thin Solid Films*, 408(1-2):297 – 301, 2002.

[52] A.E. Siegman and S.W. Townsend. Output beam propagation and beam quality from a multimode stable-cavity laser. *Quantum Electronics, IEEE Journal of*, 29(4):1212 –1217, apr 1993.

[53] John F. O'Hanlon. *A User's Guide to Vacuum Technology*. Wiley, 2003.

[54] Sterling Backus, Charles G. Durfee III, Margaret M. Murnane, and Henry C. Kapteyn. High power ultrafast lasers. *Review of Scientific Instruments*, 69(3):1207–1223, 1998.

[55] A. Sullivan, H. Hamster, H. C. Kapteyn, S. Gordon, W. White, H. Nathel, R. J. Blair, and R. W. Falcone. Multiterawatt, 100-fs laser. *Opt. Lett.*, 16(18):1406–1408, 1991.

[56] Melanie T. Asaki, Chung-Po Huang, Dennis Garvey, Jianping Zhou, Henry C. Kapteyn, and Margaret M. Murnane. Generation of 11-fs pulses from a self-mode-locked Ti:Sapphire laser. *Opt. Lett.*, 18(12):977–979, 1993.

[57] A. Offner and D. Conn. U. S. Patent Number 3748015, 1973.

[58] S. Kane and J. Squier. Fourth-order-dispersion limitations of aberration-free chirped-pulse amplification systems. *J. Opt. Soc. Am. B*, 14(5):1237–1244, 1997.

[59] J. Qiang, J. M. Byrd, J. Feng, and G. Huang. X-ray streak camera temporal resolution improvement using a longitudinal time-dependent field. *Nucl. Instrum. Meth. A*, 598(2):465–469, 2009.

[60] N. W. Ashcroft and N. David Mermin. *Solid State Physics*. Harcourt College Publishers, 1975.

[61] R. W. Falcone and J. Bokor. Dichroic beam splitter for extreme-ultraviolet and visible radiation. *Opt. Lett.*, 8(1):21, 1983.

[62] E. J. Takahashi, H. Hasegawa, Y. Nabekawa, and K. Midorikawa. High-throughput, high-damage-threshold broadband beam splitter for high-order harmonics in the extreme-ultraviolet region. *Opt. Lett.*, 29(5):507–509, 2004.

[63] E. D. Palik. *Handbook of Optical Constants of Solids*. Academic Press, 1998.

[64] C. V. Shank, R. Yen, and C. Hirlimann. Time-resolved reflectivity measurements of femtosecond-optical-pulse-induced phase transitions in silicon. *Phys. Rev. Lett*, 50:454, 1983.

[65] C. V. Shank, R. Yen, and C. Hirlimann. Femtosecond-time resolved surface structural dynamics of optically excited si. *Phys. Rev. Lett*, 51:900, 1983.

[66] H. W. K. Tom and G. D. Aumiller. Time resolved study of laser induced disorder of si surfaces. *Phys. Rev. Lett*, 60:1438, 1988.

[67] James H. Underwood, Eric M. Gullikson, Masato Koike, and Phillip J. Batson. Beamline for metrology of x-ray/euv optics at the advanced light source. volume 3113, pages 214–221. SPIE, 1997.

[68] International radiation detectors, inc. http://www.ird-inc.com/index.html.

[69] Eli Yablonovitch. Self-phase modulation and short-pulse generation from laser-breakdown plasmas. *Phys. Rev. A*, 10(5):1888–1895, Nov 1974.

[70] C. Fourcade Dutin, A. Dubrouil, S. Petit, E. Mével, E. Constant, and D. Descamps. Post-compression of high-energy femtosecond pulses using gas ionization. *Opt. Lett.*, 35(2):253–255, 2010.

[71] A. Sullivan. *Propagation of high-intensity, ultrashort laser pulses in plasmas*. PhD thesis, University of California at Berkeley, 1993.

[72] P. Tzallas, D. Charalambidis, N. A. Papadogiannis, K. Witte, and G. D. Tsakiris. Direct observation of attosecond light bunching. *Nature*, 426:267, 2003.

[73] O. Faucher, P. Tzallas, E. P. Benis, J. Kruse, A. Peralta Conde, C. Kalpouzos, and D. Charalambidis. Four-dimensional investigation of the 2nd order volume autocorrelation technique. *Appl. Phys. B*, 97(2):505–510, OCT 2009.

[74] Y. Kondo, T. Ejima, K. Saito, T. Hatano, and M. Watanabe. High-reflection multilayer for wavelength range of 200-30 nm. *Nucl. Instrum. Methods Phys. Res. A*, 467-468:333, 2001.

[75] W. Ronald Gentry. Low-energy pulsed beam sources. In G. Scoles, editor, *Atomic and Molecular Beam Methods*. Oxford University Press, 1988.

[76] J. R. Taylor. *An Introduction to Error Analysis*. University Science Books, 1997.

[77] T. Ibuki, G. Cooper, and C. E. Brion. Absolute dipole oscillator strengths for photoabsorption and the molecular and dissociative photoionization of ethylene. *Chemical Physics*, 129(3):295 – 309, 1989.

[78] P. LaPorte, J. L. Subtil, M. Courbon, M. Bon, and L. Vincent. Vacuum-ultraviolet refractive index of LiF and MgF_2 in the temperature range 80-300 K. *J. Opt. Soc. Am.*, 73(8):1062, August 1983.

[79] Masahiko Daimon and Akira Masumura. High-accuracy measurements of the refractive index and its temperature coefficient of calcium fluoride in a wide wavelength range from 138 to 2326 nm. *Appl. Opt.*, 41(25):5275–5281, 2002.

[80] Taro Sekikawa, Tomotaka Katsura, Satoshi Miura, and Shuntaro Watanabe. Measurement of the intensity-dependent atomic dipole phase of a high harmonic by frequency-resolved optical gating. *Phys. Rev. Lett.*, 88(19):193902, Apr 2002.

[81] P. Balcou, A. S. Dederichs, M. B. Gaarde, and A. L'Huillier. Quantum-path analysis and phase matching of high-order harmonic generation and high-order frequency mixing processes in strong laser fields. *Journal of Physics B: Atomic, Molecular and Optical Physics*, 32(12):2973–2989, 1999.

[82] Alexander L. Gaeta. Catastrophic collapse of ultrashort pulses. *Phys. Rev. Lett.*, 84(16):3582–3585, Apr 2000.

[83] C. Dugave and L. Demange. Cis-trans isomerization of organic molecules and biomolecules: Implications and applications. *Chem. Rev.*, 103(7):2475–2532, JUL 2003.

[84] Production: Growth is the norm. *Chemical and Engineering News*, July 10:59, 2006.

[85] Zhefeng Lin, Silin Zhong, and Don Grierson. Recent advances in ethylene research. *J. Exp. Bot.*, 60(12):3311–3336, 2009.

[86] B. H. Bransden and C. J. Joachain. *Physics of Atoms and Molecules*. Addison-Wesley Longman Limited, 1983.

[87] Roseanne J. Sension and Bruce S. Hudson. Vacuum ultraviolet resonance Raman studies of the excited electronic states of ethylene. *The Journal of Chemical Physics*, 90(3):1377–1389, 1989.

[88] T. Shimanouchi. *Tables of Molecular Vibrational Frequencies Consolidated Volume I*. National Institute of Standards, 1972.

[89] Wikimedia commons, http://commons.wikimedia.org.

[90] E. M. Evleth and A. Sevin. Theoretical study of the role of valence and rydberg states in the photochemistry of ethylene. *Journal of the American Chemical Society*, 103(25):7414–7422, 12 1981.

[91] K. Kosma, S. A. Trushin, W. Fuss, and W. E. Schmid. Ultrafast dynamics and coherent oscillations in ethylene and ethylene-d4 excited at 162 nm. *J. Phys. Chem. A*, 112(33):7514–7529, 2008.

[92] Patricia Ann Snyder, Sylvia Atanasova, and Roger W. C. Hansen. Ethylene. Experimental evidence for new assignments of electronic transitions in the $\pi \rightarrow \pi^*$ energy region. Absorption and magnetic circular dichroism measurements with synchrotron radiation. *The Journal of Physical Chemistry A*, 108(19):4194–4201, 04 2004.

[93] P. G. Wilkinson and R. S. Mulliken. Far ultraviolet aborption spectra of ethylene and ethylene-d4. *J. Chem. Phys.*, 23:1895, 1955.

[94] M. Barbatti, J. Paier, and H. Lischka. Photochemistry of ethylene: A multireference configuration interaction investigation of the excited-state energy surfaces. *The Journal of Chemical Physics*, 121(23):11614–11624, 2004.

[95] Benjamin G. Levine, Joshua D. Coe, and Todd J. Martinez. Optimizing conical intersections without derivative coupling vectors: Application to multistate multireference second-order perturbation theory (MS-CASPT2). *The Journal of Physical Chemistry B*, 112(2):405–413, 12 2007.

[96] Hongli Tao, Benjamin G. Levine, and Todd J. Martínez. Ab initio multiple spawning dynamics using multi-state second-order perturbation theory. *The Journal of Physical Chemistry A*, 113(49):13656–13662, 11 2009.

[97] M. Barbatti, G. Granucci, M. Persico, and H. Lischka. Semiempirical molecular dynamics investigation of the excited state lifetimes of ethylene. *Chem. Phys. Lett.*, 401:276–281, 2005.

[98] M. Barbatti, M. Ruckenbauer, and H. Lischka. The photodynamics of ethylene: A surface-hopping study on structural aspects. *The Journal of Chemical Physics*, 122(17):174307, 2005.

[99] Jim J. Lin, Dennis W. Hwang, Yuan T. Lee, and Xueming Yang. Site and isotope effects on the molecular hydrogen elimination from ethylene at 157 nm excitation. *The Journal of Chemical Physics*, 109(8):2979–2982, 1998.

[100] Jim J. Lin, Chia C. Wang, Yuan T. Lee, and Xueming Yang. Site-specific dissociation dynamics of ethylene at 157 nm: Atomic and molecular hydrogen elimination. *J. Chem. Phys.*, 113(21):9668–9677, 2000.

[101] Shih-Huang Lee, Yuan T. Lee, and Xueming Yang. Dynamics of photodissociation of ethylene and its isotopomers at 157 nm: Branching ratios and kinetic-energy distributions. *The Journal of Chemical Physics*, 120(23):10983–10991, 2004.

[102] Shih-Huang Lee, Yao-Chang Lee, and Yuan T. Lee. Site and isotopic effects on the angular anisotropy of products in the photodissociation of ethene at 157 nm. *The Journal of Physical Chemistry A*, 110(7):2337–2344, 02 2006.

[103] P. Farmanara, O. Steinkellner, M. T. Wick, M. Wittmann, G. Korn, V. Stert, and W. Radloff. Ultrafast internal conversion and photodissociation of molecules excited by femtosecond 155 nm laser pulses. *The Journal of Chemical Physics*, 111(14):6264–6270, 1999.

[104] J. M. Mestdagh, J. P. Visticot, M. Elhanine, and B. Soep. Prereactive evolution of monoalkenes excited in the 6 ev region. *The Journal of Chemical Physics*, 113(1):237–248, 2000.

[105] V. Stert, H. Lippert, H.-H. Ritze, and W. Radloff. Femtosecond time-resolved dynamics of the electronically excited ethylene molecule. *Chemical Physics Letters*, 388:144–149, 2004.

[106] Hanneli R. Hudock, Benjamin G. Levine, Alexis L. Thompson, Helmut Satzger, D. Townsend, N. Gador, S. Ullrich, Albert Stolow, and Todd J. Martnez. Ab initio molecular dynamics and time-resolved photoelectron spectroscopy of electronically excited uracil and thymine. *The Journal of Physical Chemistry A*, 111(34):8500–8508, 08 2007.

[107] A. Peralta Conde, J. Kruse, O. Faucher, P. Tzallas, E. P. Benis, and D. Charalambidis. Realization of time-resolved two-vacuum-ultraviolet-photon ionization. *Phys. Rev. A*, 79(6):061405, Jun 2009.

[108] G. M. Bluemenstock, R.A.M Keski-Kuha, and M. L. Ginter. Extreme ultraviolet optical properties of ion beam deposited boron carbide thin films. *Proc. SPIE-Int. Soc. Opt. Eng.*, 2515:558, 1995.

[109] S. A. Trushin, W. E. Schmid, and W. Fuss. A time constant of 1.8 fs in the dissociation of water excited at 162 nm. *Chem. Phys. Lett.*, 468:9–13, 2009.

[110] Glyn Cooper, Toshio Ibuki, Yoshihiro Iida, and C. E. Brion. Absolute dipole oscillator strengths for photoabsorption and the molecular and dissociative photoionization of acetylene. *Chemical Physics*, 125(2-3):307 – 320, 1988.

[111] C. Sannen, G. Raseev, C. Galloy, G. Fauville, and J. C. Lorquet. Unimolecular decay paths of electronically excited species. ii. the $C_2H_4^+$ ion. *The Journal of Chemical Physics*, 74(4):2402–2411, 1981.

[112] Fabio Costa. Electronic structure study of the reaction $C_2H_4^+ \rightarrow C_2H_2^+ + H_2$. *International Journal of Quantum Chemistry*, 106(13, Sp. Iss. SI):2763–2771, 2006.

[113] A. H. H. Chang, A. M. Mebel, X. M. Yang, S. H. Lin, and Y. T. Lee. Ab initio calculations of potential energy surface and rate constants for ethylene photodissociation at 193 and 157 nm. *Chemical Physics Letters*, 287(3-4):301 – 306, 1998.

[114] B. G. Levine, J. D. Coe, A. M. Virshup, and T. J. Martinez. Implementation of *ab initio* multiple spawning in the molpro quantum chemistry package. *Chemical Physics*, 347:3–16, 2008.

[115] Evan F. Cromwell, Albert Stolow, Marcus J. J. Vrakking, and Yuan T. Lee. Dynamics of ethylene photodissociation from rovibrational and translational energy distributions of H_2 products. *The Journal of Chemical Physics*, 97(6):4029–4040, 1992.

[116] A. H. H. Chang, D. W. Hwang, X.-M. Yang, A. M. Mebel, S. H. Lin, and Y. T. Lee. Toward the understanding of ethylene photodissociation: Theoretical study of energy partition in products and rate constants. *The Journal of Chemical Physics*, 110(22):10810–10820, 1999.

[117] Shih-Huang Lee and Yuan T. Lee. Dependence of the distributions of kinetic energies of products on photoionization energy in the photodissociation of ethene at 157nm. *Chemical Physics Letters*, 419(1-3):158 – 163, 2006.

[118] S. J. Desjardins, A. D. O. Bawagan, Z. F. Liu, K. H. Tan, Y. Wang, and E. R. Davidson. Correlation states of ethylene. *J. Chem. Phys.*, 102(16):6385–6399, 1995.

[119] R. A. Mackie, S. W. J. Scully, A. M. Sands, R. Browning, K. F. Dunn, and C. J. Latimer. A photoionization mass spectrometric study of acetylene and ethylene in the VUV spectral region. *International Journal of Mass Spectrometry*, 223-224:67 – 79, 2003.

[120] A. C. Allison, S. L. Guberman, and A. Dalgarno. A model of the Schumann-Runge continuum of O_2. *J. Geophys. Res.*, 91(A9):10193–10198, 1986.

[121] Jim J. Lin, Dennis W. Hwang, Yuan T. Lee, and Xueming Yang. Photodissociation of O_2 at 157 nm: Experimental observation of anisotropy mixing in the $O_2 + h\nu \rightarrow O(^3P) + O(^3P)$ channel. *The Journal of Chemical Physics*, 109(5):1758–1762, 1998.

[122] A. Goldberg, H. M. Schey, and J. L. Schwartz. Computer generated motion pictures of one-dimensional quantum mechanical transmission and reflection phenomena. *Am. J. Phys.*, 35:177, 1967.

[123] R. P. Saxon and B. Liu. Ab initio configuration interaction study of the valence states of O_2. *J. Chem. Phys.*, 67:5432, 1977.

[124] M. V. Korolkov and B. Schmidt. Vibrationally state-selective laser pulse control of electronic branching in oh (x/a) photoassociation. *Chemical Physics*, 237(1-2):123 – 138, 1998.

[125] Y. Lu, Z. X. He, J. N. Cutler, S. H. Southworth, W. C. Stolte, and J. A. R. Samson. Dissociative photoionization study of O_2. *Journal of Electron Spectroscopy and Related Phenomena*, 94(1-2):135 – 147, 1998.

[126] Nelson H. F. Beebe, Erik W. Thulstrup, and Andreas Andersen. Configuration interaction calculations of low-lying electronic states of O_2, O_2^+, O_2^{2+}. *The Journal of Chemical Physics*, 64(5):2080–2093, 1976.

[127] Ph. Wernet, M. Odelius, K. Godehusen, J. Gaudin, O. Schwarzkopf, and W. Eberhardt. Real-time evolution of the valence electronic structure in a dissociating molecule. *Phys. Rev. Lett.*, 103(1):013001, Jun 2009.

[128] Lora Nugent-Glandorf, Michael Scheer, David A. Samuels, Anneliese M. Mulhisen, Edward R. Grant, Xueming Yang, Veronica M. Bierbaum, and Stephen R. Leone. Ultrafast time-resolved soft x-ray photoelectron spectroscopy of dissociating Br_2. *Phys. Rev. Lett.*, 87(19):193002, Oct 2001.

[129] Daniel Strasser, Fabien Goulay, and Stephen R. Leone. Transient photoelectron spectroscopy of the dissociative $Br_2(^1\Pi_u)$ state. *The Journal of Chemical Physics*, 127(18):184305, 2007.

[130] W. Li, V. Sharma, C. Hogle, A. Jaron-Becker, A. Becker, H. Kapteyn, and M. Murnane. Ultrafast molecular dynamics probed using strong field ionization. In *Second International Conference on Attosecond Physics*, 2009.

[131] Oliver Schalk, Andrey E. Boguslavskiy, and Albert Stolow. Substituent effects on dynamics at conical intersections: Cyclopentadienes. *The Journal of Physical Chemistry A*, 114(12):4058–4064, 03 2010.

[132] Dan Dill, Jon Siegel, and J. L. Dehmer. Spectral variation of fixed-molecule photoelectron angular distributions. *The Journal of Chemical Physics*, 65(8):3158–3160, 1976.

[133] A. Landers, Th. Weber, I. Ali, A. Cassimi, M. Hattass, O. Jagutzki, A. Nauert, T. Osipov, A. Staudte, M. H. Prior, H. Schmidt-Böcking, C. L. Cocke, and R. Dörner. Photoelectron diffraction mapping: Molecules illuminated from within. *Phys. Rev. Lett.*, 87(1):013002, Jun 2001.

[134] P. J. Richardson, J. H. D. Eland, P. G. Fournier, and D. L. Cooper. Spectrum and decay of the doubly charged water ion. *The Journal of Chemical Physics*, 84(6):3189–3194, 1986.

[135] M. S. Schoffler, J. Titze, N. Petridis, T. Jahnke, K. Cole, L. Ph. H. Schmidt, A. Czasch, D. Akoury, O. Jagutzki, J. B. Williams, N. A. Cherepkov, S. K. Semenov, C. W.

McCurdy, T. N. Rescigno, C. L. Cocke, T. Osipov, S. Lee, M. H. Prior, A. Belkacem, A. L. Landers, H. Schmidt-Bocking, Th. Weber, and R. Dorner. Ultrafast probing of core hole localization in N_2. *Science*, 320(5878):920–923, 2008.

[136] Yasuki Arasaki, Kazuo Takatsuka, Kwanghsi Wang, and Vincent McKoy. Time-resolved photoelectron spectroscopy of wavepackets through a conical intersection in NO_2. *The Journal of Chemical Physics*, 132(12):124307, 2010.

[137] Christer Z. Bisgaard, Owen J. Clarkin, Guorong Wu, Anthony M. D. Lee, Oliver Gessner, Carl C. Hayden, and Albert Stolow. Time-resolved molecular frame dynamics of fixed-in-space CS_2 molecules. *Science*, 323:1464, 2009.

[138] Steven T. Manson and Anthony F. Starace. Photoelectron angular distributions: energy dependence for *s* subshells. *Rev. Mod. Phys.*, 54(2):389–405, Apr 1982.

[139] Henrik Stapelfeldt and Tamar Seideman. Colloquium: Aligning molecules with strong laser pulses. *Rev. Mod. Phys.*, 75(2):543–557, Apr 2003.

[140] J Ullrich, R Moshammer, A Dorn, R Dörner, L Ph H Schmidt, and H Schmidt-Böcking. Recoil-ion and electron momentum spectroscopy: reaction-microscopes. *Reports on Progress in Physics*, 66(9):1463, 2003.

[141] I. V. Litvinyuk, Kevin F. Lee, P. W. Dooley, D. M. Rayner, D. M. Villeneuve, and P. B. Corkum. Alignment-dependent strong field ionization of molecules. *Phys. Rev. Lett.*, 90(23):233003, Jun 2003.

[142] Sterling Backus, Randy Bartels, Sarah Thompson, Robert Dollinger, Henry C. Kapteyn, and Margaret M. Murnane. High-efficiency, single-stage 7-khz high-average-power ultrafast laser system. *Opt. Lett.*, 26(7):465–467, 2001.

[143] P.A. Schulz and S.R. Henion. Liquid-nitrogen-cooled Ti:Al_2O_3 laser. *Quantum Electronics, IEEE Journal of*, 27(4):1039 –1047, Apr 1991.

[144] S. Witte, R. Zinkstok, W. Hogervorst, and K. Eikema. Generation of few-cycle terawatt light pulses using optical parametric chirped pulse amplification. *Opt. Express*, 13(13):4903–4908, 2005.

[145] Dylan C. Yost, Thomas R. Schibli, Jun Ye, Jennifer L. Tate, James Hostetter, Mette B. Gaarde, and Kenneth J. Schafer. Vacuum-ultraviolet frequency combs from below-threshold harmonics. *Nat Phys*, 5(11):815–820, 11 2009.

[146] I. Hartl, T. R. Schibli, A. Marcinkevicius, D. C. Yost, D. D. Hudson, M. E. Fermann, and Jun Ye. Cavity-enhanced similariton yb-fiber laser frequency comb: 3×10^{14} W/cm^2 peak intensity at 136 MHz. *Opt. Lett.*, 32(19):2870–2872, 2007.

[147] A. Ozawa, J. Rauschenberger, Ch. Gohle, M. Herrmann, D. R. Walker, V. Pervak, A. Fernandez, R. Graf, A. Apolonski, R. Holzwarth, F. Krausz, T. W. Hänsch, and Th. Udem. High harmonic frequency combs for high resolution spectroscopy. *Phys. Rev. Lett.*, 100(25):253901, 2008.

[148] A. M. Lindenberg, J. Larsson, K. Sokolowski-Tinten, K. J. Gaffney, C. Blome, O. Synnergren, J. Sheppard, C. Caleman, A. G. MacPhee, D. Weinstein, D. P. Lowney, T. K. Allison, T. Matthews, R. W. Falcone, A. L. Cavalieri, D. M. Fritz, S. H. Lee, P. H. Bucksbaum, D. A. Reis, J. Rudati, P. H. Fuoss, C. C. Kao, D. P. Siddons, R. Pahl, J. Als-Nielsen, S. Duesterer, R. Ischebeck, H. Schlarb, H. Schulte-Schrepping, Th. Tschentscher, J. Schneider, D. von der Linde, O. Hignette, F. Sette, H. N. Chapman, R. W. Lee, T. N. Hansen, S. Techert, J. S. Wark, M. Bergh, G. Huldt, D. van der Spoel, N. Timneanu, J. Hajdu, R. A. Akre, E. Bong, P. Krejcik, J. Arthur, S. Brennan, K. Luening, and J. B. Hastings. Atomic-scale visualization of inertial dynamics. *Science*, 308:392, 2005.

[149] A. M. Lindenberg, I. Kang, S. L. Johnson, T. Missalla, P. A. Heimann, Z. Chang, J. Larsson, P. H. Bucksbaum, H. C. Kapteyn, H. A. Padmore, R. W. Lee, J. S. Wark, and R. W. Falcone. Time-resolved x-ray diffraction from coherent phonons during a laser-induced phase transition. *Phys. Rev. Lett.*, 84(1):111–114, Jan 2000.

[150] Christian Bressler and Majed Chergui. Time-resolved X-ray absorption spectroscopy. *Actualite Chimique*, (317):59–61, 2008.

[151] Tenio Popmintchev, Ming-Chang Chen, Alon Bahabad, Michael Gerrity, Pavel Sidorenko, Oren Cohen, Ivan P. Christov, Margaret M. Murnane, and Henry C. Kapteyn. Phase matching of high harmonic generation in the soft and hard X-ray regions of the spectrum. *Proceedings of the National Academy of Sciences*, 106(26):10516–10521, 2009.

[152] R. W. Schoenlein, S. Chattopadhyay, H. H. Chong, T. E. Glover, P. A. Heimann, C. V. Shank, A. A. Zholents, and M. S. Zolotorev. Generation of femtosecond pulses of synchrotron radiation. *Science*, 287:2237–2240, 2000.

[153] M. Richter, M. Ya. Amusia, S. V. Bobashev, T. Feigl, P. N. Juranić, M. Martins, A. A. Sorokin, and K. Tiedtke. Extreme ultraviolet laser excites atomic giant resonance. *Phys. Rev. Lett.*, 102(16):163002, Apr 2009.

[154] A. A. Sorokin, S. V. Bobashev, T. Feigl, K. Tiedtke, H. Wabnitz, and M. Richter. Photoelectric effect at ultrahigh intensities. *Phys. Rev. Lett.*, 99(21):213002, Nov 2007.